Max-Planck-Institut
für Plasmaphysik

Application of a 3D Monte Carlo PIC code for modeling the particle extraction from negative ion sources

Dissertation

zur Erlangung des akademischen Grades

Dr. rer. nat.

eingereicht an der
Mathematisch-Naturwissenschaftlich-Technischen Fakultät
der Universität Augsburg

von

Ivar Mauricio Montellano Duran

Augsburg, May 2019

Universität
Augsburg
University

Vorgelegt am 20.05.2019

Tag der mündlichen Prüfung: 04.10.2019

Erste Gutachterin: Prof. Dr.-Ing. Ursel Fantz

Zweiter Gutachter: Prof. Dr. Liviu Chioncel

Contents

1 Introduction **1**

2 Negative ion sources for NBI in fusion reactors **5**

2.1 NBI sources for negative ion 9

2.2 Production and destruction mechanisms for D^- and H^- 10

2.2.1 Volume production processes 10

2.2.2 Surface production processes 13

2.2.3 Mechanisms of destruction 14

2.3 RF driven negative ion sources for the ITER NBI 15

2.3.1 BATMAN (BAvarian Test MAchine for Negative ions) 15

2.3.2 ELISE (Extraction from a Large Ion Source Experiment) . . . 17

3 Extraction region in negative ion sources **21**

3.1 Dynamics of charged particles without collisions 22

3.2 Dynamics of charged particles with collisions 23

3.3 Plasma sheath 25

3.4 Double layer 28

3.5 Negative ion extraction 30

4 PIC modeling for negative ion extraction **35**

4.1 Particle In Cell method 36

4.2 Stability criteria for explicit PIC method 40

4.3 Approaches for the PIC modeling of negative ion sources 41

4.4 The 3D PIC-MCC code ONIX 43

4.4.1 Simulation domain 44

4.4.2 Poisson's equation solver 46

4.4.3 Particle configuration shape 46

4.4.4 Particle Pusher 47

4.4.5 Collision Processes 48

4.4.6 Surface particle emission 49
4.4.7 Initial conditions 50
4.4.8 Boundary conditions 50

5 ONIX code validation 53
5.1 Physical validation 54
5.1.1 Plasma sheath 54
5.1.2 Range of accuracy 57
5.1.3 Secondary particle emission 58
5.2 Numerical efficiency of the validated model 61
5.2.1 Mesh size optimization 62
5.2.2 Time step optimization 63
5.2.3 Particles Per Cell (PPC) 64
5.2.4 Optimal parameter set 65

6 Simulations for the NBI ion sources at the test facilities 69
6.1 BATMAN extraction aperture geometry 71
6.1.1 BATMAN standard case 71
6.1.2 Extraction potential variation 77
6.1.3 Aperture geometry influence 80
6.1.4 Negative ion emission homogeneity 84
6.1.5 Isotope effect 88
6.1.6 Plasma phase simulation 93
6.2 ELISE extraction aperture geometry 94
6.2.1 ELISE standard case 95
6.2.2 Evaluation of different magnetic field configurations 103

7 Summary 109

A ONIX-IBSimu connection 117

B Magnetic field input 121
B.1 BATMAN 121
B.2 ELISE 121

Bibliography 126

Chapter 1

Introduction

Nuclear fusion is a promising source of energy for the future. One of the most developed nuclear fusion reactor concept designs is based on the magnetic confinement of a fully ionized plasma. Currently the test fusion reactor ITER[1] is under construction in Cadarache, France, to demonstrate the feasibility of nuclear fusion reactors.

ITER will explore deuterium and tritium nuclear fusion reactions. Since the nuclei of the particles are charged, they require a high kinetic energy to overcome the Coulomb repulsion. Therefore, in order to heat the plasma to the required temperatures ($> 10^8 K$), external heating systems are required. Neutral Beam Injection (NBI) systems will be used to heat the plasma and drive a current through the plasma needed for sustaining the magnetic confinement.

In general, NBI systems are divided in 4 stages: an ion source where ions are produced and extracted; the acceleration phase where the ions are brought to the required particle energy; neutralization phase where the ions are neutralized by charge exchange collisions with the background gas, and any remaining ion is deflected onto an ion dump by a magnetic or electric field; the last phase is the beam transmission where the NBI is connected to the reactor by a duct. The neutral beam can pass through the magnetic field confining the fusion plasma and once ionized heat the plasma by means of collisions. Additionally, the injected beam can be used to drive a current in the plasma, and therefore partially generate the magnetic field necessary for the plasma confinement.

ITER requires a deuterium (hydrogen) beam with 1 MeV (870 keV) particle energy. Nowadays, most NBI systems work based on the extraction and acceleration of positive ions. However, at the ITER required energies the neutralization efficiency with the background gas for positive deuterium (hydrogen) ions is negligible. Thus,

[1] "The way" in latin

the ITER-NBI system will be based on the extraction and acceleration of negative deuterium (hydrogen) ions. These ions have a neutralization efficiency of around 60% in a gas neutralizer at the required energies. Nevertheless, the choice of a negative ion source implies certain challenges, namely, the difficulties associated in the negative ion production and the co-extraction of electrons. For example, accelerating the co-extracted electrons would require to double the high voltage power supply in the acceleration phase.

The negative ion extraction and acceleration in the ITER NBI will be done by a multi-grid, multi-aperture system. A magnetic filter field is used in the ion source to reduce the electron density and temperature close to the plasma facing grid which contains the extraction apertures. Thus, diminishing the losses of negative ions by collisions with energetic electrons and reducing the co-extracted electron current.

The inevitable co-extracted electrons are deflected by a magnetic deflection field onto the second grid after extraction. A high co-extracted electron current represents a heat load on the second grid that can overcome the capabilities of the cooling system, which is already at the technological limit. Thus, the ITER-NBI ion source requires the ratio between the co-extracted electron current and the extracted ion current to be lower than 1.

The ITER-NBI is required to deliver an accelerated negative ion current of 40 A in deuterium (46 A in hydrogen). In order to achieve this, the ITER-NBI ion source design is based on the surface conversion of neutral atoms and ions into negative ions on a low work function surface. Due to its short mean free path, most of the extracted negative ions are produced in the region close to the extraction apertures. The region close to the extraction apertures with lower electron density and where most of the extracted negative ions are produced is known as extraction region.

Two test facilities at the Max Planck Institute for Plasma Physics, Garching, Germany, are in operation as part of the program for the ITER-NBI RF-driven ion source development. In order to achieve the ITER NBI source requirements, several experimental diagnostics are used to study the relation between plasma parameters in the ion source and the extracted ion current and co-extracted electron current.

Experimental campaigns, at the test facilities, have shown a relation between the negative ion density at the extraction region and the extracted ion current, as well as, a relation between the electron density and the co-extracted electron current density. A particularly higher co-extracted electron current has been measured in deuterium with respect to hydrogen, implying that the isotope influences the plasma in such a way that the co-extracted electron current is increased. Thus, the source performance

is related with plasma parameters in the extraction region, and therefore an increase of the understanding of the plasma physics in the extraction region is desired.

It is of particular interest the study of the transport of electrons under the influence of the magnetic field; the plasma sheath, which determines the negative ion transport from the surface into the plasma, and therefore the extracted ion current; the "meniscus" formation which determines the surface interface between the plasma and the extracted beam, and therefore the beam divergence. Besides the requirements for the extracted ion current, the ITER NBI demands a beam divergence between 3 and 7 mrad in order to ensure the beam transport to the reactor.

Diagnostics at the test facilities are limited up to a distance $\gtrsim$2 cm from the extraction apertures. Thus, experimental measurements do not allow for obtaining a detailed picture of the plasma physics in the extraction region, which work in the typically much smaller Debye length scale $\sim 2{\cdot}10^{-3}$ cm. Computational models have to be used to complement the measurements at the test facilities in order to study the ion (electron) transport, plasma sheath and the meniscus formation in the extraction region.

The 3D Particle In Cell Monte Carlo Collision (PIC-MCC) code ONIX was developed at LPGP, France, to study the beam formation in the extraction region of an ITER relevant ion source. Due to high calculation times required in PIC-MCC codes at the plasma densities found in the extraction region, the simulation domain is limited to one extraction aperture from $\sim$ 2 cm into the plasma and until the beginning of the second grid of the extraction system. The reduced domain is chosen to reduce the calculation time as an ONIX simulation requires at least 180 hrs in 4096 cores to reach a steady state. The code uses as input for the initial conditions densities and temperatures measured at $\sim$ 2 cm from the extraction apertures.

ONIX has been already successfully applied to study the relation between the maximum extracted current and the surface production of negative ions. Relevant output given by the code are the profile and the evolution of the electrostatic potential close to the extraction aperture, density distribution of each specie forming the plasma, extracted current density and the flow maps of electrons and negative ions before their extraction. However, before the application of the ONIX code for an analysis on the extraction region physics, a rigorous validation of the plasma physics model implemented in the code is mandatory.

As initial step of the present work, a validation of ONIX for the plasma sheath and surface emission of negatively charged particles is carried out. Besides, an op-

timization of the numerical parameters in the code is implemented to reduce the computational cost, allowing for series of parametric studies.

Parametric series of simulations with the validated ONIX code can help to understand possible factors that influence the maximum extracted current density, the co-extracted electron current and the beam optics. Parameters such as the extraction aperture geometry or the extraction potential can heavily influence the meniscus formation, and therefore the beam optics. These parameters are modified in ONIX, to fit those of the test facilities or evaluate new configurations, in order to find modifications that lead to an improvement of the ion source performance.

The measured higher co-extracted electron current in deuterium with respect to hydrogen has not been explained to this day. Therefore, it is part of the present work to study the effect of the ion mass on the plasma and its relation with the co-extracted electron current.

The ONIX capabilities to solve for the flow of particles in the plasma can be used to analyze the effect of the magnetic field in the transport of electrons. Variations of the magnetic field topology can be explored in order to find the optimal configuration for the reduction of the co-extracted electron current. Afterwards, the results can be implemented in the test facilities in order to reach the ITER NBI ion source requirements.

Chapter 2

Negative ion sources for NBI in fusion reactors

In a nuclear fusion reaction two or more nuclei combine to form a heavier one; in the process energy is generated due to the mass difference between the new formed nuclei and the total sum of the initial ones. To accomplish these reactions, the nuclei have to overcome the Coulomb repulsion (long range) until they are in the range of the nuclear force (short range), which attracts the nuclei and produces the fusion reaction. The particles need a high kinetic energy to overcome the initial electrostatic repulsion, however, the quantum tunneling-effect allows fusion reactions at energies lower than that set by the Coulomb barrier. The fusion reaction D + T $\longrightarrow$ ^{4}He(3.5 MeV) + n(14.1 MeV) between deuterium and tritium has the highest reaction rate at the lowest energies, see figure 2.1, and therefore is planned to be used in the different concepts of nuclear fusion reactors.

One of the most developed concepts for nuclear reactors is the magnetic confinement. A plasma is confined by a magnetic field and is heated up by external systems up to the required temperatures ($\sim$20 keV) needed for the nuclear reactions. A magnetic field with a toroidal topology allows a plasma confinement over a finite volume; the toroidal field lines are required to reduce particle losses due to drift velocities. This magnetic field can be decomposed into two components: one poloidal (along the minor radius) and one toroidal (along the major radius). Two concepts under this idea have been developed [1]: the Stellarator and the Tokamak. In a Stellarator the magnetic field is generated uniquely by the use of complex external field coils. A Tokamak, as shown in figure 2.2, has external poloidal coils that generate the toroidal magnetic field. The poloidal magnetic field is generated by a combination of external toroidal coils and a plasma current. A varying (increasing) current is driven through a central solenoid, creating a magnetic field which induces a toroidal

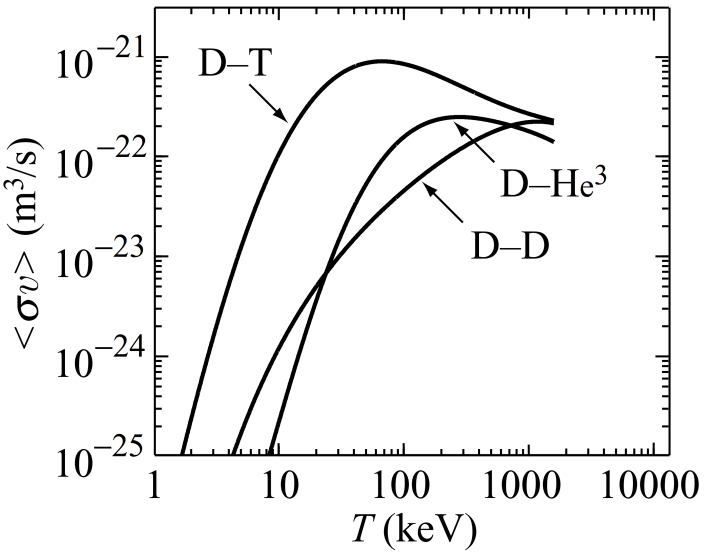

Figure 2.1: Reaction rate averaged over a Maxwellian energy distribution as function of the temperature for different fusion reactions between hydrogen isotopes: deuterium-deuterium (D-D), deuterium-tritium (D-T) and deuterium-helium (D-^{3}He) [1].

current in the plasma. This is the same principle of a transformer: the solenoid acts as the primary and the plasma as secondary. In this way a CW operation scenario for a Tokamak is not feasible as the current in the transformer can not be indefinitely ramped. However, a steady state Tokamak operation can be done by driving plasma currents non-inductively [1].

The future international test fusion reactor ITER, based on the Tokamak concept [3], is planned to start operation in 2025 [4]. The ITER toroidal vacuum vessel dimensions account for a major radius $R = 6.2$ m and minor radius $r_{\min} = 2.0$ m, with a plasma volume of $\sim$837 m^3, making it the biggest Tokamak built up to the date. ITER will rely on three different external heating techniques in order to achieve the required input power of 73 MW [5] to reach the required plasma temperatures. High frequency electromagnetic waves based on ion cyclotron resonance heating (ICRH) and electron cyclotron resonance heating (ECRH) will deliver 20 MW [5] to the plasma. Two Neutral Beam Injection (NBI) systems will deliver a total of 33 MW [5] of heating power.

Generally, NBI systems inject a high energy neutral beam into fusion devices (e.g. Tokamak). Neutral particles are used in order to pass through the magnetic field containing the plasma; the particles are then ionized and heat up the plasma by means of collisions. NBI systems can also be used to generate the required toroidal

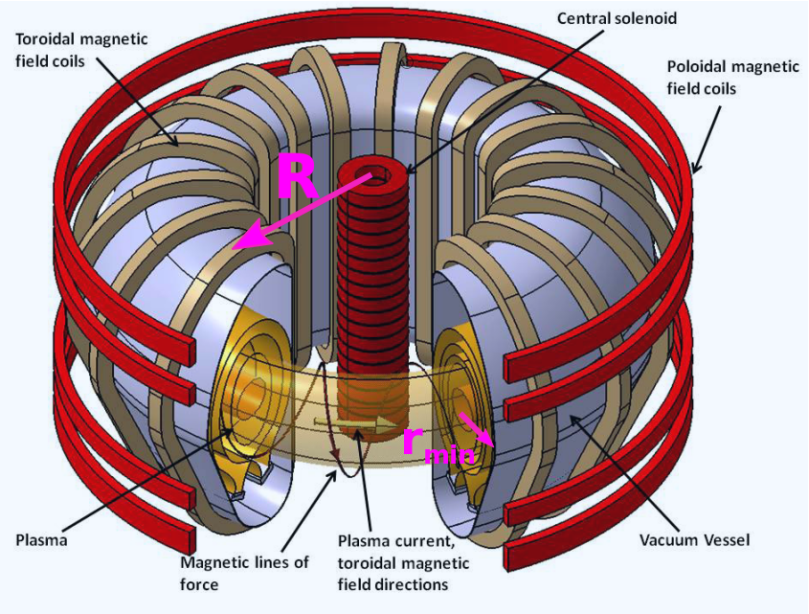

Figure 2.2: Schematic of a Tokamak [2]: shown are the central solenoid, the external toroidal coils, the external poloidal magnetic field coils, the major radius R and the minor radius r_{min}.

current for a Tokamak if applied tangentially to the torus, allowing in this way a CW operation scenario. The scheme of a NBI system is presented in the figure 2.3. Ions (positive or negative) are produced in an ion source, extracted and accelerated by an electric field produced by a multi-aperture multi-grid system and neutralized in a gas target by charge exchange collisions. Any remaining ions are deflected by an electric or magnetic field onto a residual ion dump.

ITER requires a NBI system that produces beams of 1 MeV (870 keV) with a pulse length of up to 3600 s (1000 s) in steady operation for deuterium (hydrogen). These energies are much higher than what is used up to now in fusion machines ($\lesssim$ 100 keV in the ASDEX experiment [6]). The higher energies are a consequence of the higher densities and bigger dimensions of the torus vessel, requiring the particles an energy above ∼300 keV in order to reach the plasma core [7]. Additionally, the efficiency for current drive depends on the beam energy. Therefore, the energy requirement for the D^0 beam is a compromise between the need to deposit power across the plasma minor radius, the need to drive the plasma current and the technological difficulties of developing a high voltage system to obtain the required accelerated current densities. If the accelerator optimized for D^- and the required accelerated current of 40 A at 1 MeV is operated with H^-, optimized beam optics are achieved at 870 kV with an accelerated current of 46 A [7]. Up to now the existing negative ion NBI system at

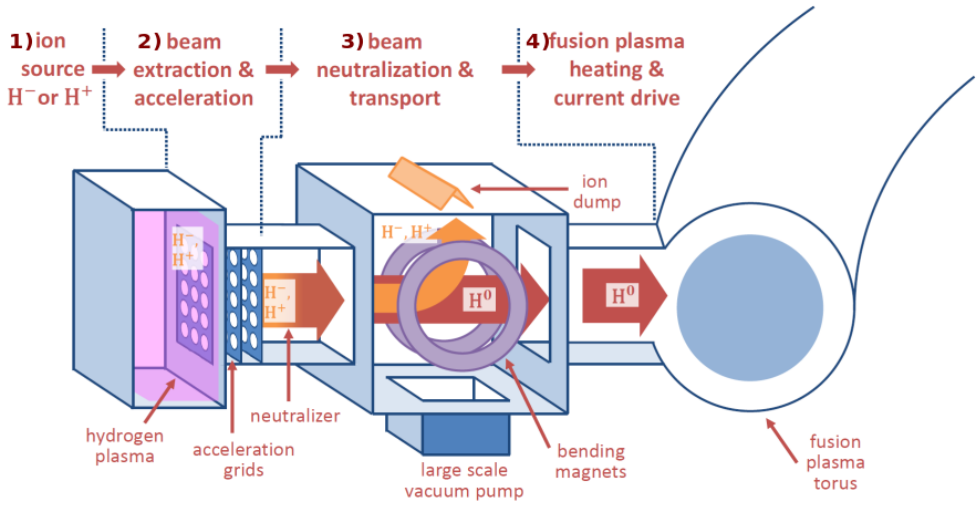

Figure 2.3: Schematic of the structure of a NBI line: 1) Ion source; 2) Extraction & acceleration grid system; 3) Beam neutralizer & Residual ion dump ; 4) Connection duct from the NBI to the Tokamak.

JT-60U has achieved a beam of 500 keV [8] for 30 s and the ITER test facility at QST has achieved a beam with a particle energy of 970 keV for 60 s [9].

Most existing NBI systems work based on the acceleration and neutralization (with a gas target) of positive ions. Figure 2.4 shows the neutralization efficiency for an optimized gas neutralizer [10]. At the ITER beam energies the neutralization efficiency for positive hydrogen ions is reduced to less than 10 %. Thus, used at ITER will be a NBI based on the extraction and acceleration of negative ions. For an optimized neutralizer with a gas target the neutralization efficiency for negative ions is around 60 % for the ITER NBI energy requirements. The higher neutralization efficiency of negative ions is due to the low binding energy 0.75 eV of the electron in the hydrogen atom. Due to the fragility of the ions and in order to diminish the ion losses in the acceleration stage the gas pressure in the ion source has to be kept below 0.3 Pa [11].

The requirements for the ITER NBI system based on the acceleration of negative ions bring new challenges to the production and extraction of negative ions, compared to the already widely used positive ion sources. Although negative ion based NBI systems are already in use [8][13], achieving the ITER NBI requirements face problems such as the negative ions being more difficult to create: they are easily lost by collisions with the background gas in the ion source plasma and in the accelerator. Besides, co-extracted electrons can lead to high power loads on the NBI extraction or acceleration components. In order to confront these issues a research and development plan for

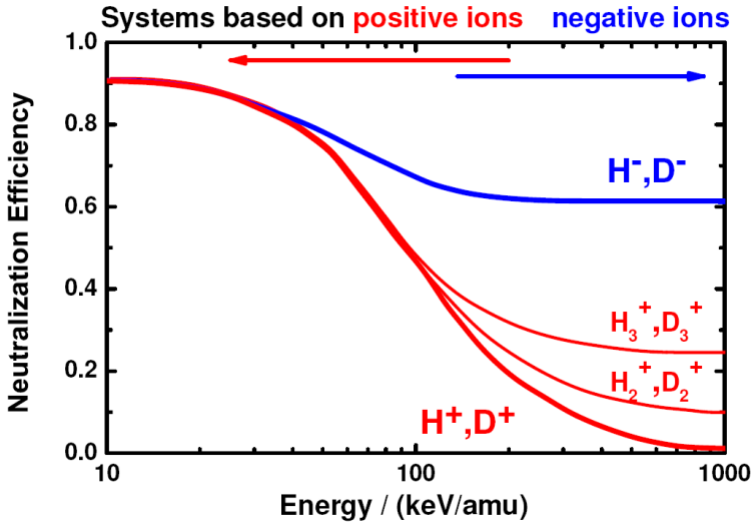

Figure 2.4: Neutralization efficiency for an optimized gas neutralizer respect to the energy per mass of the accelerated particle [12].

the negative ion sources has been implemented [14].

2.1 NBI sources for negative ion

The ITER requirements for the accelerated current can be extrapolated backwards to the extracted current from the ion source assuming a neutralization efficiency of ∼60% [7] and losses in the acceleration phase due to stripping of the electrons with the background gas ∼20-30% at 0.3 Pa [11]. The requirements for the ITER NBI accelerated and extracted beam are shown in the table 2.1 [15].

ITER	
Heating power	16.6 MW
Beam energy D^- (H^-)	1(0.87) MeV
Pulse length D^- (H^-)	3600 (1000) s
Extracted current D^- (H^-)	57 (66) A
Extracted current density D^- (H^-)	285 (329) A/m^2
Extraction area	2000 cm^2
Number of extraction apertures	1280
Beam inhomogeneity	<10%
Source pressure	0.3 Pa
extracted electron-ion current density ratio	≤ 1

Table 2.1: Beam requirements for the ITER NBI for D and H [7].

The current density extracted from negative ion sources typically is comparatively lower to those from positive ion sources (up to 339 Am^{-2} for negative ions [16] and 2300 Am^{-2} for positive ions [17]). Thus, to obtain the required extracted current the dimensions of the extraction area is increased in negative ion sources. Due to the larger extraction area another requirement is given to the beamlet spatial homogeneity in order to ensure the beam transmission: any two random points of the beam cross section should not differ more than 10 % in their intensity.

Furthermore, when extracting negative ions inevitably co-extraction of electrons occurs. These electrons are deflected by a magnetic field and dumped onto the second grid before their full acceleration, otherwise the power needed to sustain the acceleration voltage would double. A maximum tolerable co-extracted electron current is defined by the heat load supported by the technological limits of the cooling system in the grid. For ITER this technological limitation is expressed in the beam parameters as requiring a co-extracted electron current density lower than the extracted ion current density, $j_e/j_{D^-} \leq 1$.

2.2 Production and destruction mechanisms for D^- and H^-

In order to achieve the extracted current requirements for the ITER NBI, negative ions can be formed by several mechanisms such as volume processes by electron impact or surface conversion of impinging particles [18]. The production rate $R_{\text{Production}}$ can be enhanced by varying parameters such as the electron temperature, the plasma density or gas density. However, several destruction mechanisms of negative ions arise with the same parameters, increasing the destruction rate $R_{\text{Destruction}}$. Thus, the net production rate of negative ions is given by the equilibrium between the production and destruction mechanisms: $R_{\text{Net}} = R_{\text{Production}}$ - $R_{\text{Destruction}}$.

The description of the production and destruction mechanisms for negative hydrogen ions is given in the following. As the atomic processes are the same for hydrogen and deuterium, they will be referred only for hydrogen unless a difference exists between the isotopes.

2.2.1 Volume production processes

The main volume process for the generation of negative hydrogen ions, in a hydrogen plasma, is dissociative electron attachment of vibrationally excited molecules $H_2(\nu)$

[19]:

$$H_2(\nu) + e \longrightarrow H^- + H, \tag{2.1}$$

where ν is the quantum number of the vibrational state of the molecule. As shown in figure 2.5, the maximum value of the cross section for dissociative attachment increases with the vibrational quantum number, becoming considerably higher for $\nu \gtrsim 5$ for hydrogen and $\nu \gtrsim 8$ for deuterium. Besides, the electron temperature at which the maximum cross section is achieved decreases with ν. Thus, the production of negative ions can be enhanced with an electron temperature $T_e \leq 1$ eV and increasing the population of molecules excited in high vibrationally states. However, the excitation of molecules to high vibrational states is produced by collisions with energetic electrons ($T_e \geq 10$ eV) [20]:

$$H_2 + e \longrightarrow H_2(\nu) + e. \tag{2.2}$$

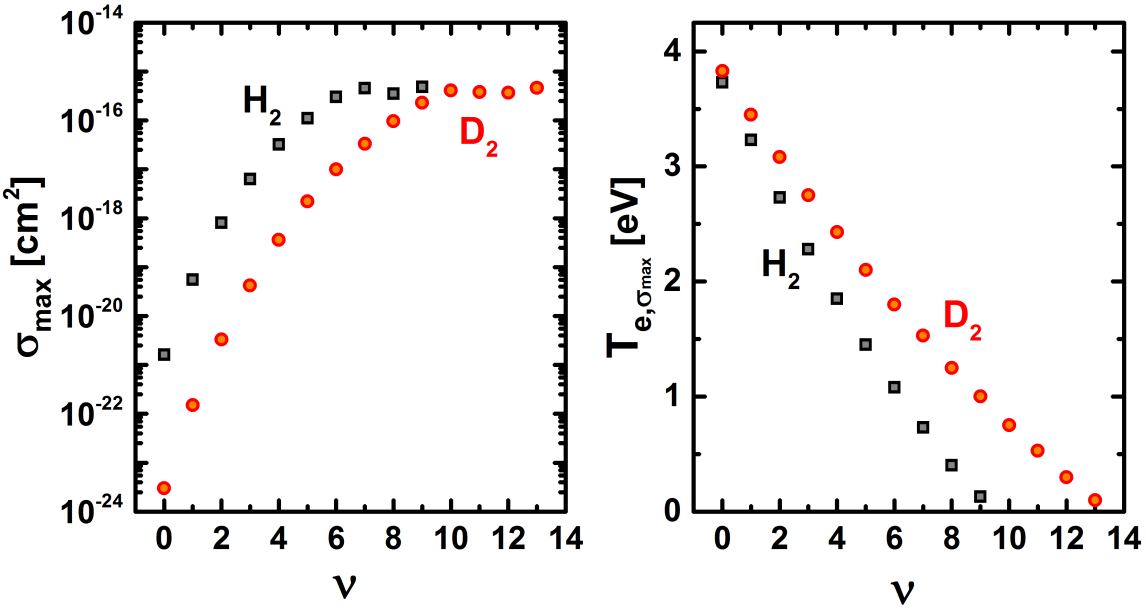

Figure 2.5: Left) Maximum cross section for the dissociative attachment process in hydrogen and deuterium versus the vibrational excitation quantum number ν; Right) Electron temperature at which the cross section for dissociative attachment reaches the maximum as function of ν. The plotted data is taken from [20].

In order to spatially divide the processes 2.1 and 2.2 in a plasma, a tandem concept [21] as shown in figure 2.6 is used. In the plasma driver segment the plasma is generated and high electron temperatures (> 10 eV) are present. Therefore, in

the driver the vibrational excitation of the molecules via process 2.2 is enhanced. This segment is separated from the extraction region, where the extraction apertures can be found, by a magnetic filter field perpendicular to the electron flow. The magnetic field can be generated by external permanent magnets located outside the plasma chamber or by an electric current, of the order of kA, flowing through the grid containing the extraction apertures. Therefore, electrons traversing the magnetic filter field are cooled down and in the extraction region the electron temperature is lowered below 2 eV in order to enhance the dissociative attachment of vibrationally excited molecules. The produced vibrationally excited molecules in the driver region pass through the magnetic field into the extraction region, and thus the production of negative ions through the process in equation 2.1 is enhanced in the extraction region.

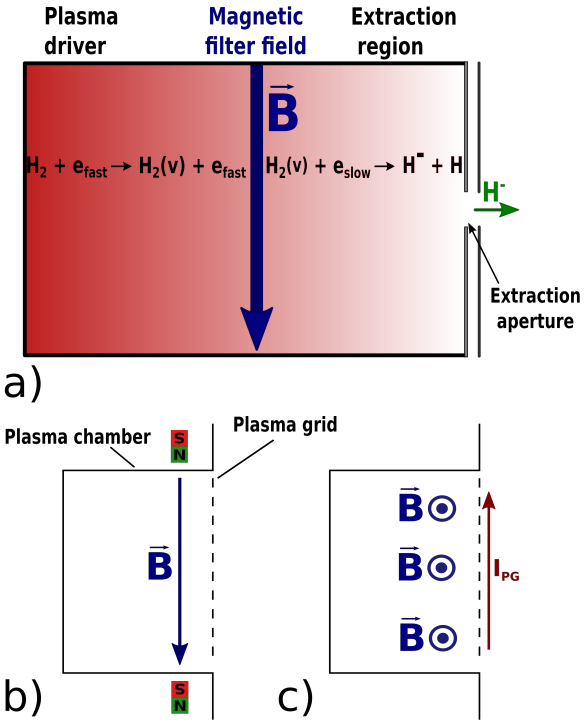

Figure 2.6: a) Schematic of the tandem concept for negative ion sources using a magnetic filter field **B**. b) Magnetic filter field generated by permanent magnets; c) Magnetic filter field generated by a current I_{PG} flowing through the plasma grid.

The negative ions are extracted from the ion source by applying a positive potential difference between the plasma facing grid (PG) containing the apertures and a following grid usually called extraction grid (EG).

Because molecules are involved in the creation of H^-, ion sources based on volume processes need to increase the pressure, thus the H_2 density, in order to enhance the

negative ion production. However, the high pressure required for an efficient volume process based ion source is not compatible with the ITER requirement of a maximum pressure of 0.3 Pa in the source.

2.2.2 Surface production processes

Negative ions can be produced by the conversion of atoms or positive ions colliding with a surface [19]. The formation of the negative ions can be described in a two step process for ions and a single step for atoms:

$$H^+ + e_{\text{surface}} \longrightarrow H^-. \tag{2.3}$$

$$H + e_{\text{surface}} \longrightarrow H^-. \tag{2.4}$$

The first step, given by equation 2.3, is the neutralization of positive ions by either an Auger or resonant process. The second step, described by equation 2.4, is the negative surface ionization of hydrogen due to the direct transfer of an electron from the surface to the atom leaving the surface.

A physical description of processes during the atom surface ionization is given in the following. The electron affinity of an atom is a measure of the capacity to retain one additional electron, and the value for a hydrogen atom is 0.75 eV [22]. As an atom gets closer to the surface the affinity level is decreased. It goes below the work function of the surface, the atom captures an electron from the surface to the affinity level and escapes from the surface as a negative ion [19].

In order to enhance the negative ion surface production, the surface work function is reduced by the adsorption of Cs which has the lowest work function of all elements (2.14 eV) [23]. Preparing a surface made entirely of Cs is not possible due to its low melting point of 28 °C [24] and its high chemical reactivity. The work function of a metal coated with Cs depends on the thickness of the Cs layer and the compound i.e. of the chemistry of Cs layers [25]. Therefore, a non-homogeneous work function over the surface may occur due to the formation of compounds or variation of the Cs thickness layer.

Negative ion sources based on surface production have shown an extracted negative ion current ∼10 times higher compared to the ion sources based on volume production [26]. Besides, a strong reduction of the co-extracted electron current was also seen in the surface production ion sources [19][26].

In order to enhance the surface production of negative ions, the flow of H and H^+ onto the surface has to be increased. Increasing the dissociation of hydrogen molecules increases the flow of atoms and ions onto the surface, and therefore the surface production of negative ions. The dissociation rate is enhanced with increasing electron temperature [27].

However, higher H and H^+ densities and energetic electrons also increase the destruction rate of negative ions [28], the destruction processes involved are described in the following section.

2.2.3 Mechanisms of destruction

Due to the low binding energy of the additional electron to the hydrogen atom, the negative ions in a plasma have a short survival length.

Collision of a negative ion with an electron can strip the additional electron:

$$H^- + e \longrightarrow H + 2e \ \textit{(electron stripping)}. \tag{2.5}$$

The efficacy of the electron stripping process depends on the energy of the colliding electron, becoming dominant for $T_e > 20$ keV [28]. The electron stripping can be diminished by applying the tandem concept, reducing the electron temperature below 2 eV reduces the electron stripping rate by two orders of magnitude.

Other destruction channels can still take place regardless of the electron temperature:

$$H^- + H^+(H_2^+, H_3^+) \longrightarrow H + H(H_2, H_3) \ \textit{(mutual neutralization)}, \tag{2.6}$$

$$H^- + H \longrightarrow H_2 + e^- \ \textit{(associative detachment)}, \tag{2.7}$$

$$H^- + H \longrightarrow 2H + e^- \ \textit{(non-associative detachment)} \ , \tag{2.8}$$

$$H^- + H_2 \longrightarrow H + H_2 + e^- \ \textit{(collisional detachment)} \ . \tag{2.9}$$

The reaction rate for mutual neutralization depends on the positive ion density and the associative detachment and non-associative detachment with hydrogen atoms depend on the density of H atoms. Thus, these processes cannot be diminished in the plasma volume without reducing the surface production of negative ions. In order to reduce the reaction rate of collisional detachment of negative ions with the hydrogen

molecules in the acceleration phase, the pressure of the source is required to be 0.3 Pa for the ITER NBI.

2.3 RF driven negative ion sources for the ITER NBI

The radio frequency inductively driven negative ion source developed at IPP Garching [29] has demonstrated capabilities to generate the required current densities in short pulses (< 4 s)[30], and it has been selected as reference design for the ITER NBI ion source [15]. As part of the roadmap for the development of ITER NBI ion source, the test facilities BATMAN and ELISE are currently in operation at IPP Garching [31].

2.3.1 BATMAN (BAvarian Test MAchine for Negative ions)

The prototype negative ion source at the BATMAN test facility was built to prove the feasibility of high extracted H^- (D^-) current at ITER relevant conditions (0.3 Pa pressure and a ratio of co-extracted electrons to negative ions below 1). Figure 2.7 shows a CAD drawing of the ion source at BATMAN. The ion source can be divided in three segments: driver, expansion region and extraction and acceleration system.

In the driver region the plasma is generated by inductive coupling of the RF power (up to 150 kW, f=1 MHz) by an water cooled RF coil with six windings around an alumina cylinder (24 cm diameter and 14 cm length)[29][32]. The plasma parameters found in this region are $n_e \sim 10^{18}$ m^{-3} and $T_e \sim 10$ eV [33], resulting in a dissociation degree H/H_2 ∼0.2-0.3. The plasma expands out from the driver region and flows into the expansion chamber.

The expansion chamber follows the tandem concept; a magnetic filter field, generated by permanent magnets, reduces the diffusion of energetic electrons to the plasma grid (PG) where the extraction apertures are located. In the region close to the extraction apertures (∼2 cm) the electron density is decreased to $\sim 10^{17}$ m^{-3} and the electron temperature to ∼ 1 eV [16]. A metallic bias plate, located in front the PG and surrounding the apertures, is connected to the source potential. As the PG is electrically isolated, a variation of its potential with respect to the bias plate changes the structure of the electric potential close to the PG. Thus, the fluxes of charged particles onto the PG are modified and a reduction of co-extracted electrons can be achieved. An oven nozzle evaporates Cs in the expansion chamber. The evaporated

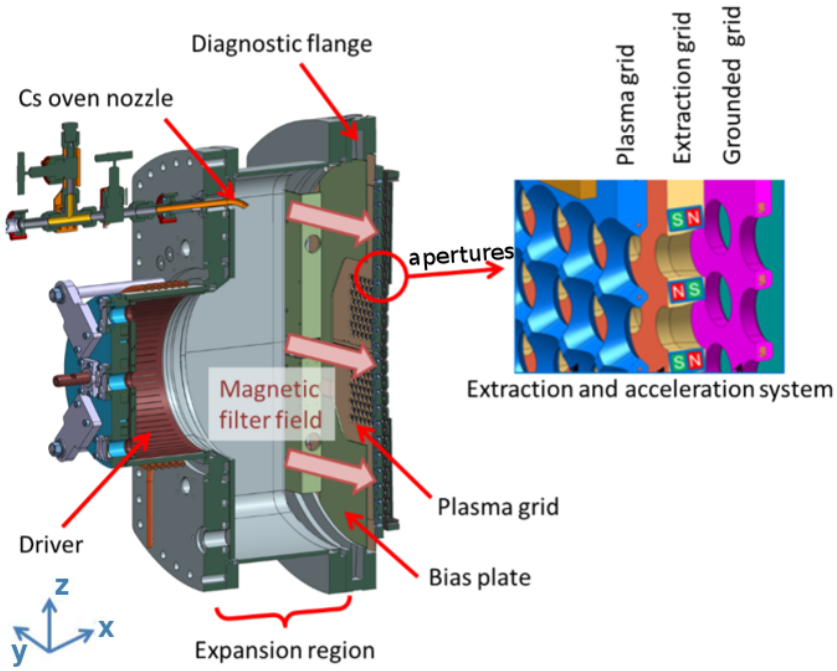

Figure 2.7: CAD drawing of the prototype source used at the BATMAN test facility.

Cs then covers the surfaces of the expansion chamber, enhancing the surface production of negative ions. The Cs oven is located on the top part of the back-plate of the expansion region.

The extraction of negative ions is done with a multi-aperture multi-grid system consisting of the PG, the extraction grid EG and the grounded grid GG. The plasma grid is made of molybdenum [32], on which the evaporated Cs is deposited to enhance the negative ion formation close to the extraction apertures. The use of molybdenum minimize any sputtering which could contaminate the Cs layer on the PG. The PG has 126 chamfered apertures with a diameter of 8 mm each (configuration used up to 2016), accounting for a total of 63 cm^2 extraction area. The chamfered extraction aperture geometry was chosen as it increases the probability of extraction of the surface produced negative ion from the PG [34].

A positive potential difference between PG and the EG (up to 10 kV) allows the extraction of negative ions. An acceleration voltage between the GG and the EG is set between 10-20 kV; the maximum total high voltage is limited to 22 kV by the power supply. The extraction of negative ions is done in pulsed operation: 4 seconds of beam extraction in a 6-10 s plasma pulse, with ∼180 s in between pulses. The pulsed operation is due to limitations in the high voltage supplier and vacuum systems.

Co-extracted electrons are deflected onto the EG by a dipole magnetic field created

by permanents magnets embedded inside the EG with alternating polarity. The power heat load that can be deposited onto the EG is technologically limited by the cooling capacity of the grid [35]. This constraint limits other source parameters that could potentially increase the extracted current density. For example, an increase in the RF power increases the molecular dissociation, increasing the flux of neutrals onto the PG, and therefore enhancing the surface production of negative ions; however, the plasma density is also increased, and therefore so does the co-extracted electron current. Thus, the RF-power is limited in order to avoid a high co-extracted electron current.

2.3.2 ELISE (Extraction from a Large Ion Source Experiment)

The ion source at the ELISE test facility is an intermediate step in between the prototype source and full ITER size ion source [16], having the same width and half the height of the ITER source. Figure 2.8 shows the ion source of the ELISE test facility with main parts highlighted.

The physical principles used for plasma operation and negative ion production is the same as in the prototype source. The plasma is generated by 4 cylindrical drivers arranged in pairs (27.6 cm inner diameter and 15.7 cm length) with a maximum RF power of 360 kW (90 kW per driver). Two Cs ovens are located on the lateral sides of the expansion chamber. The expansion chamber volume is 100 x 87 x 22 cm^3.

The magnetic filter field is created by a current I_{PG} through the PG. Additionally, external permanent magnets can be attached to the side walls of the source in order to strengthen or weaken the magnetic filter field and modify its topology. The I_{PG} current can be set up to 5 kA corresponding to a field strength of $\sim$4.2 mT at 1 cm distance from a PG aperture.

As in the prototype source the extraction and acceleration system consist of three multi-aperture grids. The plasma grid has a total of 640 chamfered apertures with 14 mm diameter, the aperture diameter being the same as for the ITER NBI ion source [16]. The total extraction area is 985 cm^2, accounting for half of that in the ITER NBI source (1970 cm^2). The apertures are divided in 8 beamlet groups, 4 in the top and 4 in the bottom. The distance between the PG and the EG (6 cm) at ELISE is the same used in the ITER-NBI source [36], implying that the electric field applied to extract the negative ions is similar (for the same extraction voltage).

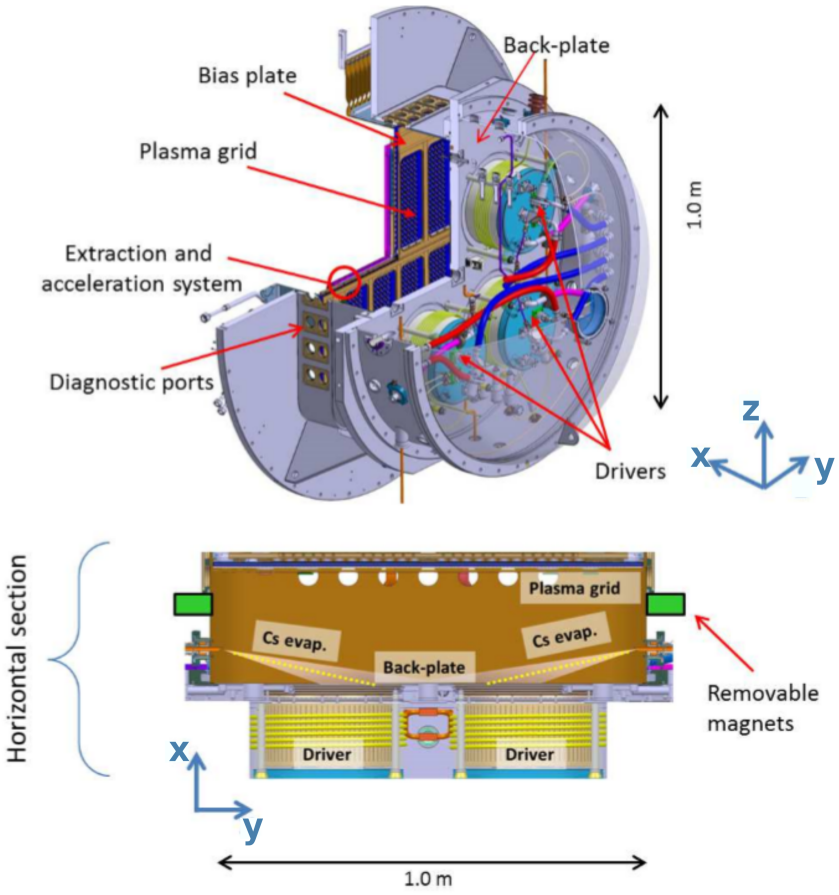

Figure 2.8: CAD drawing of the ELISE test facility.

The ELISE test facility was designed for long plasma pulses up to 3600 s. Technical limits of the high voltage power supply result in a maximum length of beam extraction of 10 s every 150 s. During long plasma pulses, a series of beam extraction blips are done. Figure 2.9 shows experimental data for hydrogen and deuterium of the extracted current density and the electron-ion current density ratio for short pulses (plasma-on-time: 20 s). The results show a higher extracted negative ion current and a lower electron-ion ratio in hydrogen with respect to deuterium; even more notorious, the co-extracted electron current has a stronger increase over time in a deuterium plasma. The higher co-extracted electron current in deuterium limits the operation parameters like the RF power or the extraction potential, and usually a higher filter field intensity is required. This high co-extracted electron current represents one of the biggest challenges in the achievement of the ITER-NBI source requirements for deuterium.

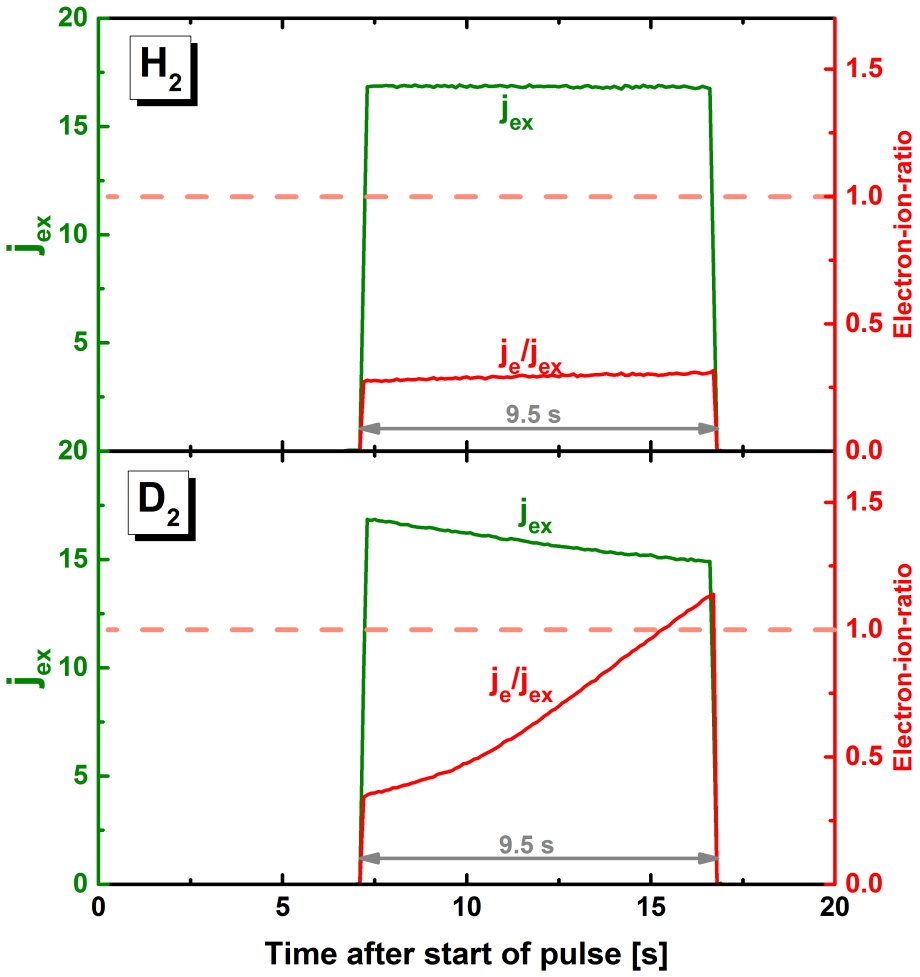

Figure 2.9: Time traces of the extracted ion current (green) and the electron-ion ratio (red) at ELISE in hydrogen and deuterium operation with 0.3 Pa of gas pressure in the source for a short pulse [16].

Chapter 3

Extraction region in negative ion sources

Understanding the behavior of the co-extracted electron current and negative ion extracted current requires a comprehension of the plasma transport in the extraction region. The transport of electrons in the extraction region is heavily influenced by the presence of the magnetic filter field and the magnetic deflection field in the EG. The magnetized electrons are transported through the magnetic field lines by collisions with gas molecules or by the development of drift velocities due to the electric field and/or inhomogeneities in the magnetic field present in this region. The transport of negative ions through the plasma towards the extraction apertures depends significantly on their origin: those produced at the surface have a preferential direction perpendicular to the emitting surface, and therefore their initial direction has to be bended in the direction of the PG before extraction; the volume produced negative ions present an homogeneous velocity distribution and their flow to the extraction apertures is that of a thermal flow [37].

The interaction between the plasma and the containing walls affects the transport of surface produced negative ions into the plasma and of the electrons onto the PG. The electrostatic potential in the region close to the emitting surface evolves according to the fluxes of charged particles from the plasma onto the surface and the fluxes from the surface into the plasma. A steady state for the electrostatic potential depends of parameters such as plasma density, electron temperature, ion temperature, negative ion emission rate and the applied voltage between the PG and the EG. The interface between the plasma and the surface reaches a steady state by the development of the plasma sheath, which produces a potential drop between the plasma and the surface in order to keep a quasi-neutral plasma, i.e. same fluxes of charges particles from the plasma onto the surface.

A similar structure forms at the interface between the quasi-neutral plasma and the extraction potential. The surface defining the penetration of the extraction potential in the plasma is known as "meniscus". Over this surface there is an equilibrium between the forces generated by the plasma pressure P and the extraction potential Φ, using the fluid representation of a plasma [38] the equilibrium is expressed as $\frac{\nabla \mathrm{P}}{n} = -q\nabla\Phi$. The shape of the meniscus influences the beam formation, as the initial velocity angle of the extracted particles with respect to the beam direction is defined by its curvature.

Insights into the physics of the extraction region can be obtained by considering simplified situations, as will be shown in this chapter. Nonetheless, a complete description of the extraction region requires more complex modeling as a PIC model such as the one described in Chapter 4.

3.1 Dynamics of charged particles without collisions

The analysis of the movement of single charged particles in electric and magnetic fields allows to understand the more global dynamics of the plasma. The equation describing the dynamic of a charged particle is:

$$\frac{d^2\mathbf{x}}{dt^2} = \frac{q_\mathrm{s}}{m_\mathrm{s}}(\mathbf{E} + \mathbf{v} \times \mathbf{B}), \tag{3.1}$$

where q_s and m_s are the charge and mass of a particle s, $\mathbf{E}$ is the electric field and $\mathbf{B}$ the magnetic field.

In the simplified case of a charged particle under the influence of a constant and homogeneous magnetic field, the particle trajectory is helicoidal along the magnetic field lines. The velocity $\mathbf{v}$ can then be divided into a rotational velocity $\mathbf{v_g}$ around the magnetic field lines, and a velocity $v_{||}\hat{\mathbf{b}}$ in the magnetic field direction $\hat{\mathbf{b}}$: $\mathbf{v} = v_{||}\hat{\mathbf{b}} + \mathbf{v_g}$. The circular motion along the magnetic field lines has a radius of rotation $\rho_\mathrm{g} = \frac{m_\mathrm{s} v_\perp}{q_\mathrm{s} B}$ ($v_\perp = |\mathbf{v_g}|$) and frequency $\omega_\mathrm{g} = \frac{q_\mathrm{s} B}{m_\mathrm{s}}$, denominated gyroradius and cyclotron frequency respectively. The gyroradius is usually used in the definition of magnetization (without considering collisions). If ρ_g is smaller than the characteristic length of the system, then the particle is considered magnetized as the magnetic field affect the trajectories of the particle at the scale of interest.

The addition of any force perpendicular to the magnetic field produces a drift velocity on the magnetized particles [39]. For example, if an electric field perpendicular

to the magnetic field is added, it accelerates the particle in half of the rotation period increasing the gyroradius; while, it decelerates the particle in the other half, reducing the gyroradius. The variations of the gyroradius through the particle trajectory produces a drift velocity which is proportional to the intensity of the electric field $v_{\mathbf{E}\times\mathbf{B}} = \frac{\mathbf{E}\times\mathbf{B}}{B^2}$. Generally, any external force $\mathbf{F}$ generates a drift velocity $v_{\mathbf{F}} = \frac{1}{q_\mathrm{s}}\frac{\mathbf{F}\times\mathbf{B}}{B^2}$.

Drift velocities may also be originated from non-uniformities in the magnetic field. For example, if a particle moves into a region with a more intense magnetic field, its gyroradius is reduced and the net effect is a drift velocity $v_{\nabla\mathbf{B}} = \frac{m_\mathrm{s}v_\perp^2}{2q_\mathrm{s}B}\frac{\mathbf{B}\times\nabla B}{B^2}$. If the magnetic field lines are curved a drift velocity is originated as the magnetized particles tend to follow the curvature of the field lines $v_{\mathbf{R}} = \frac{m_\mathrm{s}v_{||}^2}{q_\mathrm{s}B}\frac{\mathbf{B}\times\nabla B}{B^2}$. The addition of all the drift velocities to the helicoidal movement allows to express the velocity of a charged particle as:

$$\mathbf{v} = v_{||}\hat{\mathbf{b}} + \mathbf{v_g} + \frac{\mathbf{E}\times\mathbf{B}}{B^2} + \frac{1}{q_\mathrm{s}}\frac{\mathbf{F}\times\mathbf{B}}{B^2} + \frac{m_\mathrm{s}v_{||}^2 + m_\mathrm{s}v_\perp^2/2}{q_\mathrm{s}B}\frac{\mathbf{B}\times\nabla B}{B^2}. \tag{3.2}$$

The drift velocity $v_{\mathbf{E}\times\mathbf{B}} = \frac{\mathbf{E}\times\mathbf{B}}{B^2}$ does not depend on the particle charge, and therefore all the particles in the plasma globally move without producing any net electric current in the plasma. The drift velocities occasioned by either the gradient or curvature of the magnetic field are charge dependent, and therefore differently charged particles move in opposite directions.

In the extraction region of a NBI ion source, the magnetic filter field is low such that only the electrons are magnetized over one aperture domain. The gyroradius of electrons is around ∼0.3 mm while the extraction aperture diameter is between 8-14 mm, meaning that the trajectories are significantly changed by the presence of a magnetic field at the scale of one extraction aperture. The positive and negative ions are, however, less affected by the magnetic field; their gyroradius being around ∼9 mm. Thus, the transport of the magnetized electrons in the extraction region is dominated by the topology and strength of the magnetic field. The other charged species in the plasma are also influenced by the magnetic field topology through the electrons, as they redistribute in space in order to keep the plasma quasi-neutrality.

3.2 Dynamics of charged particles with collisions

In the presence of a magnetic field the velocities of charged particles perpendicular to it are smaller than the parallel one, $v_\perp \ll v_{||}$. Besides the drift velocities, magne-

tized particles can traverse magnetic field lines by momentum exchange produced by collisions with the background gas or other charged particles and by the development of turbulent transport.

In the extraction region the momentum transfer for the magnetized electrons is dominated by collisions with the atoms and molecules. However, due to its higher mass, the ion momentum transfer is dominated by Coulomb collisions with other ions. Negative ions emitted from the surface have a preferential direction perpendicular to the surface; however, it is possible to to redistribute these particles through the plasma (i.e modify significantly their trajectory) by momentum transfer or the magnetic field curvature [34]. If there is no redirection of the particles to the extraction aperture, the negative ions emitted from the surface go into the plasma and are destroyed before other effects (e.g. drift velocities, magnetic fields) can redirect these particles to the extraction aperture.

The diffusion equation describes the collective motion of particles resulting from density gradients. Assuming the mean free path λ_{mfp} is small when compared to the size of the system, it can be written as:

$$\frac{\partial n_{\mathrm{s}}}{\partial t} = \nabla \cdot (D \nabla n_{\mathrm{s}}), \tag{3.3}$$

where D is the diffusion coefficient and n_{s} the density of the specie s. For a non-magnetized system, particles will follow straight path segments in between collisions and the diffusion coefficient can be expressed as:

$$D \approx \nu_{\mathrm{coll}} \lambda_{\mathrm{mfp}}^2 \approx \frac{k_{\mathrm{B}} T_{\mathrm{s}}}{\nu_{\mathrm{coll}} m_{\mathrm{s}}}, \tag{3.4}$$

where ν_{coll} is the collision frequency, T_{s} the temperature of particles of specie s (assuming a Maxwellian energy distribution) and m_{s} is the mass of particle of specie s.

If the particles are magnetized, their mobility in the direction perpendicular to the magnetic field is of the order of ρ_{g}. For helicoidal trajectories of magnetized particles and considering $2\pi\rho_{\mathrm{g}} < \lambda_{\mathrm{mfp}}$ the diffusion coefficient becomes:

$$D_{\perp} \approx \nu_{\mathrm{coll}} \rho_{\mathrm{g}}^2. \tag{3.5}$$

In the parallel direction the mobility of the particles is still of the order of λ_{mfp} and therefore $D_{||} \approx \frac{k_{\mathrm{B}} T_{\mathrm{s}}}{\nu_{\mathrm{coll}} m_{\mathrm{s}}}$. Therefore, collisions enhance the transport of particles in the direction transverse to a magnetic field and reduce it in the the parallel direction.

Due to its larger gyroradius, the diffusion coefficient of ions in the direction perpendicular to the magnetic field is larger than that of electrons. However, to maintain a quasi-neutral plasma, the fluxes of particles self adjust by the generation of internal electric fields due to charge imbalances. The process through which the plasma keeps its quasi-neutrality is called *ambipolar diffusion* [38] and its diffusion constant for an electron-ion plasma is given by:

$$D_{\perp \mathrm{amb}} \approx \nu_{\mathrm{ei}} < \rho_{\mathrm{e}} > \left(1 + \frac{T_{\mathrm{i}}}{T_{\mathrm{e}}}\right), \tag{3.6}$$

where $\nu_{\mathrm{ei}} \propto T_{\mathrm{e}}^{-\frac{3}{2}}$ is the electron ion collision frequency and $< \rho_{\mathrm{e}} > = < \frac{m_{\mathrm{e}}^2 v_{\perp}^2}{q^2 B^2} > \propto T_{\mathrm{e}}$ is the average electron gyroradius over a gyration period. The ambipolar diffusion coefficient is then proportional to $T_e^{-\frac{1}{2}}$, meaning that the diffusion through a magnetic field is less effective for higher electron temperatures.

The magnetic filter field used in the negative ion sources is perpendicular to the flow of particles from the driver towards the PG, and therefore it reduces the flux of fast electrons while low temperature electrons pass at a higher rate, as designed for the tandem concept. The ambipolar diffusion originates to compensate any charge imbalance, but in negative ion sources the surface production of negative ions can compensate this imbalance in the extraction region reducing even more the electron diffusion.

3.3 Plasma sheath

The flux of charged particles onto a surface (e.g. the PG) is affected by the topology of the magnetic field and physical parameters such as the density and temperatures of the species present in the plasma. However, this flux is also affected by the formation of a non quasi-neutral plasma region in direct vicinity of the PG surface, denominated plasma sheath, marking the transition between the quasi-neutral plasma and the containing walls. To understand the causes and properties of the plasma sheath a simplified model is helpful for a first insight.

Let's consider a collisionless low temperature plasma in a 1D domain, without magnetic fields, formed by two species: electrons and positive ions, and a grounded perfectly conductive planar wall which absorbs all the impacting charged particles. In a low temperature plasma, the electron temperature is higher than the ion temperature ($T_{\mathrm{e}} \gg T_{\mathrm{i}}$) [40]. Since additionally the electron mass is small compared to the ion mass, the thermal velocity of the electrons, $v_{\mathrm{e}} = \sqrt{\frac{k_{\mathrm{B}} T_{\mathrm{e}}}{m_{\mathrm{e}}}}$, is higher than the thermal

velocity of the ions, $v_{\mathrm{i}} = \sqrt{\frac{k_{\mathrm{B}} T_{\mathrm{i}}}{m_{\mathrm{i}}}}$. Electrons will reach the absorbing surface at a higher rate compared to the ions. The charge imbalance in the plasma occasioned by the fast electrons will produce an electrostatic potential drop Φ according to Poisson's equation:

$$\triangle\Phi = -\frac{\rho}{\varepsilon_0} = \frac{e(n_{\mathrm{e}} - n_{\mathrm{i}})}{\varepsilon_0}, \tag{3.7}$$

where ρ is the charge density, e the elemental electric charge, n_{i} the positive ion density, n_{e} the electron density and ε_0 is the space vacuum permittivity. This potential drop generates an electric field accelerating positive ions onto the surface while decelerating electrons. A steady state is reached when the quasi-neutrality in the plasma is recovered. To reach this state the flux of positive ions and electrons to the surface must be equalized, i.e. ambipolar diffusion from the plasma onto the surface has to take place. To equal these fluxes a positive electrostatic potential drop from the plasma to the absorbing surface has to be developed; this potential drop is produced by a layer with positively electrical charge between the quasi-neutral plasma and the surface, as shown in figure 3.1. This layer is called "plasma sheath". Any isolated charge in the plasma is screened to a length $\lambda_D = \sqrt{\frac{\varepsilon_0 k_B T_e}{e n_e}}$, called Debye length [39]. Therefore, the extension of the plasma sheath is also in the order of several λ_D. For example, for $\mathrm{T_e} = 1$ eV and $\mathrm{n_e} = 10^{16}$ m^{-3} the Debye length is $\lambda_D = 7.4{\cdot}10^{-5}$ m and the plasma sheath extends to $\sim 8\lambda_D$ [41].

The energy conservation equation for the positive ions from the plasma to the sheath is:

$$\frac{m_{\mathrm{i}} u^2(x)}{2} = \frac{m_{\mathrm{i}} u_{\mathrm{sh}}^2}{2} - e\Phi(x), \tag{3.8}$$

where u_{sh} is the ion velocity entering the sheath. The continuity equation for the ion flux in the sheath is:

$$n_i(x) u(x) = n_{\mathrm{i,sh}} u_{\mathrm{sh}} \tag{3.9}$$

From equations 3.8 and 3.9 it is obtained:

$$u(x) = \sqrt{u_{\mathrm{sh}}^2 - \frac{2e\Phi(x)}{m_{\mathrm{i}}}}, \tag{3.10}$$

$$n_{\mathrm{i}}(x) = \frac{n_{\mathrm{i,sh}}}{\sqrt{1 - \frac{2e\Phi(x)}{u_{\mathrm{sh}}^2 m_{\mathrm{i}}}}}. \tag{3.11}$$

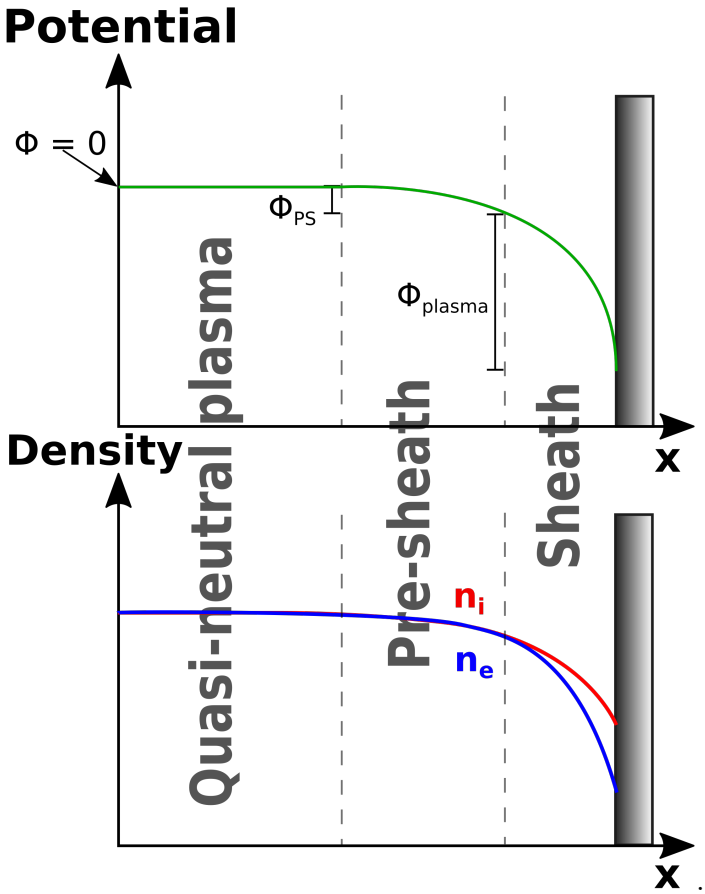

Figure 3.1: In the interface between the quasi-neutral plasma ($n_i = n_e$) and the absorbing wall two regions can be identified: a quasi-neutral pre-sheath region marked by a potential drop Φ_{PS} and the positively charged sheath region producing a potential drop Φ_{plasma}.

Considering the higher velocity of the electrons, an equilibrium state between electrons can be assumed. Therefore a Boltzmann relation is used for the electron density:

$$n_{\mathrm{e}}(x) = n_{\mathrm{e,sh}} e^{\frac{-e\Phi(x)}{k_{\mathrm{B}} T_{\mathrm{e}}}}. \tag{3.12}$$

Setting $n_{\mathrm{e,sh}} = n_{\mathrm{i,sh}} = n_{\mathrm{sh}}$ at the sheath edge and substituting n_i and n_e into Poisson's equation:

$$\frac{d^2\Phi}{dx^2} = \frac{e n_{\mathrm{sh}}}{\varepsilon_0} \left(e^{\frac{-e\Phi(x)}{k_{\mathrm{B}} T_{\mathrm{e}}}} - (1 - \frac{\Phi}{E_{\mathrm{s}}})^{-\frac{1}{2}} \right), \tag{3.13}$$

with $E_{\mathrm{s}} = \frac{m_{\mathrm{i}} u_{\mathrm{s}}^2}{2}$, and multiplying by $\frac{d\Phi}{dx}$ and integrating over x it is obtained:

$$\frac{1}{2}\left(\frac{d\Phi}{dx}\right)^2 = \frac{en_{\rm sh}}{\varepsilon_0}\left(k_{\rm B}T_{\rm e}e^{\frac{-e\Phi(x)}{k_{\rm B}T_{\rm e}}} - k_{\rm B}T_{\rm e} + 2E_{\rm s}\left(1-\frac{\Phi}{E_{\rm s}}\right)^{\frac{1}{2}} - 2E_{\rm s}\right), \tag{3.14}$$

where it has been set $\Phi = 0$ and $\frac{d\Phi}{dx} = 0$ at $x = 0$, corresponding to a field free plasma. For the equation 3.14 the right hand side should be positive for a solution to exist. Physically, this means that the electron density must always be lower than the ion density in the plasma sheath region. Expanding the right side until the second order in a Taylor expansion, we obtain a condition for $u_{\rm sh}$:

$$u_{\rm sh} \geq u_{\rm B} = \sqrt{\frac{k_{\rm B}T_{\rm e}}{m_{\rm i}}}, \tag{3.15}$$

where the velocity $u_{\rm B}$ is denominated Bohm velocity, as this criteria was first derived by Bohm [42]. For the ions to reach this velocity, a pre-sheath potential drop must accelerate the ions with $\Phi_{\rm PS} = \frac{k_{\rm B}T_{\rm e}}{2}$.

Finally, taking $u_{\rm sh} = u_{\rm B}$, the minimum value for the potential drop $\Phi_{\rm plasma}$ within the sheath between the quasi-neutral plasma and the wall can be determined. Equating the ion flux, $\Gamma_{\rm i} = n_{\rm sh}u_{\rm B}$, to the electron flux at the wall, $\Gamma_{\rm e} = \frac{n_{\rm sh}\bar{v}_{\rm e}}{4}e^{\frac{-e\Phi_{\rm plasma}}{k_{\rm B}T_{\rm e}}}$ with $\bar{v}_{\rm e} = (\frac{8eT_{\rm e}}{\pi m_{\rm e}})^{\frac{1}{2}}$, $\Phi_{\rm plasma}$ can be found:

$$\Phi_{\rm plasma} = -k_{\rm B}T_{\rm e}\ln\left(\sqrt{\frac{m_{\rm i}}{2\pi m_{\rm e}}}\right). \tag{3.16}$$

The simplest formulation of the plasma sheath potential drop (plasma potential) is $\Delta\Phi = \Phi_{\rm plasma} + \Phi_{\rm PS} = \frac{k_{\rm B}{\rm T_e}}{2}\left(\ln\left(\frac{2\pi m_{\rm e}}{m_{\rm i}}\right) + 1\right)$. It gives the basic linear trend of it respect to the electron temperature and the logarithmic dependence respect to the masses of the species composed by the plasma.

3.4 Double layer

For the negative ion sources the strong surface emission of negatively charged particles from the surface affects the plasma sheath. These negative charged particles can be secondary electrons released from the surface by impinging electrons or negative ions produced by surface conversion.

In the case of a normal plasma sheath the plasma potential re-adjusts to equate the flux of electrons $\Gamma_{\rm e}$ and positive ions $\Gamma_{\rm i}$ from the plasma onto the containing walls, and in this way it keeps the plasma beyond the plasma sheath quasi-neutral. The surface emission of secondary electrons and the the negative ion surface production

add a flux Γ_{SE} and Γ_{NI} respectively, from the surface into the plasma. The flux equilibrium in this scenario is given by:

$$\Gamma_i = \Gamma_e - (\Gamma_{NI} + \Gamma_{SE}). \tag{3.17}$$

A decrease in the potential drop is expected as the positive ion flux needed for reaching the equilibrium is lower, as shown in equation 3.17, and a lower potential drop is sufficient to provide the required acceleration to the positive ions towards the surface. The loss of electrons onto the walls is partly compensated by the surface emitted negatively charged particles.

An analysis of the plasma potential including the effects of the ion temperature and the emission of secondary electrons was done by P. Stangeby [43] modifying the equation 3.16 to obtain:

$$\Phi_{plasma} = \frac{k_B T_e}{2e} \ln\left(\frac{2\pi m_e}{m_i}\left(1 + \frac{T_i}{T_e}\right)(1-\gamma)^{-2}\right), \tag{3.18}$$

where $T_i > 0$ is the ion temperature and γ the secondary electron emission coefficient. From equation 3.18 it can be seen that as γ increases, Φ_{plasma} will decrease as expected.

If the emission rate is increased, the negative charge accumulation in front of the surface can neutralize the positive charge of the plasma sheath in a immediate layer in front of the surface. At this point a null electric field in front of the surface is present. If the flux of negative charged particles from the surface is increased beyond the critical value Γ_{SEC}, at which the electric field in front of the surface is already null, an accumulation of negatively charged particles in front of the surface takes place, producing a layer of negative charge density. This second layer next to the positive charged sheath layer produces an inversion of the electrostatic potential, as seen in figure 3.2, and this structure is denominated "potential well".

The potential well in front of the surface limits the amount of negatively charged particles into the plasma, as any negative ion with a kinetic energy lower than Φ_{well} is reflected back onto the surface. Studies done by Wünderlich [44] and McAdams [45] have shown that the flux of negative ions into the plasma can be space charge limited in negative ion sources, even if the emission rate is increased, as result of the formation of the potential well.

Additionally, changes in other plasma parameters are expected when a potential well is formed. For example, a reduction in the electron flux onto the surface due to the potential well increasing the energy required by the electron to overcome the potential barrier formed by the plasma potential and the potential well. To understand the

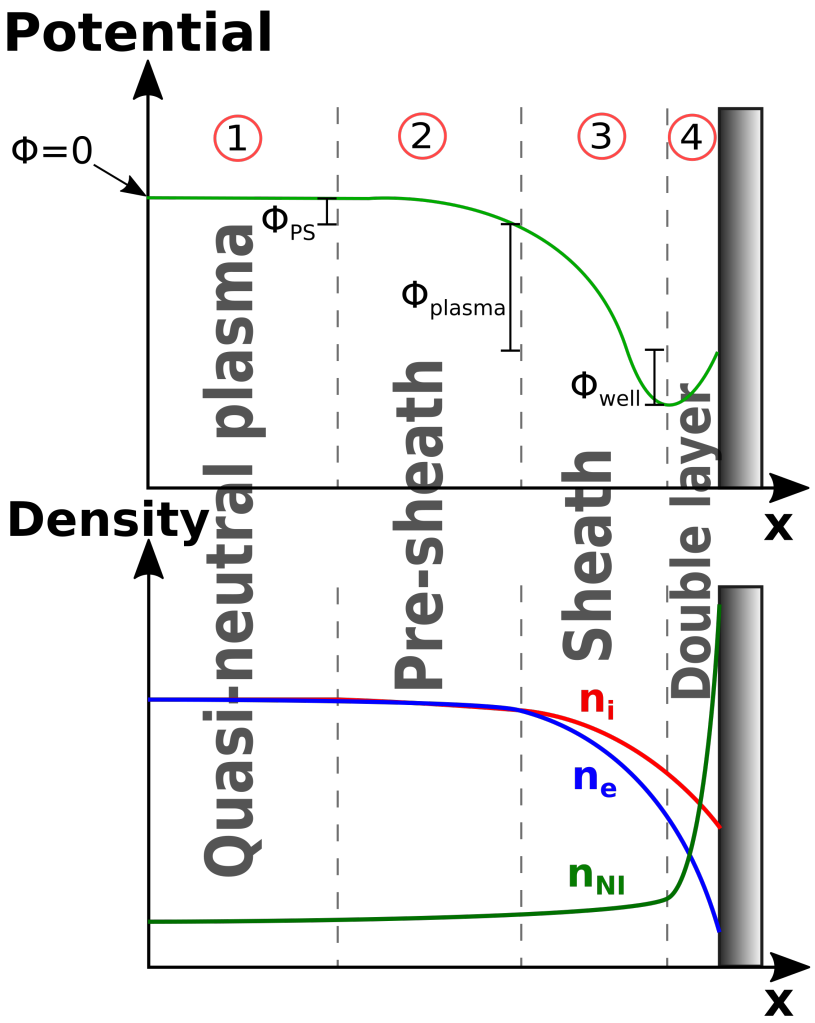

Figure 3.2: Plasma potential and density as function of the distance to the surface for a double layer scenario. 4 regions can be distinguished: 1) quasi-neutral plasma ($n_\mathrm{i} = n_\mathrm{e} + n_\mathrm{NI}$), 2) pre-sheath, a potential drop Φ_PS with respect to the quasi-neutral plasma ($n_i = n_e + _{NI}$), 3) sheath with a potential drop Φ_plasma with respect to the pre-sheath ($n_i > n_e + _{NI}$) and 4) Double layer with a potential drop Φ_well with respect to the sheath ($n_i < n_e + n_\mathrm{NI}$).

whole system, complete kinetic models capable to model the plasma sheath formed by the fluxes of particles from the plasma and from the surface are mandatory.

3.5 Negative ion extraction

The extraction process of negative ions from the plasma consists on applying a high positive voltage V_ex between the EG and the PG. The produced electric field penetrates into the plasma through the extraction apertures. An equilibrium is found

between the forces applied to the plasma due to the pressure gradient and the electric field. Figure 3.3 shows a schematic of the equilibrium. The boundary surface called meniscus defines the separation between the quasi-neutral plasma and the extracted particles forming the beam. In the plasma side the electric field applied to extract the negative ions is screened; any particle crossing the meniscus is extracted and accelerated by the electric field between the PG and EG.

The meniscus shape influences the beam formation as the initial acceleration of the extracted particle by the electric field is perpendicular to the meniscus surface. The divergence angle α_{i} of a particle in the direction i = y,z is defined by $\tan(\alpha_{\mathrm{i}}) = \frac{v_{\mathrm{i}}}{v_{\mathrm{x}}}$, where v_x is the particle velocity in the beam direction. The divergence of the beam is given by the average divergence of all the N particles forming the beam $<\alpha_{\mathrm{i}}>=\sqrt{\frac{1}{N}\sum^{N}(\alpha_{\mathrm{i}})^2}$. The divergence indicates how much the beam spread in a force free situation. However, if external electric or magnetic fields are applied the divergence of the beam can be changed. The beam rms-emittance $\epsilon_{\mathrm{rms,i}} = \sqrt{<\alpha_{\mathrm{i}}^2><i^2> - <i\alpha_{\mathrm{i}}>}$ is the standard parameter used to measure the spatial and velocity spread of the beam.

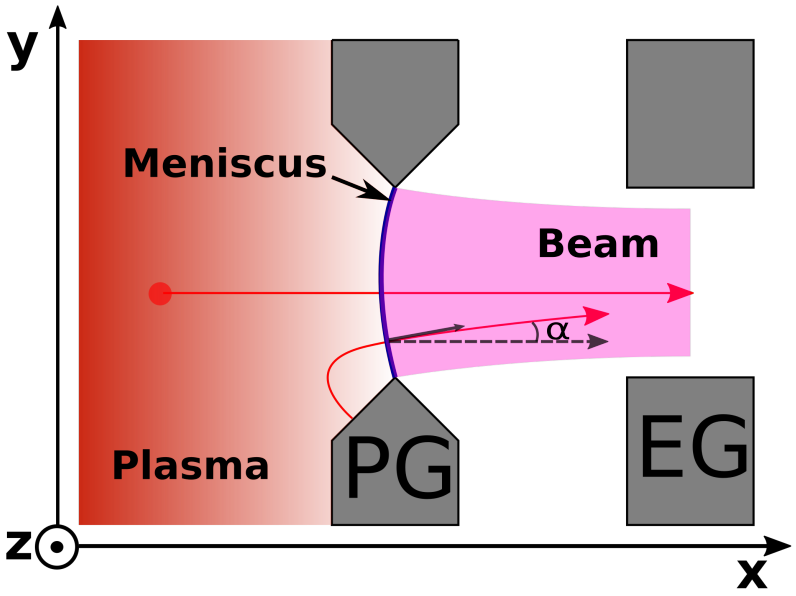

Figure 3.3: Schematic of the meniscus formation as boundary between the plasma and the beam.

Besides the optics of the beam the meniscus also defines the maximum current that can be extracted. In a negative ion source the extracted current through one aperture depends on the flux of particles through the meniscus. This flux depends on the density and temperature of the particles being extracted, and the total extracted

current depends then on the meniscus surface area. The surface area of the meniscus depends on several parameters such as the geometry of the extraction aperture and its curvature.

The Child-Langmuir law [46] gives the maximum current density $j_{\max}$ that can be extracted from a planar emitting surface applying a potential V_{ex}, when the electric field immediately after the emitting surface is screened by the space charge of the emitted particles:

$$j_{\max} = \frac{4}{9}\varepsilon_0 \sqrt{\frac{2q_{\text{s}}}{m_{\text{s}}}} \frac{V_{\text{ex}}^{\frac{3}{2}}}{d^2}, \tag{3.19}$$

where d is the distance between the planar emitting surface and the EG. Even though some assumptions in the derivation of this law are not strictly valid for the ion sources, such as the initial velocity of the particles not being zero, the physics of the space charge limit is still applied for estimation purposes. Thus, in any system the maximum extracted current also depends on the applied voltage difference and distance between grids.

The meniscus surface can also be changed by varying the extraction voltage. An increase of the extraction voltage would produce a more penetrating electric field which increases the curvature and surface of the meniscus. However, increasing the meniscus curvature would affect the beam divergence, as seen in figure 3.4. A low extraction voltage would produce a convex meniscus, producing a divergent beam; a high extraction voltage produces an over-focused beam which if the focus point is before the EG, the beam is considered divergent. The extraction voltage has to be chosen to avoid any of the two extreme cases to obtain a minimum divergence.

It has been empirically seen that there is a relation between the beam divergence and the perveance. The perveance Π is defined from the Child-Langmuir law as

$$\Pi = \frac{j_{\max}}{V_{\text{ex}}^{\frac{3}{2}}} = \frac{4}{9}\sqrt{\frac{2q_{\text{s}}}{m_{\text{s}}}} \frac{\varepsilon_0}{d^2}. \tag{3.20}$$

Perveance scans are done in the test facilities by varying either extraction voltage or the extracted current. For example, if V_{ex} is kept constant and the RF power is increased, then Π increases. Increasing the RF power enhance the production of negative ions by volume and surface processes, and therefore $j_{\max}$ increases. On another side, if the extracted current is kept constant and V_{ex} is increased, then Π decreases.

Experimental results of a perveance scan show a parabolic dependence of the divergence with respect to the perveance, as shown in figure 3.5. Three regimes

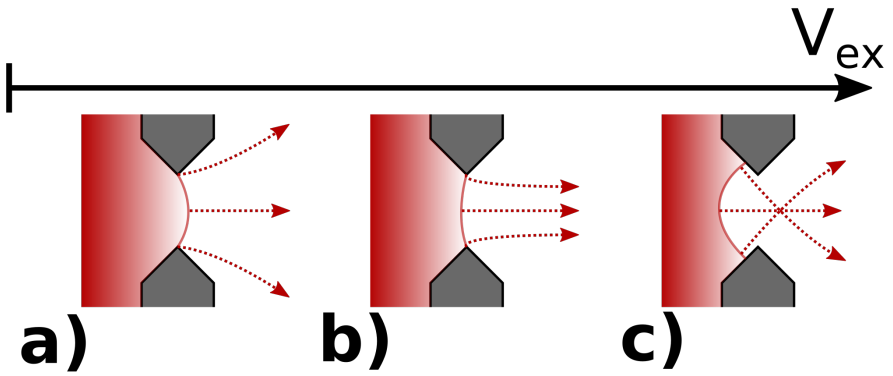

Figure 3.4: Diagram of the evolution of the shape of the meniscus as function of the extraction voltage. a) Convex meniscus: a divergent beam is extracted; b) Planar meniscus: the extracted beam is parallel; c) Concave meniscus: the beam is convergent.

can be distinguished: under-perveance, perveance optimum and over-perveance. The dependence of the divergence with the perveance is qualitatively explained by figure 3.4. Assuming the extracted current is kept constant, then starting in the over-perveance regime with low values of V_{ex} the meniscus shape is convex (figure 3.4a), producing a beam with a high divergence. For increasing values of V_{ex} the regime goes through a minimum divergence (figure 3.4b), and further increasing V_{ex} pass to a situation with a concave meniscus (figure 3.4c), producing a divergent beam and entering the under-perveance regime. The beam divergence measured in perveance scan is usually for the acelerated beam. However, the beam divergence can be altered by electrostatic lenses as those generated by a multi-aperture multi-grid extraction system, as those in the test facilities.

Figure 3.6 shows a schematic of the extraction and acceleration system for a beamlet of a negative ion source. The co-extracted electrons are dumped onto the EG by a magnetic deflection field in order to avoid its full acceleration. The remaining negative ion beam moves through the acceleration phase. The electrostatic lenses generated in the acceleration phase (e.g. near the EG and GG) modify the beam divergence through the beam line. The electrostatic potential at the entrance and exit of the EG and GG acts as biconcave lenses for the beam. The curvature of this lenses can be modified by changing the distances or the potential difference between each grid, i.e. between the PG and EG (V_{ex}) and between the EG and the GG (V_{acc}). Besides, the addition of more acceleration phases allows to modify the beam divergence.

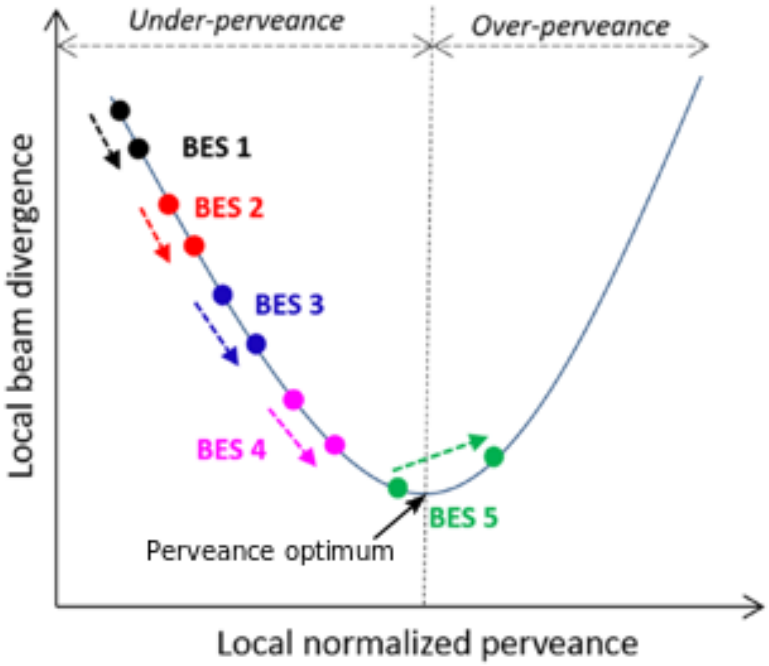

Figure 3.5: Schematic evolution of the divergence measured by beam emission spectroscopy (BES) during a perveance scan [47].

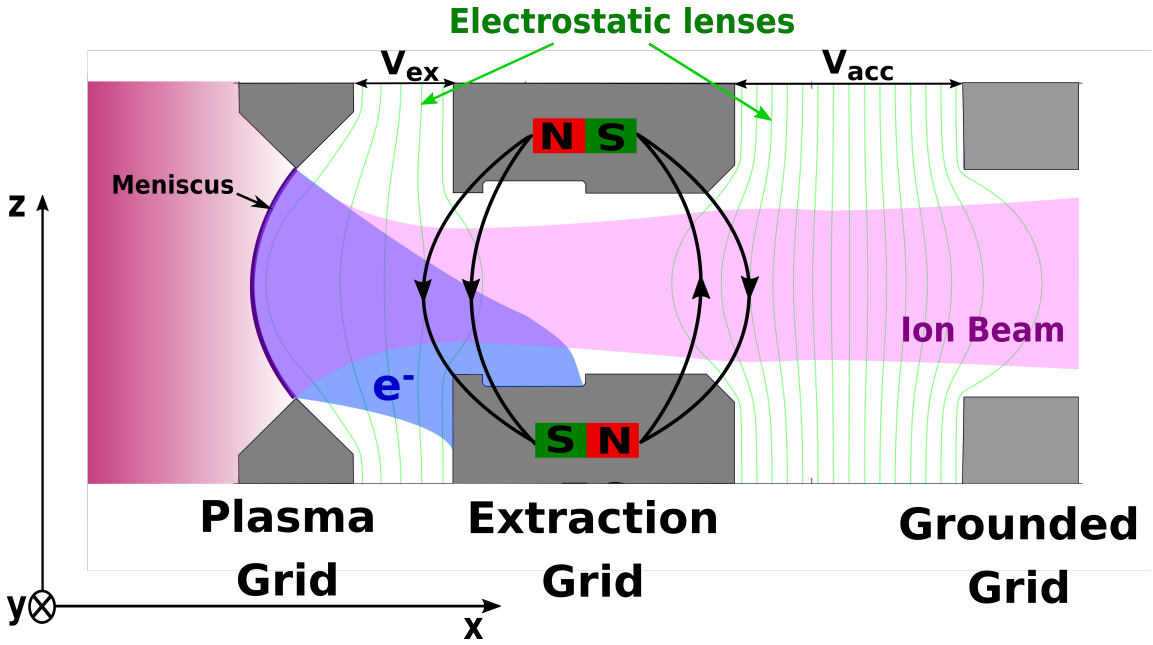

Figure 3.6: Shown are the extraction system composed by three grids: plasma grid, extraction grid and grounded grid.

Chapter 4

PIC modeling for negative ion extraction

An adequate numerical model of the extraction region in negative hydrogen ion sources for NBI has to be capable of solving self-consistently the physics in the extraction region, accounting for aspects such as the plasma sheath and the charged particle diffusion through the magnetic field. In the plasma sheath the electrons are not thermalized and their energy distribution cannot be assumed to be Maxwellian, thus, this case demands kinetic models. A kinetic model does not require the assumption of a specific energy distribution, which is instead obtained as an output.

A kinetic model applied to the extraction region allows for an extensive parametric study over the influence of physical parameters such as density, temperature and specie (isotope) composition. Besides, parameters of the ion source such as the magnetic field configuration or the extraction aperture geometry can be easily varied in numerical models. This approach can give then a more detailed understanding of the physical processes that can lead to an improvement of the extracted current in order to reach the ITER-NBI requirements.

Particle In Cell (PIC) models are the best option for modeling the extraction region in negative ion sources. For example, a PIC model does not need to assume the flux of particles on the surfaces containing the plasma as in fluid models, allowing to model self-consistently the meniscus surface. The kinetic nature of PIC models gives a detailed picture of the plasma dynamics starting from the given initial and boundary conditions. The initial conditions for the plasma parameters such as density and temperature can be obtained from the installed diagnostics at the existing NBI test facilities.

4.1 Particle In Cell method

The PIC method is used to solve a system of kinetic equations describing the dynamics of a plasma [48]. In its most general form the model solves for a collisionless plasma the system composed by Vlasov and Maxwell equations.

For densities and temperatures as those found in plasmas inside negative ion sources for fusion the electrostatic approximation is valid. In the electrostatic approximation it is assumed that the magnetic field does not change with time. The magnetic field in the extraction region is mainly generated by a external source, and it is much higher than that generated by the extracted ion current. For example, assuming an extracted current density of 329 Am^{-2} with an aperture radius of 7 mm, the produced magnetic field is $\sim$0.004 mT while the external magnetic field is $\sim$5 mT in the extraction region; thus, the magnetic field can be considered constant. This approximation reduces Maxwell equations to Poisson's equation [48]. In this way the system of equations to be solved is reduced to equation 4.1 for the plasma evolution (Vlasov equation), equation 4.2 for the electrostatic electric field (Poisson's equation) and the charge distribution given by equation 4.3:

$$\frac{\partial f_\mathrm{s}}{\partial t} + \mathbf{v}\cdot\nabla_\mathbf{x} f_\mathrm{s} + \frac{q_\mathrm{s}}{m_\mathrm{s}}(\mathbf{E}+\mathbf{v}\times\mathbf{B})\cdot\nabla_\mathbf{v} f_\mathrm{s} = 0, \tag{4.1}$$

$$\triangle\Phi = -\frac{\rho}{\varepsilon_0}, \tag{4.2}$$

$$\rho = \sum_\mathrm{s} q_\mathrm{s} \int f_\mathrm{s} d\mathbf{v}, \tag{4.3}$$

where $f_\mathrm{s} \equiv f_\mathrm{s}(\mathbf{x},\mathbf{v},t)$ is the phase-space distribution function of a particle of specie s, Φ is the electrostatic potential, $\mathbf{E} = -\nabla\Phi$ is the macroscopic electric field, $\mathbf{B}$ is the magnetic field (external input) and ρ is the charge density.

The numerical solution approach of the PIC method consists in approximating the function f_s by a sum of quasi-particles p in the phase-space, i.e. $f_\mathrm{s}(\mathbf{x},\mathbf{v},t) = \sum_\mathrm{p} f_\mathrm{p}(\mathbf{x},\mathbf{v},t)$. Each quasi-particle represents a large number N_p of real particles. The distribution of each quasi-particle over the phase-space is given by the shape functions S_x over the configuration space and S_v over the velocity space. In this way the distribution of each quasi-particle is:

$$f_\mathrm{p}(\mathbf{x},\mathbf{v},t) = N_\mathrm{p} S_\mathrm{x}(\mathbf{x}-\mathbf{x_p}(t)) S_\mathrm{v}(\mathbf{v}-\mathbf{v_p}(t)), \tag{4.4}$$

where $\mathbf{x}_\mathrm{p}$ and $\mathbf{v}_\mathrm{p}$ represent the center of the shape functions which are required to be symmetrical and normalized.

In the standard PIC method a delta function is used as shape function over the velocity space, $S_\mathrm{v}(\mathbf{v} - \mathbf{v_p}(t)) = \delta(\mathbf{v} - \mathbf{v_p}(t))$. Therefore, the shape function over the configuration space remains constant over time [48]. For the spatial shape function S_x, b-splines are commonly used [48].

The integration of the moments of the Vlasov equation gives the equations for the temporal evolution of the quasi-particles. The integration of the zero order moment gives the equation:

$$\frac{dN_\mathrm{p}}{dt} = 0, \tag{4.5}$$

meaning that the total number of particles N_p represented by the quasi-particle is constant over time.

The first moment of Vlasov equation multiplied by $\mathbf{x}$ gives:

$$\frac{d\mathbf{x}_\mathrm{p}}{dt} = \mathbf{v}_\mathrm{p}, \tag{4.6}$$

meaning that the movement of a quasi-particle is such as that of a particle with position $\mathbf{x_p}$ and velocity $\mathbf{v_p}$.

The first moment of Vlasov equation multiplied by $\mathbf{v}$ gives:

$$\frac{d\mathbf{v_p}}{dt} = \frac{q_s}{m_s}(\mathbf{E} + \mathbf{v_p} \times \mathbf{B}), \tag{4.7}$$

meaning that the dynamics of a quasi-particle is the same as that of a particle of specie s under the influence of fields $\mathbf{E}$ and $\mathbf{B}$.

The fields such as ρ, Φ and $\mathbf{E}$ are calculated over a numerical grid (mesh) that extends through the system domain. The values for each field are calculated at each point of the mesh. The charge density $\rho(\mathbf{x}, t)$ is obtained from the projection of the quasi-particles charge onto the mesh, using equation 4.3 and the shape function S_x. The electrostatic potential Φ is obtained by solving Poisson's equation (equation 4.2) over the numerical grid using methods for hyperbolic differential equations. The electric field $\mathbf{E}$ is obtained by a numerical differentiation of Φ over the mesh.

Once $\mathbf{E}$ has been calculated over the mesh, it can be interpolated in order to obtain the electric field $\mathbf{E}_\mathrm{p}$ at a quasi-particle position:

$$\mathbf{E}_\mathrm{p} = \int S_\mathrm{x}(\mathbf{x} - \mathbf{x_p})\mathbf{E}. \tag{4.8}$$

The same procedure is used for calculating the magnetic field $\mathbf{B}_p$ at the particle position, using the external input for the magnetic field $\mathbf{B}$ at each point of the mesh. The quasi-particle movement, described by equations 4.6 and 4.7, can be solved numerically for a time step Δt, thus moving the initial system from time t_0 to $t_0 + \Delta t$.

The procedure for a time iteration integration of the initial system, shown in figure 4.1, can be summarized as: 1) projection of the charge density of the particle over the numerical mesh, 2) integration of Poisson's equation, 3) calculation of the electric field, 4) interpolation of the electric and magnetic fields to the particles position and 5) temporal integration of the dynamic equations of the quasi-particles.

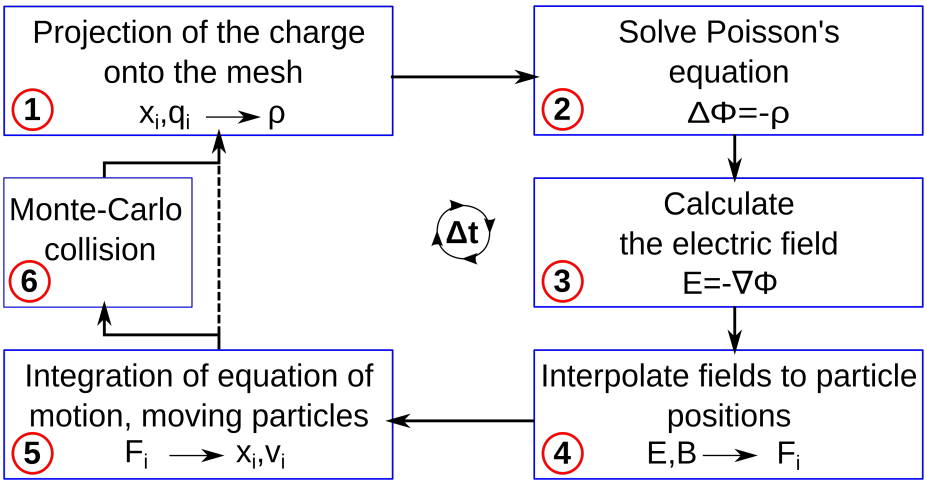

Figure 4.1: Scheme of a PIC cycle. For each particle i: 1) their charge q_i is projected onto the mesh according to their position x_i; 2) The electrostatic potential Φ is determined from the plasma charge density ρ;) The electric field E is calculated; 4) The electrostatic force F_i is interpolated; 5) The new position x_i and velocity v_i are calculated; 6) Collisional processes are evaluated.

Short-range particle-particle interactions are neglected in the standard PIC model, as the initial equations solved in a PIC model do not account for collisions between particles. Chemical reactions and velocity scatterings associated with an inter-particle interaction, of a range shorter than the mesh spacing $\Delta\mathbf{x}$, can be included in the model by a collision module [49] based on the Monte-Carlo method. The collisions are evaluated after the dynamic equations of the quasi-particles are solved.

The Monte-Carlo method [49] first calculates the probability for a process l given by:

$$P_{\mathrm{coll},l} = 1 - \exp\left(-n_{\mathrm{target}}\sigma_l(E_{\mathrm{i}})|\mathbf{v}_{\mathrm{i}}|\Delta t\right), \tag{4.9}$$

where n_{target} is the density of the target with which the particle is colliding, σ_l is the cross section of the process l at the incident particle energy E_{i} (with respect to the center of mass) and $\mathbf{v}_{\mathrm{i}}$ is the incident particle velocity. The calculated probability $P_{\mathrm{coll},l}$ is compared to a random number R_1 from an uniform probability distribution between zero and one. If $R_1 < P_{\mathrm{coll},l}$ the process associated with σ_1 takes place in the time interval Δt.

The presented version of the Monte-Carlo method assumes $n_{\mathrm{target}} \gg \mathrm{n_p}$, where n_{p} is the density of the incident particle specie. In this case the target acts as thermal bath and the effect of collisions on the target is considered negligible. Each quasi-particle is treated as a real single particle implying a high collisional rate due to the quasi-particle representing a bigger amount of real particles.

The processes with higher cross sections in plasmas inside negative ion sources for fusion to which the Monte-Carlo method can be applied are: electron scattering with the background gas, associative detachment (equation 2.7) and collisional detachment (equations 2.8 and 2.9). For the velocity scattering processes of electrons with the background gas, the velocity of the incident particle is reset randomly according to the thermal distribution of the species.

A different model has to be applied to model the momentum transfer between charged particles due to the Coulomb interaction, in order to ensure preservation of the momentum and energy of the particles involved. A binary collision method for Coulomb collisions, preserving momentum explicitly and energy implicitly, was developed by Takizuka and Abe [50]. This method pairs the charged particles inside a mesh cell of the domain. For each pair of particles A and B their relative velocity $\mathbf{u}_{\mathrm{rel}} = \mathbf{v}_{\mathrm{A}} - \mathbf{v}_{\mathrm{B}}$ is rotated in the rest frame of the incident particle. Figure 4.2 shows the rotation of the relative velocity by $\Delta\mathbf{u}_{\mathrm{rel}}$ with the angles Θ and Ψ in the rest frame.

The angle Θ is calculated by:

$$\Theta = 2\tan^{-1}(\delta), \tag{4.10}$$

where δ is originated from a Gaussian distribution with mean equal to zero and a variance $\langle\delta^2\rangle$ given by:

$$\langle\delta^2\rangle = \frac{q_{\mathrm{A}}^2 q_{\mathrm{B}}^2 n_{\mathrm{L}} \Lambda_{\mathrm{C}}}{8\pi\varepsilon_0^2 m_{\mathrm{AB}}^2 u_{\mathrm{rel}}^3}\Delta t, \tag{4.11}$$

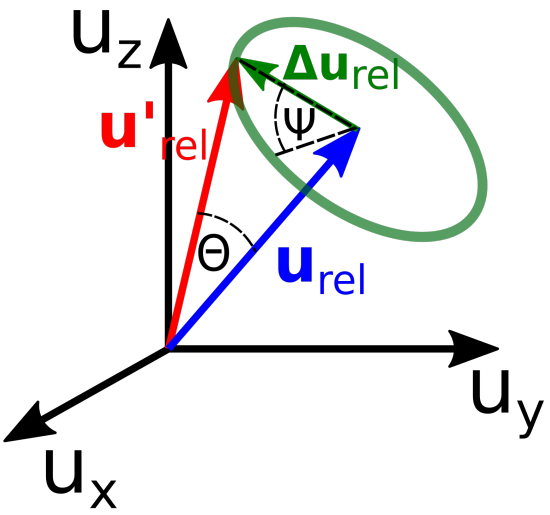

Figure 4.2: Schematic representation of the scattering of the relative velocity $\mathbf{u}_{\mathrm{rel}}$ by the angles Θ and Ψ, taking place during Coulomb collisions.

where q_{A} and m_{A} are the charge and mass of particle A; q_{B} and m_{B} are the charge and mass of particle B; n_{L} is the lower density between that of species A and B; Λ_{C} denotes the Coulomb logarithm [51], and $m_{\mathrm{AB}} = \frac{m_{\mathrm{A}} m_{\mathrm{B}}}{m_{\mathrm{A}}+m_{\mathrm{B}}}$. The angle Ψ is taken from a random uniform distribution in the range between 0 and 2π.

This process represents a binary collision where the magnitude of the relative velocity is unchanged but its direction is altered. The particles velocities are updated for each time step Δt by:

$$\mathbf{v}_{\mathrm{A}}^{t+\Delta t} = \mathbf{v}_{\mathrm{A}}^{t} + \frac{m_{\mathrm{AB}}}{m_{\mathrm{A}}} \Delta \mathbf{u}_{\mathrm{rel}}, \tag{4.12}$$

$$\mathbf{v}_{\mathrm{B}}^{t+\Delta t} = \mathbf{v}_{\mathrm{B}}^{t} - \frac{m_{\mathrm{AB}}}{m_{\mathrm{B}}} \Delta \mathbf{u}_{\mathrm{rel}}. \tag{4.13}$$

4.2 Stability criteria for explicit PIC method

Stability criteria have been deduced for the numerical parameters used in PIC models [48], such as the mesh size $\Delta \mathbf{x}$, time step Δt and the number of quasi-particles per mesh cell (PPC). These criteria give a range for the numerical parameters, in which the results of the model accurately describe the plasma physics and reduce any numerical perturbation.

Mesh size: The mesh size has to be of the order of the Debye length in a range between $0.3\lambda_{\mathrm{D}}$ and $3\lambda_{\mathrm{D}}$. The physical reason is that the global behavior of the

plasma, scope of a PIC model, takes place at distances larger than λ_D. Beyond λ_D any punctual charge is screened by the plasma. The lower limit of $0.3\lambda_D$, proven by [52], establishes that smaller mesh sizes bring numerical perturbations. The upper limit proven theoretically by [48] for a first order spline shape function S_x in an explicit PIC model, establishes that the use of a mesh size larger than $3\lambda_D$ produces numerical instabilities resulting in non-physical results.

Time step: The time step used for the cycle iteration has to be sufficiently small in order to describe the highest frequency of the global behavior in a plasma. The electron density oscillations have one of the highest frequencies in a plasma, it is given by $\omega_{pe} = \sqrt{\frac{n_e e}{m_e \varepsilon_0}}$, where n_e is the electron density, m_e is the electron mass and e the electron charge. The time step for the PIC cycle must then be smaller than the inverse of this frequency to solve properly this phenomenon. A more strict restriction to Δt is defined in [48] where is stated that for the proper description of the movement of particles in presence of plasma oscillations, Δt has to be smaller than $0.3\omega_{pe}^{-1}$.

CFL condition: The numerical parameters Δt and Δx are correlated by the Courant-Friedrich-Lewy (CFL) condition [53]. For a PIC model this condition is expressed as $v_{max}\Delta t < \Delta x$, where v_{max} is the velocity of the fastest particle in the system. The condition can be physically interpreted as requiring that a particle cannot cross over two mesh divisions in one time step.

PPC: A condition for the number of Particles Per mesh Cell (PPC) in the simulation is established to reduce the statistical noise, and therefore ensure that the physics is accurately reproduced. However, the necessary number of particles per cell depends on the used particle shape. For instance, with a particle shape S_x given by a spline of first order the suggested number of particles per mesh cell has to be larger than 10 [48] for a three dimensional spatial domain.

4.3 Approaches for the PIC modeling of negative ion sources

The initial applications of PIC models to negative ion sources for fusion used 1D, 2D or 3D configuration space depending on their focus of study. 1D models are useful to study qualitatively the behavior of the plasma in front of the PG surface; however, they cannot represent the extraction in a multi-aperture ion source. A 2D model can represent the extraction system and also allows to study the reduction in the plasma flow due to the magnetic filter field. Nonetheless, 2D models do not represent accurately an extraction aperture, as the 2D representation of an aperture is equivalent to

a slit in a 3D configuration. Besides, due to the 3D magnetic field topology resulting from the superposition of the magnetic filter fields and magnetic deflection field, the reduced 2D domain does not allow a study of the electron transport in the extraction region. Thus, a 3D simulation domain is mandatory to accurately represent the effects of the aperture geometry, the transport of electrons and the plasma distribution close to the meniscus.

The 1D PIC models were developed in [44][54], they gave an insight into the physics of the plasma transport close to the PG and evolution of the potential well. 2D models were initially developed in [55], these models were focused on the study of the electron and negative ion diffusion through a magnetic filter field. A 3D model was initially developed to model the whole source by [56][57], but the model presented a large mesh size comparatively to the extraction aperture diameter and did not fulfill the stability criteria for PIC models.

Ongoing improvements of computer processors and the increasing access to high performance computing (HPC) systems allow PIC models, respecting the stability criteria, in 2D, 2.5D (2D configuration space and 3D in velocity space) and 3D.

At Naruto University and Keio University, Japan, 2D and 2.5D PIC models for one extraction aperture have been applied to the study of the meniscus formation and its influence on the optics of the extracted beam [58][59]. In these models, the dimensions of the extraction aperture are reduced to decrease the calculation time.

A 2.5D PIC model was developed at CNR-Nanotec, Italy, for a domain accounting for the expansion chamber of the prototype source (BATMAN) from the driver exit until the EG [60]. However, to fulfill the stability criteria a scaling of the vacuum permittivity was used.

At the LAPLACE group, University of Toulouse, France, 2D and 2.5D PIC models are applied for basic studies of the beam [61]. The domain size used by the later models can be either that of the whole ion source or one extraction aperture. Nevertheless, these models use a significantly reduced plasma density (by a factor 10-1000) compared to the values measured in a negative ion source for fusion. The reduced density is used to decrease the calculation time. However, physical aspects such as the sheath length are modified by varying the density, and therefore representing a different physical scenario.

Currently, four different 3D PIC models are applied to the study of negative ion sources. The 3D PIC code “Keio-BFX” developed at Keio University has been applied to study the formation of an ion-ion plasma and the meniscus formation for a domain of one extraction aperture [62][63][64]. To reduce the calculation time

a scaling in the lengths of the extraction aperture is applied. The 3D PIC code "Bari-Ex"[65] developed at CNR-Nanotec has been applied to the simulation of the extraction system of the NIO1 ion source[66][67]. A 3D PIC model developed at LAPLACE has been applied to study the plasma transport from the driver to the PG using a scaled density [68].

The ONIX code developed at LPGP, France [69] and advanced at IPP-Garching [70] implements a 3D PIC model to simulate the volume around one extraction aperture of a NBI ion source. It posses a flexible geometry and can be applied to simulate the extraction aperture geometry of the test facilities BATMAN and ELISE. The input parameters such as the densities or lengths are not scaled. Input parameters, for the densities and temperatures of the species in the plasma, correspond to the values measured at the test facilities. However, typical calculation times are still high, requiring 180 hours in 4096 cores until steady state. Initially, it has been applied to the study of the extracted current and beam formation, and its dependence on the negative ion surface emission rate from the PG [71][72].

4.4 The 3D PIC-MCC code ONIX

ONIX implements an explicit 3D PIC model with a Monte-Carlo collision module (PIC-MCC). The implementation of the numerical methods as well as its verification was done by Mochalskyy [69]. It is parallelized using domain decomposition and the message passing interface (MPI). The initial simulations done with ONIX focused on the analysis of the extracted ion current [71], and proved to have predictive capabilities regarding the maximum extracted current in negative ion sources [72]. However, in these simulations a large numerical mesh size was used, not allowing a proper description of the plasma. This initial election for the numerical parameters was a compromise between the calculation time and the subject of study of the simulations. A computational optimization was realized by Revel et al [70], allowing to make simulations using a more refined mesh.

The computational optimized version of the ONIX code allowed to make simulations with a focus on the plasma behavior (e.g. plasma sheath and electron transport). However, a validation of the code for the plasma sheath and surface particle emission was needed. Then, the first step done as part of this project was the physical validation for the plasma physics, presented in chapter 5. Additionally, an optimal set of numerical parameters was identified. The validated ONIX code was used for simulations regarding the analysis of the plasma behavior, and its relation with unanswered

questions such as that of the isotope effect (see chapter 2), the results are presented as part of this work in chapter 6. A description of the current ONIX version is given in the following.

4.4.1 Simulation domain

Two different domains have been used for ONIX: first, the volume around one extraction aperture of a negative ion source; and second, a simplified domain used for validation purposes. Both domains are in a 3D space.

The extraction aperture domain is shown in 4.3. It extends ∼2 cm into the plasma side and until the beginning of the EG. Periodic boundary conditions are applied in the directions parallel to the PG (i.e. y and z). Thus, this configuration is representative of an infinite array of apertures, but without the inversed polarity of the deflection each other aperture. This approximation can then be considered valid for one of the inner apertures of a beamlet group of the PG in the test facilities.

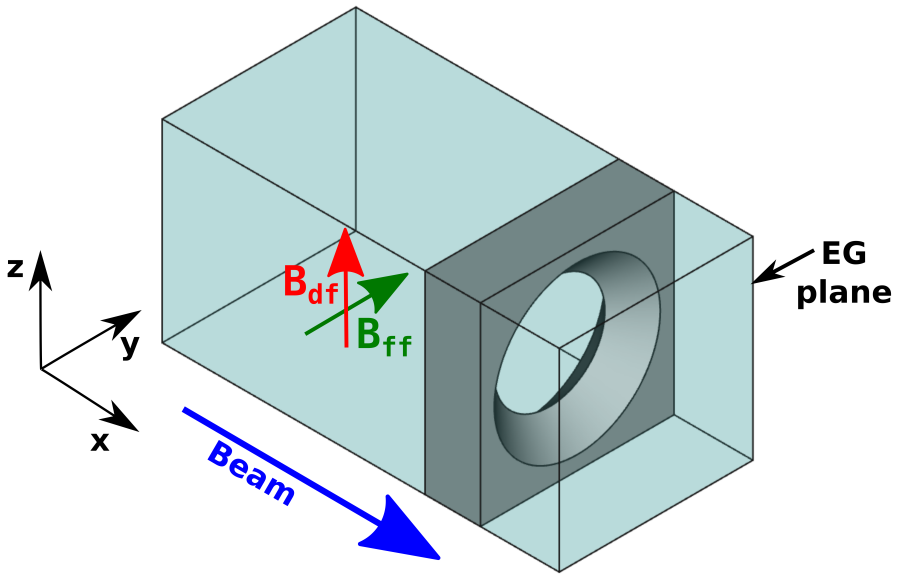

Figure 4.3: 3D domain used in ONIX for the simulation of one extraction aperture. The aperture geometry corresponds to the system used in the BATMAN test facility. The magnetic filter field (FF) and deflection field (DF), perpendicular to each other, break the symmetry in the system.

Two different setups of the extraction aperture domain are available, accounting for the geometries of the BATMAN (used up to 2016) and the ELISE test facility. The main differences between the two geometries are the wider aperture diameter in ELISE and the larger distance between the PG and the EG at ELISE. Figure 4.4

shows the 2D middle plane cut of these domains. In each case a source region is defined: a space in which particles are initially loaded and injected at each time step of the simulation.

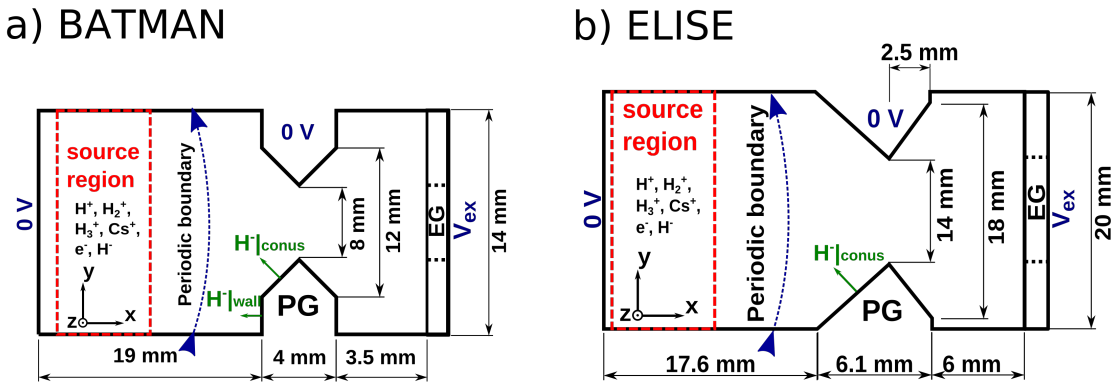

Figure 4.4: Transversal cut of the extraction aperture domain used in ONIX (black). a) Extraction aperture geometry of the BATMAN test facility. b) Extraction aperture geometry of the ELISE test facility. Space used to represent the plasma source (slashed red).

The complex 3D magnetic field configuration found at the test facilities is calculated externally and given to ONIX as input. For the aperture domain of the BATMAN test facility, the magnetic filter field and deflection field are taken from [73], calculated using the PerMag code [74]. For the ELISE test facility, the deflection field was taken from [73], calculated using the PerMag code [74], and the magnetic filter field was taken from [75], calculated using the commercial software ANSYS. The filter field direction is in the y direction in the coordinate system used in the simulations, corresponding to the horizontal direction in the test facilities. The deflection field main component is in the z direction, corresponding to the vertical direction in the test facilities. Figures for 2D maps of the magnetic field components can be found in Appendix B.

The test domain, shown in figure 4.5, was used for the validation of the model against basic plasma physics such as the plasma sheath and the surface emission of negative ions. It consists of two parallel absorbing plates with periodic boundary conditions in the directions parallel to the plates. Thus, this domain represents an infinite plasma confined by two infinite parallel plates.

The simulation domains are discretized by using a 3D Cartesian mesh with mesh size $\Delta\mathbf{x} = (\Delta x, \Delta y, \Delta z)$. The mesh size is kept constant through the simulation cycles.

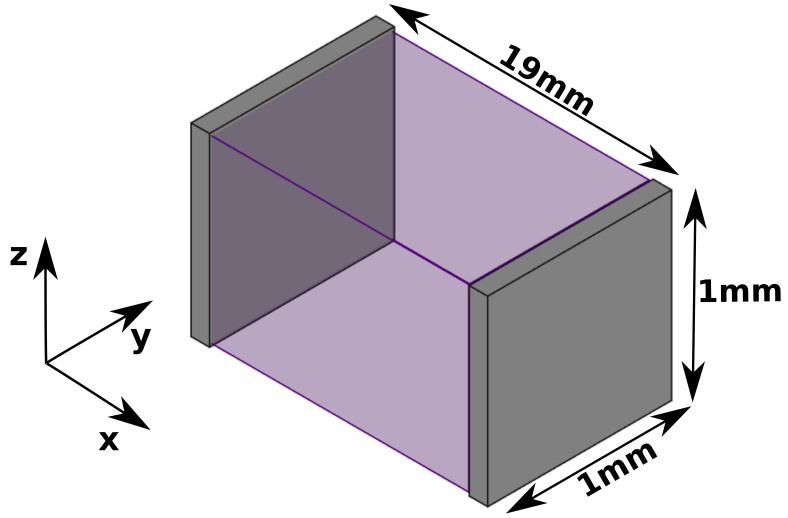

Figure 4.5: 3D domain used in ONIX for the physical validation of the plasma sheath and surface emission.

4.4.2 Poisson's equation solver

Poisson's equation is discretized by the finite difference method [48] onto the mesh extending over the simulation domain. This discretization of the Poisson's equation generates a sparse definite positive (SPD) linear system. An accurate and fast method to solve this kind of system is by the iterative method of the conjugate gradient (CG). As the shape of the linear system to be solved is known, a preconditioned version of the CG method is used in ONIX for a faster convergence to the solution [69].

The electric field is calculated from the discretized solution of the electrostatic potential over a mesh shifted by $\left(\frac{\Delta x}{2}, \frac{\Delta y}{2}, \frac{\Delta z}{2}\right)$. The differentiation is done by the middle point method for each of the spatial directions [69].

4.4.3 Particle configuration shape

ONIX uses as particle shape that of a spline of first order extended to the 4 closest nodes in each spatial direction. This particle shape reduces the statistical noise without a huge increase in the calculation time. Figure 4.6 shows the shape function of the quasi-particles in ONIX in a one dimensional direction. A particle p with center at the position $\mathbf{x}_\mathrm{p}$ is projected onto the 3D mesh, the particle shape reaches to the 64 nodes closest to the particle position.

The same shape function is used to interpolate the electric field from the mesh to the particle position by solving the equation (4.8).

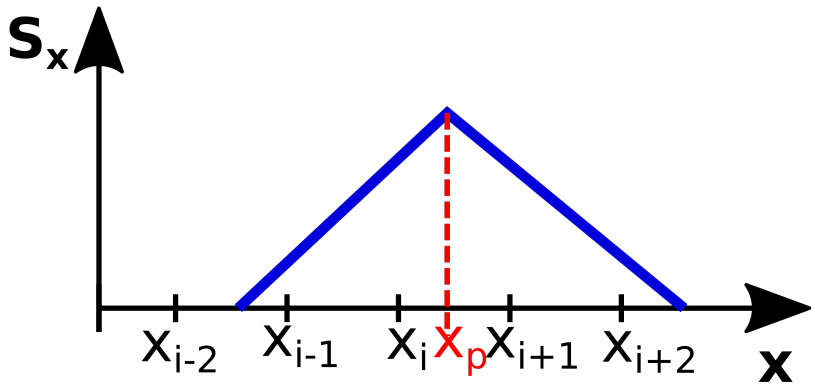

Figure 4.6: Shape function used for the spatial distribution of the quasi-particles in ONIX. The distribution is symmetric centered at $\mathbf{x}_\mathrm{p}$.

4.4.4 Particle Pusher

The part of the PIC code which solves the equations of motion, i.e. equation 4.6 and 4.7, is often refered as "particle pusher". ONIX implements the explicit Boris leap-frog finite differential algorithm [48] as particle pusher. In this scheme, at each time iteration, the position is known at the current time step t_n while the velocity is known at $t_\mathrm{n} - \frac{\Delta t}{2}$:

$$\mathbf{x}_{\mathrm{n}+1} - \mathbf{x}_\mathrm{n} = \mathbf{v}_{\mathrm{n}+\frac{1}{2}} \Delta t, \tag{4.14}$$

$$\mathbf{v}_{\mathrm{n}+\frac{1}{2}} - \mathbf{v}_{\mathrm{n}-\frac{1}{2}} = \frac{q}{m}(\mathbf{E} + \frac{\mathbf{v}_{\mathrm{n}+\frac{1}{2}} + \mathbf{v}_{\mathrm{n}-\frac{1}{2}}}{2} \times \mathbf{B})\Delta t. \tag{4.15}$$

It separates the velocity movement into a pure acceleration term related to the electric field and a pure rotation term related to the magnetic field by the introduction of two intermediate velocities $\mathbf{v}^-$ and $\mathbf{v}^+$:

$$\mathbf{v}^- = \mathbf{v}_{\mathrm{n}-\frac{1}{2}} + \frac{q}{m}\mathbf{E}\frac{\Delta t}{2}, \tag{4.16}$$

$$\mathbf{v}^+ = \mathbf{v}_{\mathrm{n}+\frac{1}{2}} - \frac{q}{m}\mathbf{E}\frac{\Delta t}{2}, \tag{4.17}$$

$$\frac{\mathbf{v}^+ - \mathbf{v}^-}{\Delta t} = \frac{q}{2m}(\mathbf{v}^+ + \mathbf{v}^-) \times \mathbf{B}. \tag{4.18}$$

4.4.5 Collision Processes

In table 4.1 the collision processes included in ONIX are summarized. The processes evaluated in ONIX are related to the creation and destruction of negative ions in a NBI ion source plasma: mutual neutralization (MN), associative detachment (AD), non-associative detachment (NAD), charge exchange (CX), electron detachment (ED) and electron dissociative attachment (DA). Besides, elastic collision for the momentum exchange of electrons with H atoms (eEC) are included.

Reactions	**Process**	**Reference**
Mutual neutralization (MN)	$H^- + H^+ \longrightarrow 2H$	[76]
Associative detachment (AD)	$H^- + H \longrightarrow H_2 + e^-$	[76]
Non-associative detachment (NAD)	$H^- + H \longrightarrow 2H + e^-$	[76]
Charge exchange (CX)	$H^- + H \longrightarrow H + H^-$	[76]
Electron dissociative attachment (DA)	$e^- + H_2(\nu) \longrightarrow H + H^-$	[77]
Electron detachment (ED)	$e^- + H^- \longrightarrow H + 2e^-$	[76]
Electron elastic collision (eEC)	$e^- + H \longrightarrow e^- + H$	[76]

Table 4.1: Collision processes included in the ONIX simulation code.

These collision types are implemented in ONIX by the use of the direct Monte-Carlo method. The cross sections σ_l shown in figure 4.7 are taken from [76][77] to calculate the probability for each process using equation (4.9). The target density n_{target}, for collisions with H or H_2, is taken from measurements from the test facilities ($n_{\mathrm{H}} = 10^{19} m^{-3}$, $n_{\mathrm{H_2}} = 4 \cdot 10^{19} m^{-3}$) [78]. These values are considered homogeneous and constant through the simulation domain. For the mutual neutralization process, n_{target} (for H^+) is taken from the mesh cell value in which the colliding particle is found.

Coulomb collisions between ions do not satisfy the conditions required to apply the direct Monte-Carlo method, and therefore they have been implemented using the binary collision method Takizuka-Abe [50]. Application of this method to all charged species would increase significantly the calculation time. The method requires to do particle pairing for each mesh cell which is computationally expensive. Therefore, in the code it is applied only to pairs formed by negative ions created at the PG surface and positive atomic ions. These particles are chosen as to study the redirection of the surface emitted negative ions.

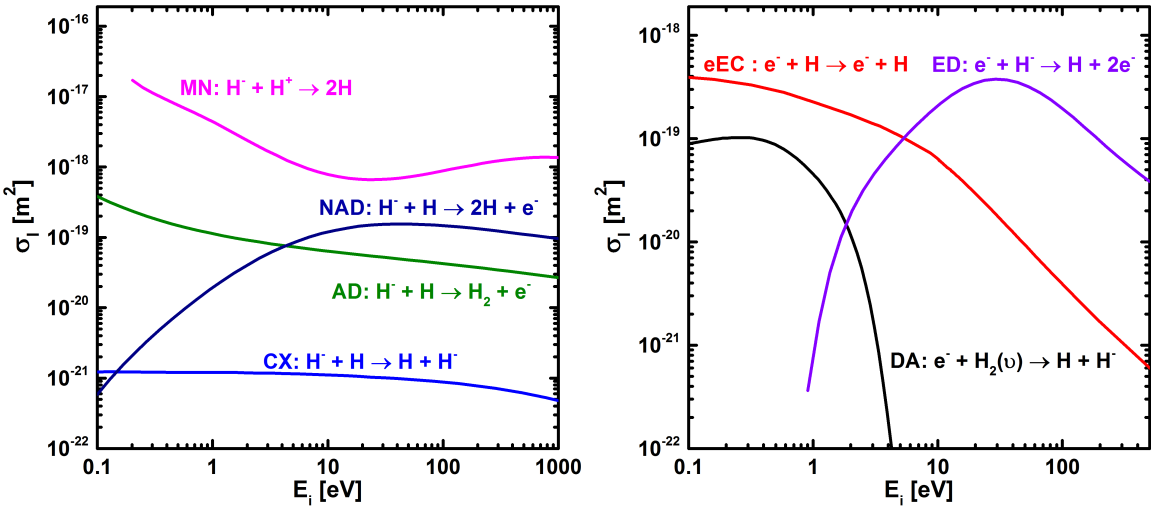

Figure 4.7: Left) Cross sections for a center of mass energy E_i: Mutual neutralization (MN), Non-associative detachment (NAD), Associative detachment (AD) and charge exchange (CX). Right) Cross sections for a incident e^- ion with energy E_i: Electron detachment (ED), Electron dissociative attachment (DA) and electron elastic collision (eEC) [76][79][77].

4.4.6 Surface particle emission

ONIX allows to simulate two different cases of surface emission of negatively charged particles: electron secondary emission by electron impact and negative ion emission by surface conversion of impinging atoms (most of the negative ions are produced by surface conversion of atoms [80][81]).

In the electron secondary emission each electron that hits a surface can emit an electron with a probability γ (between 0 and 0.8 [44]). Every time the impact of an electron onto a surface is registered, a random number R_2 is generated and if the condition $R_2 < \gamma$ is satisfied a secondary electron is emitted. A cosine distribution is used for the velocity vectors and a Maxwellian distribution for the energy.

The emission of negative ions is treated as a constant and homogeneous flux of negative ions Γ_{NI}. The emission rate of negative ions is the result of multiplying the influx of hydrogen atoms with the energy conversion probability [78][82]. The calculated emission rate for the negative ions is used as input in the ONIX code. A cosine distribution is used for the velocity direction distribution [37] and a Maxwellian distribution for the energy.

4.4.7 Initial conditions

At the beginning of each simulation the particles are homogeneously loaded in the source region, see figure 4.4. The initial velocity distribution is assumed to be Maxwellian in all directions. The probability for the velocity $\mathrm{v_i}$. in the direction i = x, y, z, is given by:

$$p(\mathrm{v_i}) = \frac{1}{\sqrt{2\pi}v_{\mathrm{th}}}\exp(\frac{-\mathrm{v_i}^2}{2v_{\mathrm{th}}^2}), \tag{4.19}$$

where $v_{\mathrm{th}} = \sqrt{\frac{k_{\mathrm{B}}T_{\mathrm{s}}}{m_{\mathrm{s}}}}$ is the thermal velocity, T_{s} is the temperature of the particles of species s and m_{s} is the mass of particles of species s.

4.4.8 Boundary conditions

In the test domain, as shown in figure 4.5, Dirichlet boundary conditions are used for the parallel plates, setting both of them at 0 V. In the extraction domain, see figure 4.3, the left part of the domain and the PG are set to 0 V using Dirichlet boundary conditions, while the EG is set to a extraction potential V_{ex}, typically in the range between 5-10 kV. The potential over the EG plane can be constant using the plate approximation (without aperture); or the potential map over this plane can be taken from another simulation tool (e.g. IBSimu [98]), in which case the the effect of the aperture on the potential is included. In the directions y and z, periodic boundary conditions are used for the potential.

For the particles, periodic boundary conditions are used in the directions y and z. If a particle hits any object, i.e. the parallel plates, PG or EG, ONIX has implemented three possible schemes to treat this particle and re-populate the source region: single particle re-injection[71], pair re-injection [83][61] and constant flux [44]. The working basis of the three schemes are detailed in figure 4.8 for a positive ion-electron plasma:

Single particle re-injection

- If a charged particle hits an object, a particle of the same specie is re-injected in the source region.

Pair re-injection

- If an electron hits an object, it is removed.
- If a positive ion hits an object, it is removed and a pair ion-electron is injected in the source region.

Constant flux

- If any particle hits an object, it is removed.
- Pairs of electrons and positive ions are injected, with a constant flux rate $\Gamma = \frac{n_i}{4} v_{th,i}$, into the source region each time step in order to keep a constant density in this region.

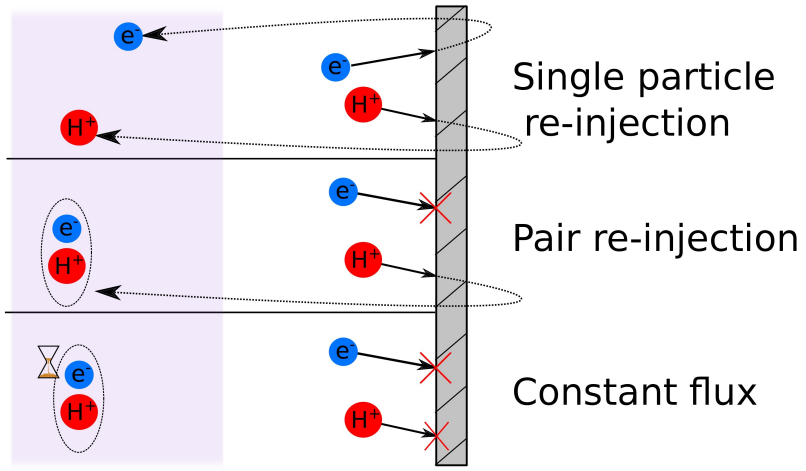

Figure 4.8: Different injection/re-injection schemes for particle re-population in the source region (for the case of a positive ion-electron plasma).

The particle re-injection/injection is done with a spatially homogeneous distribution over the source region. The velocity of the particle injected/re-injected in the source region follows a Maxwellian distribution. In order to avoid a reduction of the temperature (defined by the velocity distribution) due to the constant injection/re-injection of particles, it is needed to introduce either some kind of artificial heating or to modify the distribution function for injecting/re-injecting the particles, as suggested in [84]. An artificial heating is used in ONIX by resetting the velocity distribution of the particles with a sufficiently high frequency ($2{\cdot}10^9$ s^{-1}, higher than the electron-electron and electron-ion momentum exchange collisions) [61]. This is implemented using the guidelines described by Boeuf et al [61].

Each particle injection/re-injection scheme can be used in test and one aperture domain, depending of the physical scenario that is desired to be represented in the simulation. The scenario found in negative ion sources is of a thermal plasma facing an absorbing wall. The performance of the particle injection/re-injection schemes on

reproducing this behavior is evaluated in the test domain and the results are shown in chapter 5.

Chapter 5

ONIX code validation

The development process of a computational model, shown in figure 5.1, can be divided in three stages: model qualification, verification and validation. The model qualification consists on the analysis of the real system (Reality) in order to find a conceptual model. Examples of usual conceptual models are physical laws or system of equations. The conceptual model is then converted into a computerized model by its numerical discretization and the programming of it into a computer application. The verification ensures that the computerized model has implemented the numerical solvers properly, and therefore the equations represented in the computerized model are the same as those in the conceptual one. This step is formally defined as "ensuring that the computer program of the computerized model and its implementation are correct" [85]. The model validation consists on evaluating the results of the model and ensuring that it represents the studied system. This stage is defined as "substantiation that a computerized model within its domain of applicability possesses a satisfactory range of accuracy consistent with the intended application of the model" [85]. If all the mentioned stages of the development process have been successfully achieved, then the computerized model can be used to facilitate, speed up or give deeper understanding of the real system. The validated computerized model can also be used as predictive tool for scenarios in the range in which it was validated.

The system composed by Vlasov's and Poisson's equations are a well established conceptual model for the plasma dynamics (for plasmas densities and temperatures as those found in the extraction region of a NBI negative ion source). The PIC method allows to create a computerized model of this system of equations. An electrostatic 3D PIC model with a Monte-Carlo collision module has been implemented and verified in the ONIX code by Mochalskyy [69]. The validation of the ONIX code for simulating the plasma in the extraction region of negative ion sources is detailed and explained in this chapter.

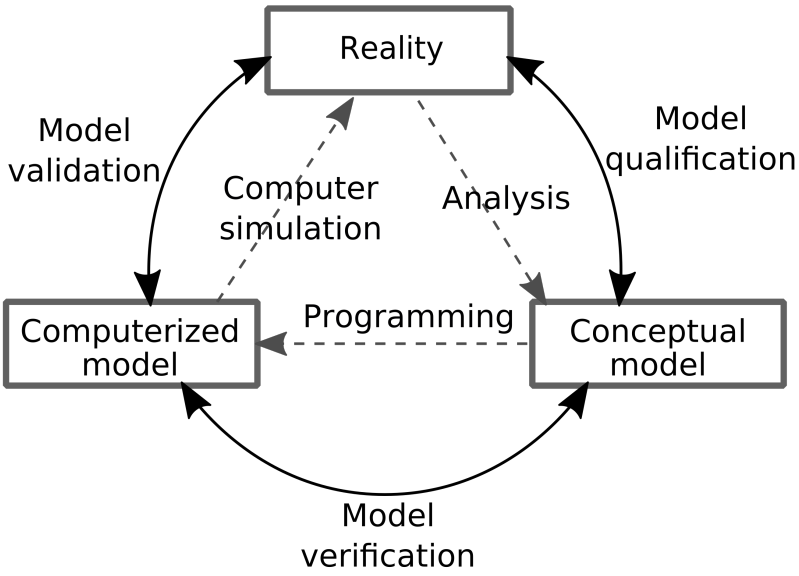

Figure 5.1: Scheme of the process of verification and validation of simulation models [85].

5.1 Physical validation

The ONIX validation was done for the basic plasma physics phenomena taking place in the plasma-wall interface: the plasma sheath and the surface particle emission, for the extraction region of the negative ion source for fusion. The validation of the description of these phenomena was done by the comparison technique [86] using the ONIX test domain (figure 4.5) : 1) A simple comparison scenario was chosen, 2) The output generated by ONIX in this scenario was compared to the results that can be described by analytical models, and 3) ONIX results were compared to results obtained by other validated computerized models.

5.1.1 Plasma sheath

The three particle injection/re-injection schemes implemented in ONIX were tested for the reproducibility of the collision-less plasma sheath scenario. It was chosen as it represents the most simple scenario of the interface in between a thermal plasma and an absorbing surface. For the validation, the ONIX results were compared with a 1D analytical fluid model [43], a 1D kinetic model [87] and results of a 1D PIC computational model [44].

The models in [43][44][87] represent a one dimensional thermal plasma source in front of an absorbing wall. This one dimensional domain is representative of an infinite

plasma in front of an infinite absorbing plate. The ONIX test domain represents the same spatial scenario. The physical parameters consisted of a plasma composed of electrons e^- and positive hydrogen ions H^+ with a density $n_{\text{plasma}} = 10^{16}$ m^{-3}, electron temperature $T_e = 1$ eV and ion temperature $T_{H^+} = 1$ eV. These values are close to those measured in the extraction region of NBI negative ion sources, with the density being one order of magnitude lower to reduce the calculation time (by a factor ∼30). Collisions were omitted to represent the same situation as in the analytical models. The numerical parameters for these simulation consisted of a mesh size $\Delta\mathbf{x} = (0.5\lambda_D, 0.5\lambda_D, 0.5\lambda_D)$ with $\lambda_D = 7.4 \cdot 10^{-5}$ m, $\Delta t = 0.05\omega_{pe}^{-1}$ with $\omega_{pe}^{-1} = 1.7 \cdot 10^{-10}$ s and an average of 80 particles per cell; these numerical parameter extensively satisfy the PIC stability requirements [48].

The evaluation of the plasma sheath formation was intended to test if these schemes reproduce this equilibrium state. Figure 5.2 shows the resulting plasma sheath for the three different investigated injection schemes, i.e. pair re-injection, single particle re-injection and constant flux injection.

The constant flux injection and pair re-injection schemes achieved a steady state and formed the characteristic potential drop of the plasma sheath. The constant flux injection scheme reaches a steady state when the total number of particles in the simulation is constant over time, implying that the number of particles being injected per time step in the system and those being lost at the walls were identical. This equilibrium condition in the numerical model is the direct equivalent of the one produced in a real plasma by the plasma sheath. In the equilibrium state, this scheme produced a plasma potential drop of 2.45 V which is, within a 4% discrepancy, in agreement with the value 2.54 V given by the analytical model in [43].

The pair re-injection scheme achieved a steady state when the total number of electrons was constant over time. In this scheme the number of ions is kept constant during the simulation, but the number of electrons adjust according to the plasma dynamics. A constant number of electrons in the system means that the number of electron-ion pairs being re-injected is equal to the number of electrons being lost at the absorbing walls. Thus, the number of ion-electron pairs injected in the source region is the same as those being lost at the walls. The value for the plasma potential is 2.52 V and it agrees, within a 1% difference, with the expected value predicted by the analytical model in [43].

The constant flux and pair re-injection schemes succeed in representing the plasma sheath steady state in which a potential drop is produced to equate the out-flux from a quasi-neutral plasma. By the injection of ion-electron pairs with neutral net electric

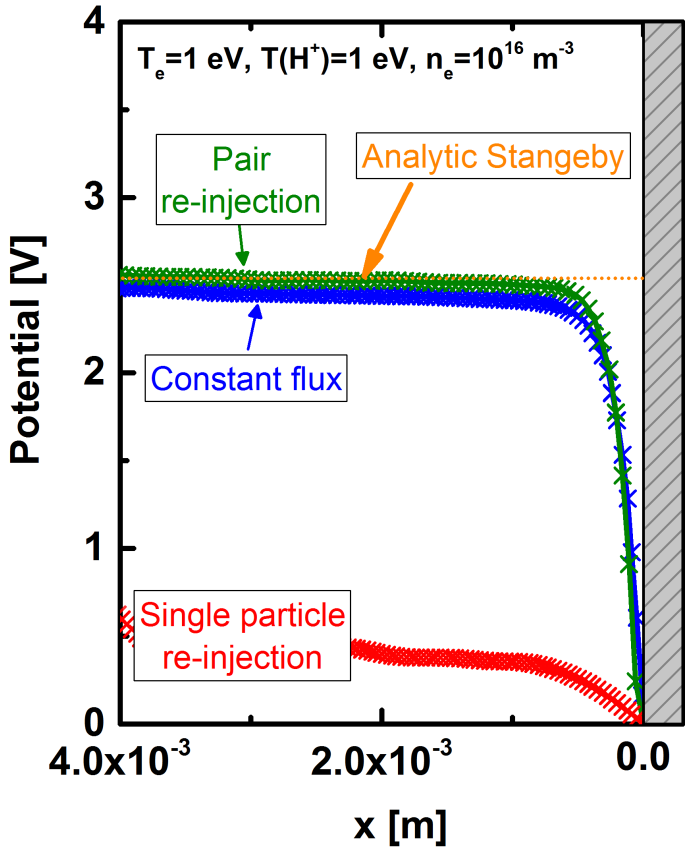

Figure 5.2: Electrostatic potential obtained for an positive ion-electron plasma in the test domain and the different injection/re-injection schemes in a simulation with T_e = 1 eV, T_{H^+}=1 eV, n_e= 10^{16} m^{-3}, λ_D = 7.4x10^{-5} m, Δx = 0.5 λ_D and Δt = 0.05 ω_{pe}^{-1} with $\omega_{pe}^{-1} = 1.7 \cdot 10^{-10}$ s.

charge, both schemes also avoid the artificial generation of plasma density oscillations [48] that could be created by the sudden deposition of isolated electric charges into the source region.

The single particle re-injection scheme did not reach a steady state despite the longer simulation time adopted with respect to the other two previous cases (1.8 μs instead of 0.9 μs). Since in this case it is not possible to identify the equilibrium of the system from a constant number of particles, instead the equilibrium is defined by the electrostatic potential stability in the plasma. The electrostatic potential oscillated around an average value of 0 V during the simulation time without producing any potential drop similar to that of the plasma sheath. An steady state equilibrium was not reached with this method. An explanation is found in the basics of the plasma sheath origin, in which a non-neutral region (the sheath) is formed to produce a potential drop. This state implies that the total charge of the system is not zero.

The initial conditions of the simulations is that of a quasi-neutral plasma with total net charge equal to zero. As the system keeps this initial state, when the single particle re-injection scheme is used, it is then impossible to generate two differently charged regions, one quasi-neutral and another positive charged. In addition, this scheme artificially generates plasma density oscillations by injecting isolated charges in a quasi-neutral plasma. Thus, this scheme is not suitable for studies related to the plasma dynamics.

5.1.2 Range of accuracy

The validation of ONIX has been done up to this point only for a fixed plasma density and electron temperature. The next step in the validation process is to test a range of accuracy.

Two tests were done: varying of the electron temperature and checking its influence on the plasma sheath potential drop for a fixed density, and the variation of the density and its effect on the sheath length for a fixed electron temperature. The pair re-injection scheme was chosen for this step in the validation as it allows setting the average plasma density by fixing the amount of positive ions in the system.

A higher electron temperature means a higher electron velocity, thus a higher electron out-flux from the plasma. Therefore, a higher plasma potential develops to reduce this out-flux of negative charges from the plasma and increase the out-flux of positive charges. The increase of the plasma sheath potential drop with the electron temperature is expected to be linear in the simplest model given by the equation 3.16 and non-linear to a small degree in the models of Stangeby [43] and Schwager [87].

Figure 5.3 shows the plasma sheath potential drop from ONIX for the variation of the electron temperature with a fixed plasma density. The plasma is composed by H^+ and e^- with a density of $n_{plasma} = 10^{16}$ m^{-3} in the test domain, an ion temperature $T_{H^+} = 1$ eV and the electron temperature is varied in the range between 0.5 eV and 5 eV. These results are compared against the analytical solutions of [43][87] and the 1D PIC code [44]. For low electron temperatures ($T_e < 3$ eV) the results are in agreement with the analytical solution and the 1D PIC model with a discrepancy $< 2\%$. For higher electron temperature the discrepancy increases up to around 10% for $T_e = 5$ eV.

Contrary to the changes in the electron temperature a change in the density does not change the value of the plasma potential. However, it changes the length of the plasma sheath Δx_{sheath}. An increase in the density increases in the same amount the

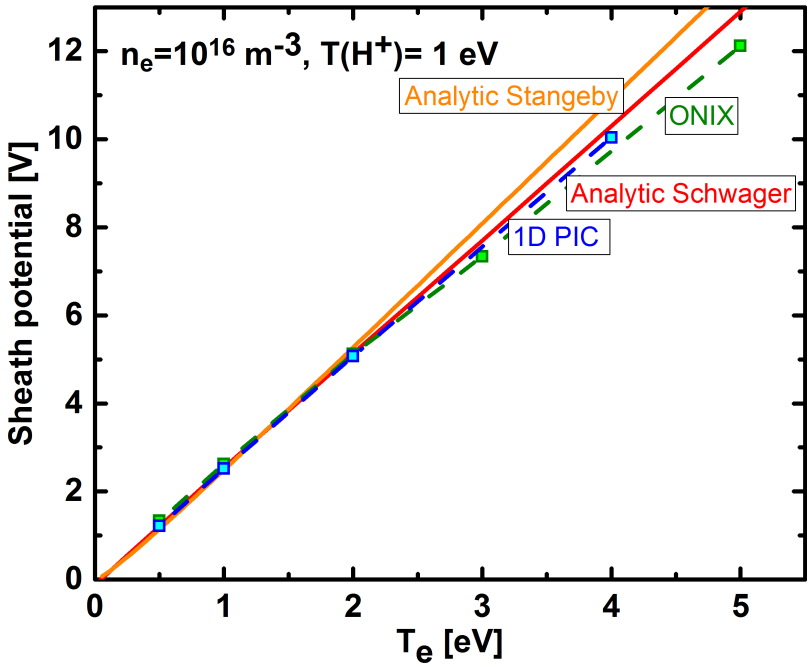

Figure 5.3: Plasma potential versus electron temperature for a positive ion-electron plasma. ONIX results for the test domain are compared with the analytical model of Stangeby [43], Schwager [87] and the 1D PIC code from [44]. Numerical parameters for the simulation are $\Delta x = 0.5\ \lambda_D$ and $\Delta t = 0.05\ \omega_{pe}^{-1}$ with $\omega_{pe}^{-1} = 1.7 \cdot 10^{-10}$ s.

out-flux of negative and positive charged particles from the quasi-neutral plasma, thus the plasma potential is not affected. Nevertheless, a higher density implies that the positive charge needed to generate the plasma potential drop is contained in a smaller region. Consequently, an increase in the plasma density implies a decrease in Δx_{sheath} (with $\Delta x_{sheath} \sim 6 - 8\lambda_D$). The plasma sheath length Δx_{sheath} can be defined as the extension of the region in which a positive charge imbalance takes place.

Simulations varying the plasma density in the range 10^{14} m^{-3} to 10^{17} m^{-3} were done in the test domain with a plasma composed solely of H^+ and e^- with $T_e = 1$ eV and $T_{H^+} = 1$ eV. Figure 5.4 shows the results for the dependence of Δx_{sheath} with the electron density. A very good agreement between ONIX and the other models can be seen in the trends and absolutes values.

5.1.3 Secondary particle emission

For the case of secondary electron emission Stangeby [43] and Schwager [87] derived analytical solutions for the dependence of plasma potential with the secondary electron emission coefficient γ. These models predict a reduction of the plasma potential with increasing γ. The flow of secondary electrons Γ_{SE} from the surface partially

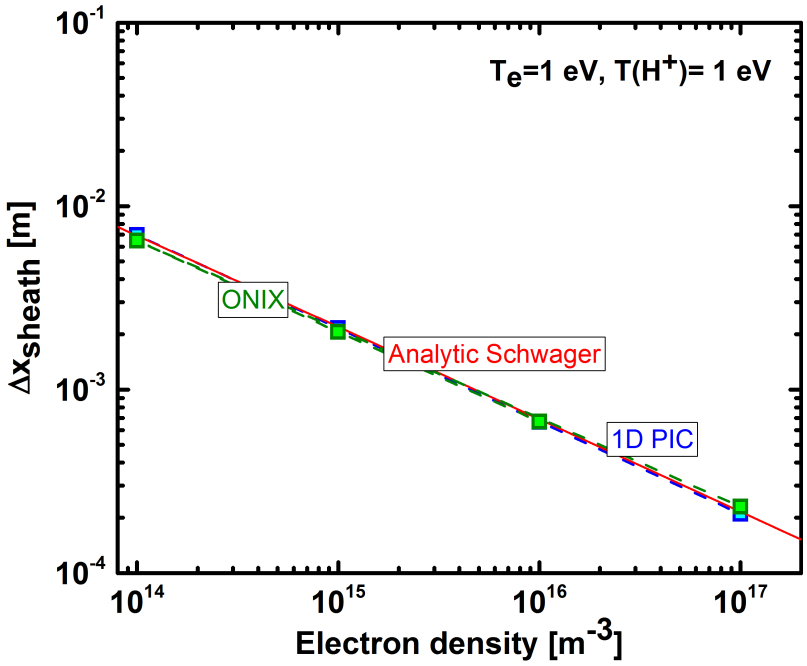

Figure 5.4: Sheath length versus the plasma density for a positive ion-electron plasma. ONIX results for the test domain are compared with the numerical solution of the Schwager analytical model [87] and the 1D PIC code from [44]. Numerical parameters for the simulation are $\Delta x = 0.5\ \lambda_D$ and $\Delta t = 0.05\ \omega_{pe}^{-1}$.

compensates the out-flow of electrons from the plasma Γ_e, see equation 3.17, thus reducing the plasma potential.

Two physical scenarios were tested to validate the accuracy of ONIX in describing emission of charged particles from a surface: secondary emission of electrons by electron impact and surface emission of negative ions by the conversion of impinging neutral atoms.

ONIX was tested for the secondary electron emission scenario. The secondary electron probability varies between 0 and 1 for materials such as Cu or Ni and $T_e < 5$ eV [88][89]. A variation of γ in the range between 0 (no emission) to 0.8 was done. The upper limit of this parameter variation is defined by the critical secondary electron emission coefficient $\gamma_{SEC} = 0.8$. The reason for this limit is that for $\gamma > \gamma_{SEC}$ the analytical models are not longer valid. Thus, the analytical models are not capable of describing the formation of the potential well.

The simulations were done in the test domain with a plasma composed of H^+ and e^- with $T_e = 2$ eV, $T_{H^+} = 2$ eV and $T_{SE} = 1$ eV, the physical parameter values are changed in order to match the conditions used by the 1D PIC code from [44].

Figure 5.5 shows the results given by ONIX for the dependence of the plasma

potential on γ. The simulations results are in good agreement with the analytical models by Stangeby [43] and Schwager [87] and the 1D PIC code from [44], presenting a maximum deviation of 8%.

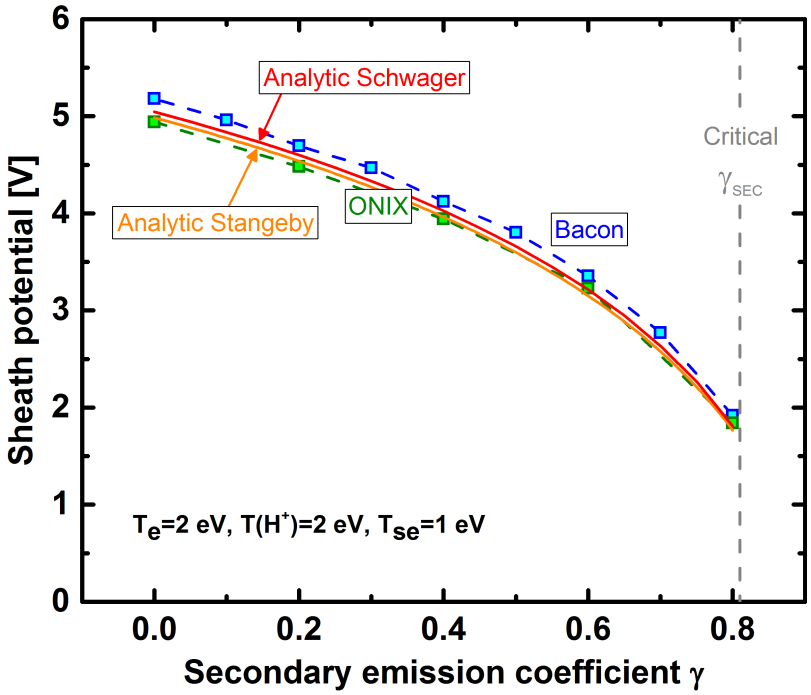

Figure 5.5: Plasma sheath potential versus the secondary electron emission coefficient γ. ONIX results for the test domain are compared against the analytical model of Stangeby [43], Schawger [87] and a 1D PIC code from [44]. Numerical parameters for the simulation are $\Delta x = 0.5\lambda_D$ and $\Delta t = 0.05\omega_{pe}^{-1}$.

The next step into the validation of ONIX is to investigate the effect of negative hydrogen ion emission from a surface into the plasma. The test domain was used with a plasma composed of H^+ and e^- with $T_e = 2$ eV, $T_{H^+} = 0.8$ eV, $T_{H^-} = 1$ eV and $n_{plasma} = 10^6$ m^{-3}, in order to match the conditions used by the 1D PIC code from [44]. The emission of negative ions is implemented as a constant flux of 55 Am^{-2} from the surface, the value is estimated from the results obtained from [44]. The emission rate of the negative ions is calculated under the assumption that negative ions are created by the surface conversion of atoms impinging onto the surface and that the flux of neutral atoms is constant and homogeneous.

Figure 5.6 shows the spatial profile of the positive ion density, the electron density and the negative ion density calculated by ONIX, the model by Schwager [87] and the 1D PIC code from [44]. Similar as for the case of secondary electron emission, the surface produced negative ions modify the structure of the plasma sheath, affecting

the transport of charged particles from and to the surface. The density profiles obtained with ONIX, Bacon and the analytical model by Schwager are on top of each other, proving the capacity of ONIX to reproduce the plasma scenario found in the extraction region of negative ion NBI sources.

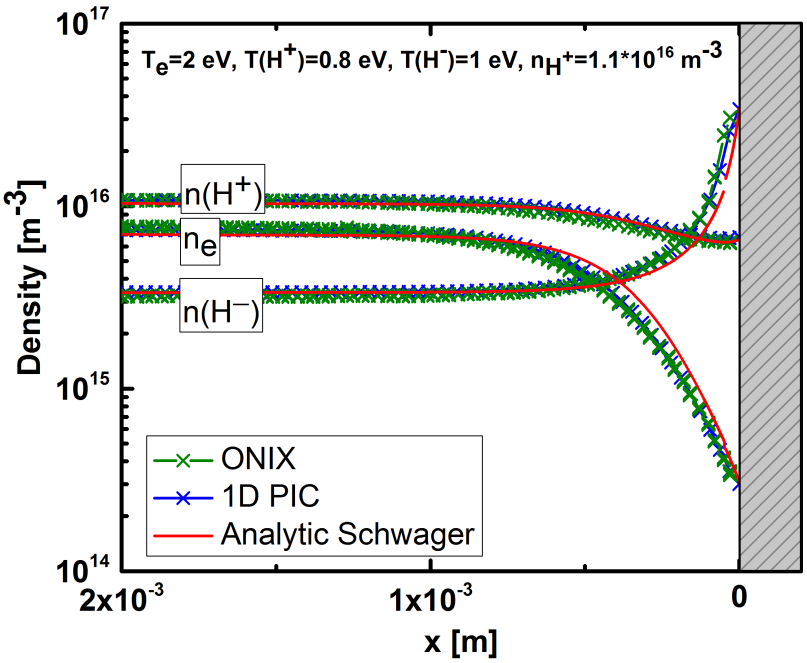

Figure 5.6: Density of species in the plasma with emission of negative ions from the wall as a function of the distance from the surface. ONIX results for the test domain are compared against the analytical model of Schwager [87] and the 1D PIC code from [44]. Numerical parameters for the simulations are $\Delta x = 0.5\ \lambda_D$ and $\Delta t = 0.05\ \omega_{pe}^{-1}$.

5.2 Numerical efficiency of the validated model

The calculation time needed by PIC codes increases with the total number of mesh points N_m, the total number of quasi-particles N_p and the total number of time iterations N_{time}. Due to the stability criteria introduced in chapter 4, these parameters increase with the density n_{plasma} of the system. The number of mesh points in each direction is $N_i = L_i/\Delta i$ with $i = x, y, z$ and L_i is the domain length in i direction. The mesh size Δi in each direction has to be of the order of λ_D to ensure numerical stability, so $N_i \sim n_{plasma}^{\frac{1}{2}}$ and $N_m \sim n_{plasma}^{\frac{3}{2}}$ in a 3D system. If we account for a fixed number of particles per cell to ensure the statistical noise in all the simulations, it is

found that N_{p} increases as N_{m} with the density. The number of time iterations will be $N_{\mathrm{time}} = t_{\mathrm{s}}/\Delta t$ where t_{s} is the time required for a steady state. The time step Δt is proportional to $\omega_{\mathrm{pe}} \sim \frac{1}{n_{\mathrm{e}}}$, and therefore for higher densities the time step is required to be smaller, resulting in an increased N_{time}.

A density of around 10^{17} m^{-3} is measured close to the PG at the negative ion source test facilities. This density is ten times higher than that used for the calculations used in the ONIX validation. Additionally, calculations for the NBI sources use the extraction aperture domain which is considerably larger than the test domain. Consequently the computational cost is increased by a factor ~ 700 respect to the calculation done in the test domain. ONIX is a well parallelized code and can run simulations for one extraction aperture, at a density equal to 10^{17} m^{-3}, using High Performance Computing (HPC) systems. A usual ONIX simulation until steady state requires at least 180 hrs of computation time in 4096 cores making it impossible to run on desktop machines.

However, the amount of computation time available at HPC systems is highly restricted, therefore a set of optimal numerical parameters for ONIX calculations is needed. With an optimal set of numerical parameters the calculation time can be reduced without altering the physical results.

The optimal set of numerical parameters was found by a variation of the mesh size, the time step and the number of particles per cell. An increase in the mesh size results in a lower amount of mesh points reducing in this way the calculation time needed by the Poisson solver and by the charge projection onto the mesh. An increase in the time step shortens the number of time iterations of the PIC cycle until the steady state is reached. A reduction of the number of particle per cell leads to a reduction of charge projection operations and the number of executions related to the particle pushing. To select the right set of parameters each one of them was tested separately. The test domain was used with a plasma formed by e^- and H^+, the temperatures set to $T_{\mathrm{e}} = 1$ eV and $T_{\mathrm{H^+}} = 1$ eV. The plasma density is set to $n_{\mathrm{plasma}} = 10^{16}$ m^{-3} to reduce the calculation time.

5.2.1 Mesh size optimization

The mesh $(\Delta x, \Delta y, \Delta z)$ was varied from $0.5\lambda_{\mathrm{D}}$ to $8\lambda_{\mathrm{D}}$. The time step was kept to $\Delta t = 0.05\ \omega_{\mathrm{pe}}^{-1}$ and the average number of PPC over the domain was kept ~ 80. Figure 5.7 shows ONIX results for the evaluation of the plasma sheath potential for the different mesh sizes. A mesh size of $8\lambda_{\mathrm{D}}$ produces a plasma sheath with noticeable

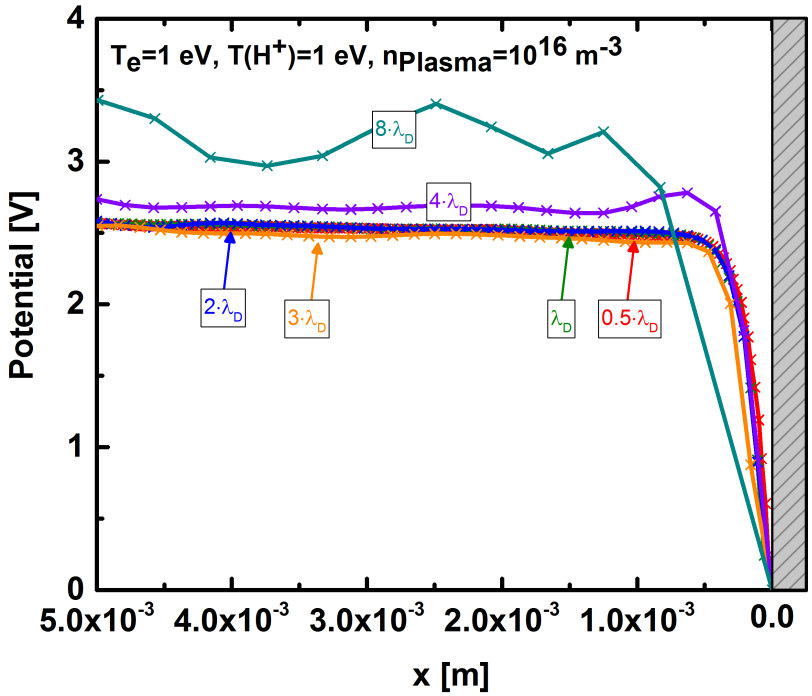

Figure 5.7: Simulation of the plasma sheath varying the mesh size using the test domain.

spatial oscillations. The plasma potential and the sheath width are larger than those produced by smaller mesh sizes, describing the sheath drop with just two mesh points. The result for a mesh size of $4\lambda_D$ shows still a higher value for the plasma potential and presents a different structure compared to calculations with smaller mesh sizes. Using a mesh size of $3\lambda_D$ does not perturb significantly the plasma potential in the quasi-neutral plasma region. However, the plasma sheath region lacks of enough mesh points and is numerically perturbed.

No considerable differences can be seen for the shape of the plasma sheath for cases with a mesh size of $\Delta x < 2\lambda_D$. Therefore, it is considered that a mesh size up to $2\lambda_D$ can be used to represent the plasma sheath physics without numerical perturbations.

5.2.2 Time step optimization

To determine the largest possible time step that does not affect the physical results given by ONIX, the mesh size was fixed to $0.5\lambda_D$ and the number of particles per cell kept above 80 in average. The plasma composition, density and temperatures are the same as in the previous investigation. Having fixed a value for Δx, the CFL criteria defines an upper limit for the time step to $\Delta t < \frac{\Delta x}{v_{\max}}$ with $v_{\max}$ fixed by the

thermal velocity of electrons $v_{\mathrm{th,e}}$; if we take $v_{\max} = \mathrm{A}v_{\mathrm{th,e}}$ and $\Delta x = \mathrm{B}\lambda_{\mathrm{D}}$ with A and B constants, then $\Delta t < \frac{B}{A}\omega_{\mathrm{pe}}^{-1}$. Taking $v_{\max} = 2v_{\mathrm{th,e}}$ (A = 2) 95 % of the particles in a Maxwellian distribution are considered, and for the particular case of Δx =0.5λ_{D} (B = 0.5), it is obtained that $\Delta t < 0.25\ \omega_{\mathrm{pe}}^{-1}$.

The plasma sheath structure was evaluated using three time steps: 0.05 $\omega_{\mathrm{pe}}^{-1}$, 0.1 $\omega_{\mathrm{pe}}^{-1}$ and 0.2 $\omega_{\mathrm{pe}}^{-1}$. Figure 5.8 shows no difference between the three evaluated cases of Δt. Therefore, a time step up to 0.2 $\omega_{\mathrm{pe}}^{-1}$ can be used as long as the CFL condition is respected.

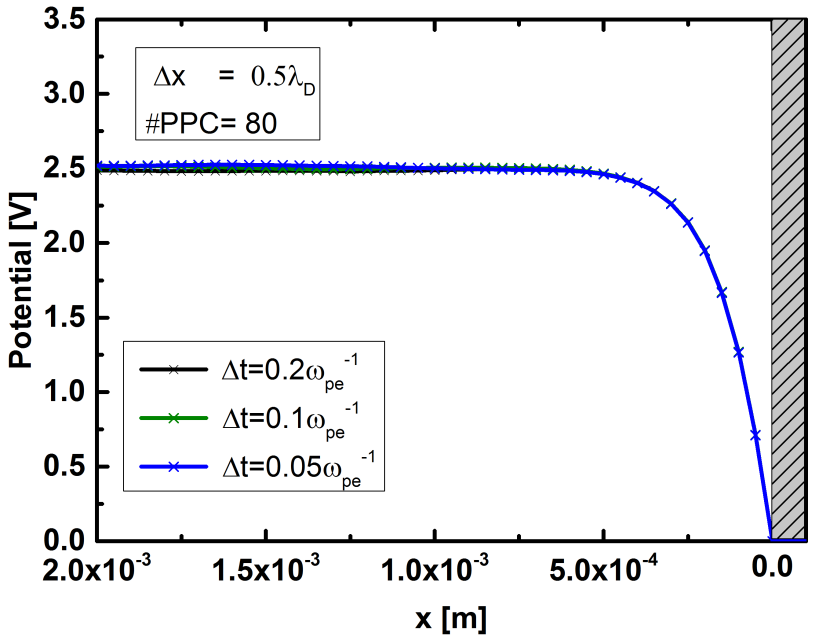

Figure 5.8: Simulation in the test domain of the plasma sheath for three different time steps, using a mesh size of 0.5λ_{D} and 80 particles per cell.

5.2.3 Particles Per Cell (PPC)

The optimal number of particles per cell for a compromise between accuracy and calculation time was found by a variation of it between 5 and 120. The mesh size was fixed to 0.5λ_{D} and the time step to 0.05$\omega_{\mathrm{pe}}^{-1}$. Figure 5.9 shows that only for values below 20 particles per cell statistical noise in the ions density (heavier species) can be seen. An optimal number of particles per cell can therefore be set between 20 and 30.

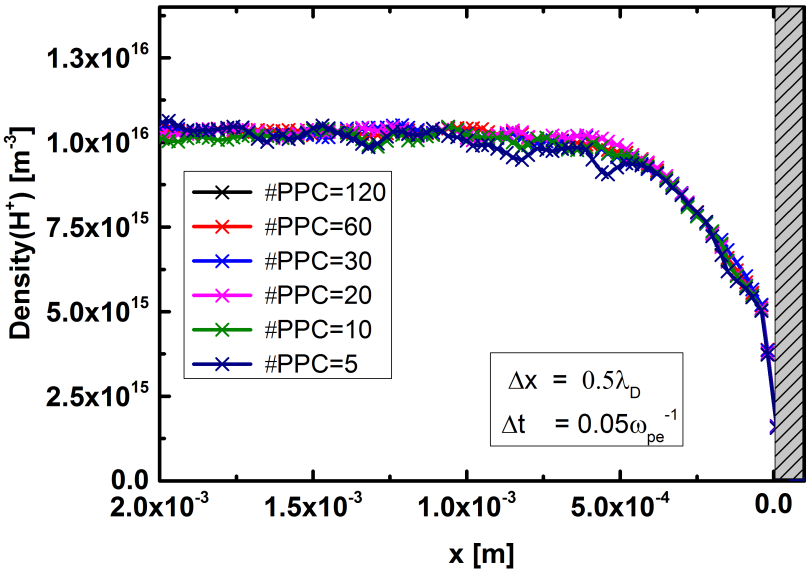

Figure 5.9: Comparison of the positive ion density by the variation of the number of particles per cell in ONIX using the test domain. Numerical parameters for the simulations are $\Delta x = 0.5\lambda_D$ and $\Delta t = 0.05\omega_{\mathrm{pe}}^{-1}$.

5.2.4 Optimal parameter set

From the parametric study of the numerical parameters upper boundaries for the mesh size and time step were identified, and a minimum value of the number of particles per cell was chosen. A set consisting of $\Delta x = 1.5\lambda_{\mathrm{D}}$, $\Delta t = 0.1\omega_{\mathrm{pe}}^{-1}$ and PPC = 30 is proposed as an optimal set. The validations test were repeated using this parameter set to verify that it reproduces properly the plasma sheath physics. The results from this set of parameters were compared to the non-optimized set, i.e. a set for which a longer calculation time is needed. Both parameter sets are described in table 5.1.

Numerical parameters	set 1	set 2
Δx	$1.5\lambda_{\mathrm{D}}$	$0.5\lambda_{\mathrm{D}}$
Δt	$0.1\omega_{\mathrm{pe}}^{-1}$	$0.05\omega_{\mathrm{pe}}^{-1}$
PPC	30	80

Table 5.1: Values for the parameter set 1 proposed to reduce the calculation time and the non-optimized parameter set 2 used in the ONIX validation.

The comparison between the two sets was done for calculations of the dependence of the sheath potential on T_{e} and the sheath length on the plasma density. The results for the sheath reproducibility along with its comparison to the results of the analytical model by Schwager [87] are shown in figures 5.10 and 5.11. No significant

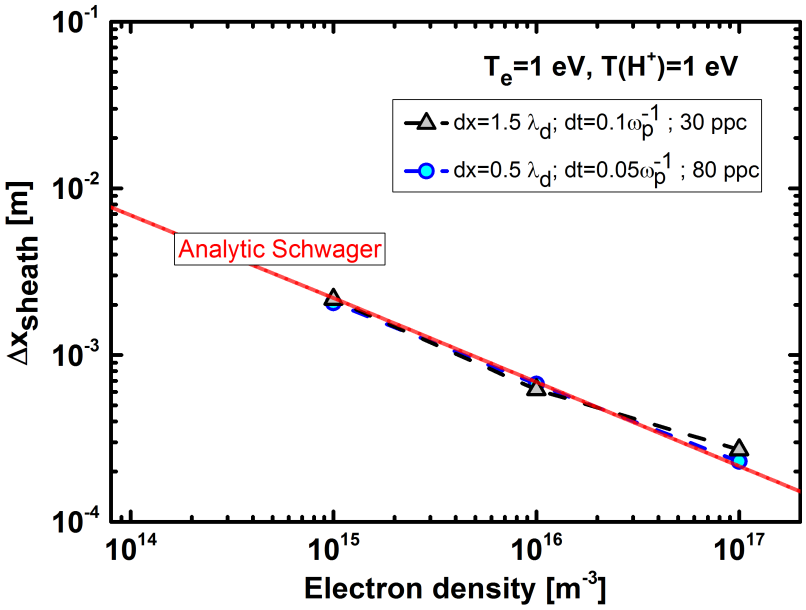

Figure 5.10: Sheath potential versus the electron temperature in simulations using parameter set 1 and parameter set 2 defined in table 5.1 and from the analytical model [87]. The simulation were done in the test domain.

discrepancy between the two numerical parameter sets and the analytical results can be seen.

Consequently, parameter set 1 was chosen for future applications using ONIX. A reduction of around 20% in the calculation time is obtained compared to the non-optimized set of numerical parameters.

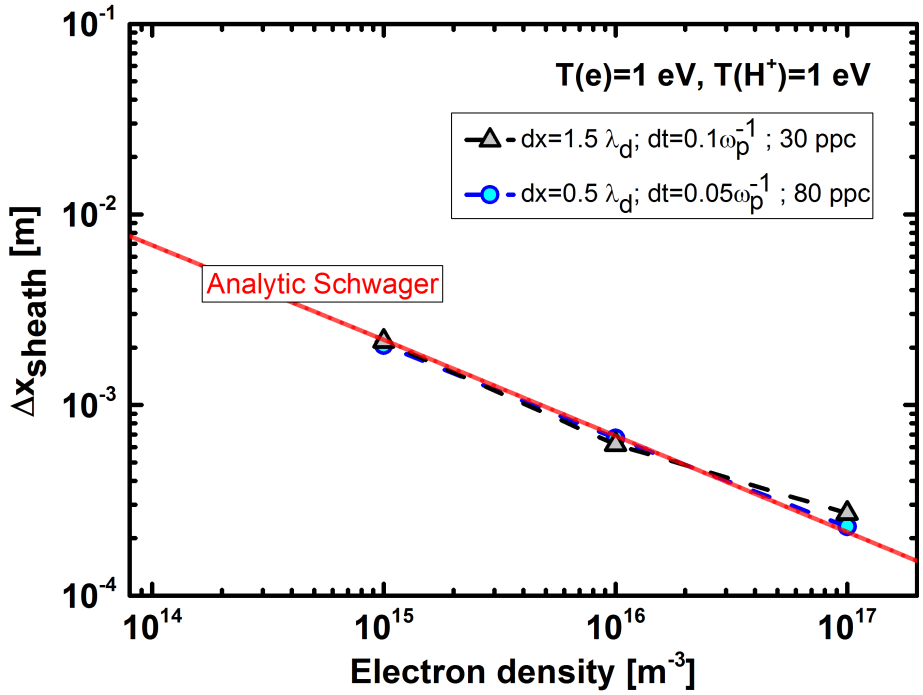

Figure 5.11: Sheath length versus the electron density in simulations using parameter st 1 and parameter set 2 defined in table 5.1 and from he analytical model (simulations done in the test domain).

Chapter 6

Simulations for the NBI ion sources at the test facilities

ONIX has been validated for the physics of the plasma sheath and surface emission in the extraction region. It can now be applied, using the one aperture domain, to improve the physical understanding of the transport of ions and magnetized electrons in the plasma before their extraction.

For all simulations using the one extraction aperture domain the same initial conditions for the plasma parameters were used, making the results comparable. The density and temperature of the species composing the plasma are taken from measurements at the BATMAN prototype ion source [78][90]. These values are summarized in table 6.1. For the distribution of positive hydrogen ions H^+, H_2^+ and H_3^+, a proportion of 2:2:1 is taken. The proportion used is an extrapolation of measurements of the particle distribution in a positive hydrogen ion source [91].

The simulations were done using the extraction aperture domains for the BATMAN and ELISE test facilities, shown in figure 4.4. The numerical parameters for all the simulations were $\Delta\mathbf{x} = (0.035, 0.035, 0.035)$ mm, $\Delta t = 5 \times 10^{-12}$ s and an average of 30 particles per cell. The total number of grid points in the BATMAN domain consisted of $N_\mathrm{x} = 784$, $N_\mathrm{y} = 400$ and $N_\mathrm{z} = 400$, while for the ELISE aperture geometry $N_\mathrm{x} = 864$, $N_\mathrm{y} = 576$ and $N_\mathrm{z} = 576$.

Surface production of negative ions was implemented assuming a constant and uniform flux of 550 Am^{-2} [44] from the surface. The emission rate is increased by one order of magnitude respect to that in the validation simulations because the plasma density has increased by the same factor. An initial amount of negative ions is inserted in the source region, as initial condition for H^-_{vol}, to match the values measured ($\sim 10^{17}$ m^{-3}) in the experiment at $\sim$2 cm from the PG. Negative ion density values of $\sim 10^{17}$ m^{-3} are only achievable with a surface production mode in negative

Specie	Density [m^{-3}]	Temperature [eV]
e	1×10^{17}	1
H^+	8×10^{16}	0.8
H_2^+	8×10^{16}	0.1
H_3^+	3×10^{16}	0.1
Cs^+	1×10^{16}	0.8
H^-_{vol}	1×10^{17}	0.8
$H^-_{surface}$	-	0.6
H	1×10^{19}	0.8
H_2	4×10^{19}	0.1

Table 6.1: Main initial physical parameters for simulations of one extraction aperture [78][90].

ion sources for fusion [26]; thus, these negative ions are originally emitted from the surface. However, to this day, none of the one aperture 3D PIC models can self-consistently achieve the negative ion density measured at ∼2 cm from the PG.

Additional electron losses may allow a higher amount of surface produced negative ions to go into the plasma from the surface. The one aperture model does not include losses of electrons onto the surface of the expansion chamber. The magnetized electrons follow the field lines of the magnetic filter field which are parallel to the PG, but at their end are perpendicular to the walls of the expansion chamber. These magnetized electrons impinging onto the wall of the expansion chamber are not represented in the reduced model of ONIX.

To keep the negative ion density in the source region constant, these initially set negative ions are treated with the single particle injection scheme. The collisions and chemical processes included in the simulations are those summarized in the table 4.1. The temporal evolution of the neutral atoms and molecules is not calculated by ONIX, and they are rather considered as a constant homogeneous background density over the simulation domain.

The complex 3D magnetic field configuration found at the test facilities is included in all simulations. For the aperture domain of the BATMAN test facility, the magnetic filter field and deflection field were calculated in [73] using the PerMag code [74]. For the ELISE test facility, the deflection field was calculated in [73] using the PerMag code [74] and the magnetic filter field was taken from [75], calculated using the commercial software ANSYS. The filter field is in the y direction in the coordinate system used in the simulations, being equivalent to the horizontal direction in the test facilities. The deflection field main component is in the z direction in the simulations,

corresponding to the vertical direction in the test facilities. Figures of the magnetic field components in different planes can be found in Appendix B.

6.1 BATMAN extraction aperture geometry

For each simulation a single parameter of the system was modified with respect to a standard case. These simulations were focused on the analysis of the effects, of these modifications, on the plasma in the extraction region (e.g. density distribution and plasma potential), the extracted negative ion current and the co-extracted electron current at the EG. The current at the EG is measured by counting and averaging the charge of the particles that reach the EG over 100 iterations (5×10^{-10}s).

6.1.1 BATMAN standard case

The simulation starts with a quasi-neutral plasma in the source region using the plasma parameters in table 6.1. In this case the EG is approximated as a plate, this approximation does not influence the electrostatic potential in the plasma region, an analysis of the effects of the inclusion of the aperture is given in Appendix A. The extraction potential is set to 10 kV over the EG plane, which is the highest possible value at the test facilities. The extraction potential is chosen in order to obtain the highest extracted current density according to the Child-Langmuir law, equation (3.19).

The simulation was continued until a steady state was found. The steady state was defined, for negative ion extraction simulations, by a constant extracted current measured at the EG position. A steady state current means that the flow of negative ions and electrons through the meniscus have reached an equilibrium (in this time scale); thus, so does the particle flows and the potential in the plasma.

Figure 6.1, shows the evolution of the extracted current density through the simulation time. The negative ion current density reaches a steady state at $j_{\mathrm{ex}} = 251$ Am^{-2} after 1.5 μs, and the co-extracted electron current density reaches a value around $j_{\mathrm{e}} = 115$ Am^{-2}. The extracted current density values and the electron-ion ratio $\frac{j_{\mathrm{e}}}{j_{\mathrm{ex}}} = 0.46$ are similar to the values found in a well-caesiated source [16].

The evolution of the co-extracted electron current density presents a peak at the beginning of the simulation. This initial high co-extracted electron current is caused by the electrons escaping from the quasi-neutral plasma, due to its higher thermal

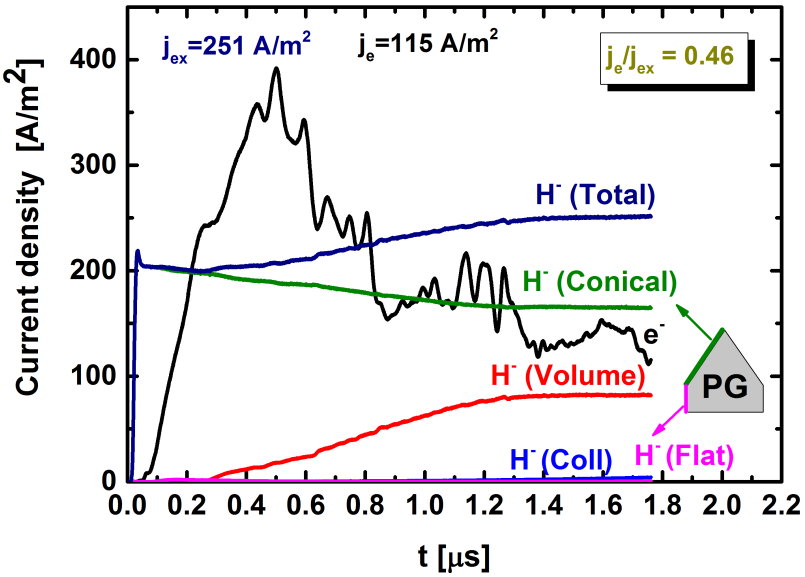

Figure 6.1: Extracted current measured at the EG position for the standard case. The negative ion current is divided according to their origin: from the PG (Conical and Flat part); originated by electron collisions with the neutral atoms (Coll); and initially inserted in the source region (Volume).

velocity, and then being accelerated by the extraction potential. The resulting initial charge imbalance produces an electric field that leads to the expansion of the plasma towards the PG. Once the plasma reaches the PG, an equilibrium is formed by the plasma sheath. Besides, the plasma expands through the aperture until an equilibrium between the forces on the plasma generated by the pressure gradient and the electric field is found, generating in this way the meniscus surface.

Figure 6.2 shows the meniscus and the positive ion density in the xy middle plane, after the plasma has fully expanded. The meniscus, which corresponds to the plasma-beam interface, is marked by the first isosurface of null positive ion density. The bottom part of figure 6.2, showing the electrostatic potential, remarks that the extraction potential is screened by the plasma, after the meniscus a strong electrostatic potential gradient arises. Figure 6.2 marks the profile line that will be used for showing potential and density potential profiles through the PG (border) and the aperture (beamlet axis).

Figure 6.3 shows the negative ion density in the xy middle plane, the negative ion density through the beamlet axis and the negative ion density profile at the EG. The decrease in the negative ions density after the meniscus is due to the conservation of the flux of particles, in order to preserve the flux of particles the density has to decrease as the velocity is increased by the accelerating electric field. An over-focused

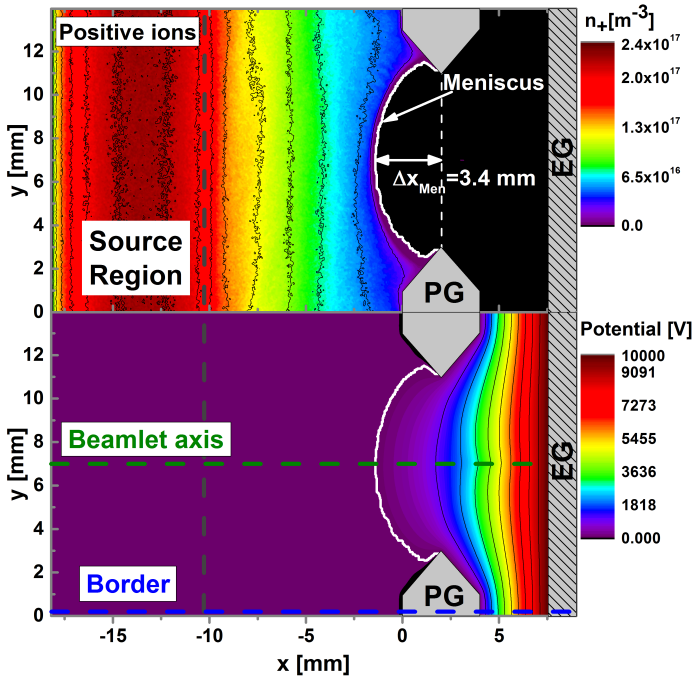

Figure 6.2: Top) Positive ion density map in the xy plane for the BATMAN PG aperture geometry, the meniscus is marked by the white curve. Bottom) Electrostatic potential.

beam is produced by the high curvature of the meniscus, the focus point being at 2.6 mm before the EG. The meniscus high curvature is due to the deep penetration of the extraction potential into the plasma. The meniscus penetrates around 3.4 mm into the plasma side from the middle of the PG aperture, having a high curvature in the zone close to the PG.

A beam halo is seen in the density profile at the EG. This halo is due to the surface produced negative ions originated at the conical part of the PG, while the rest of the negative ions produced a bell shaped beam at the EG. Figure 6.4 shows the negative ion density map in the xy middle plane according to where they were generated. The density map of negative ions originated at the conical part of the PG is the only one showing an over-focused beam. This is due to a fraction of surface emitted negative ions being directly extracted (located close to the PG edge), i.e. without passing through the plasma. The over-focused negative ions generate afterwards the beam halo seen at the entrance of the EG. The negative ions originating in the conical part of the PG represent 66 % of the total extracted current, thus it can be considered that the whole extracted beamlet is over-focused.

Figure 6.4 shows a low negative ion density in the plasma for those generated at the flat part of the PG. The transport of these ions into the plasma is limited

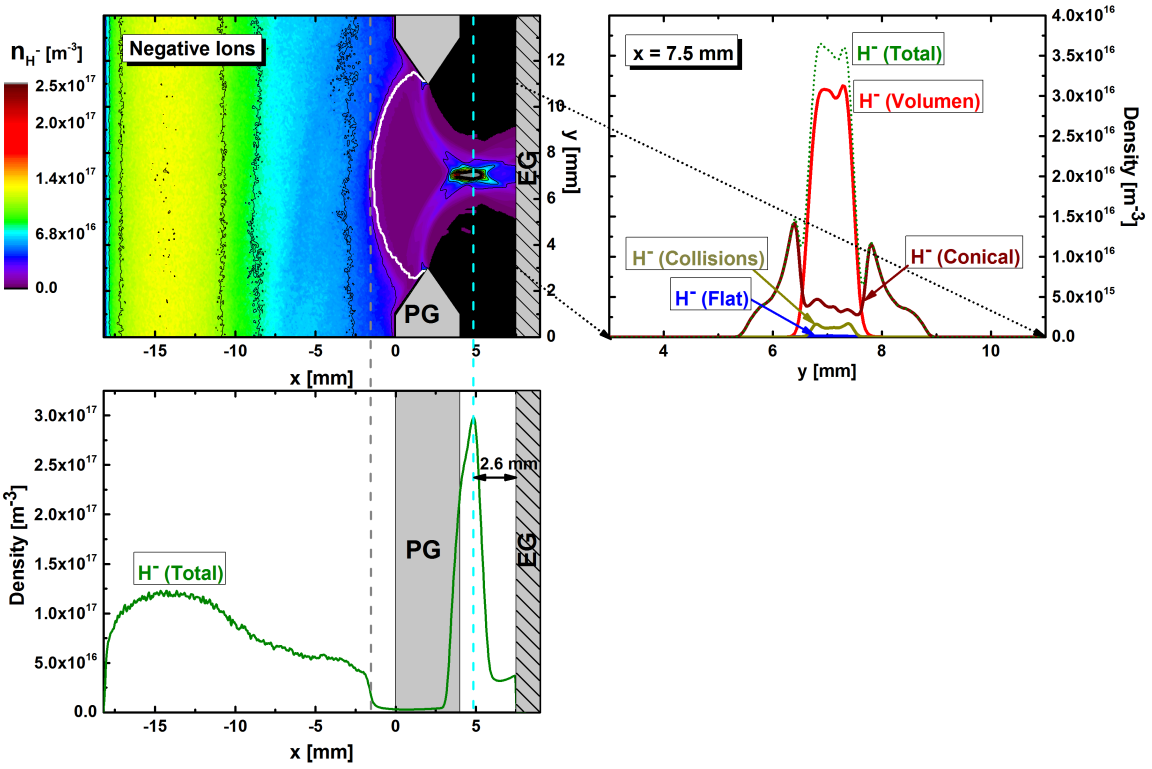

Figure 6.3: Top left) Negative ion density in the xy plane; Top right) Negative ion density profile at EG; Bottom) Negative ion density profile through the beamlet axis.

by the formation of the potential well in front of the PG, as shown in the border potential profile in figure 6.7. Besides, only a small fraction of these ions reaches the meniscus due to the low momentum transfer. A possible reaction increasing the momentum transfer and not included into this simulation are Coulomb collisions [92]. The extracted negative ions, originated in the flat region, produce a fraction of the beamlet with a focus point that is located, in the x direction, at the EG; the collective effect of the plasma reduce their initial preferential direction by the time they reach the meniscus.

Negative ions produced in the plasma volume, initially set or created by collisions, produce a focused fraction of the beamlet at the EG. These negative ions are generated with a isotropic velocity distribution, and the only preferential velocity direction is given by that of the plasma flow onto the surface and through the meniscus, i.e. in the beamlet axis direction. The density is higher in the source region and reduces as it diffuses onto the extraction aperture. Even though the neutral atom gas is considered constant and homogeneous over the domain, negative ions produced by collisions have a higher concentration in the source region. This is due to the higher amount of electrons in this region, which increase the production of negative ions by

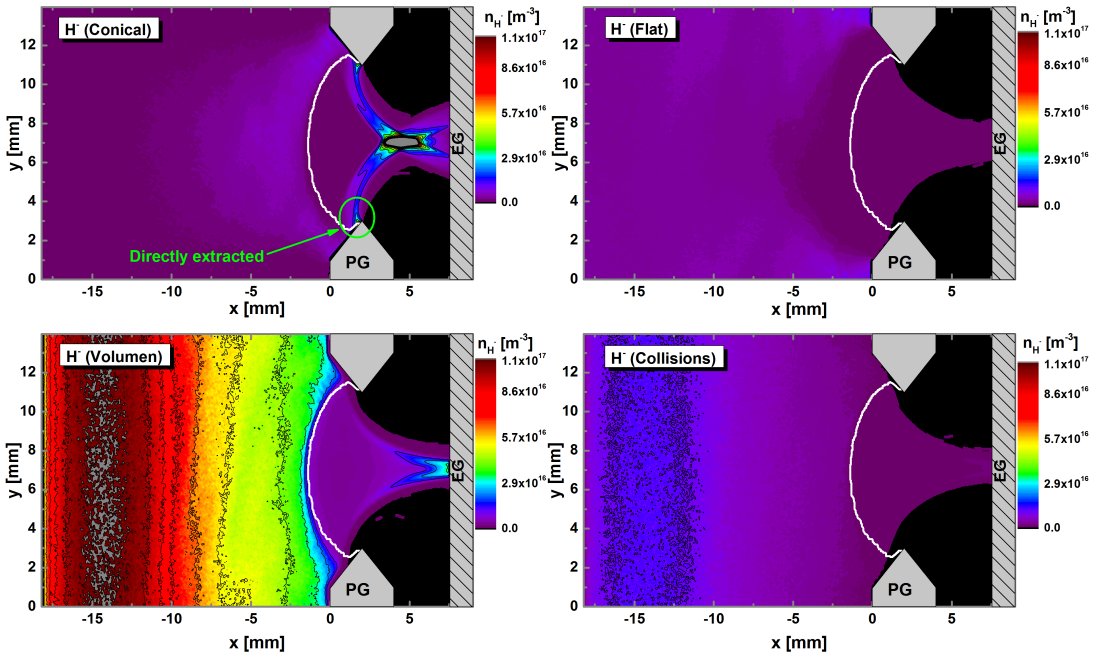

Figure 6.4: Negative ions density maps in the xy plane. The negative ions are divided according to their origin: Conical part of the PG, Flat part of the PG, initially inserted in the source region and created by collisions.

electron dissociative attachment.

The negative ion density distribution in the xz plane is similar to that shown in the xy plane. This is due to them not being magnetized.

Figure 6.5 shows the electron density maps in the xy and xz planes; the electron density decrease in the x direction towards the meniscus is caused by the magnetic field. The distribution of the electron density is, however, not the same in the xy plane compared to the xz plane. The reason is that the different magnetic fields are predominant in different directions: the filter field is predominant in the y direction and the deflection field is predominant in the perpendicular plane with its main components in the x and z direction. The filter field main component is parallel to the PG and limits the electron flow homogeneously over the y direction, this produces the decrease in the electron density in the xy plane. The deflection field limits the electron flow to the aperture, but close to the PG the x component is predominant and directs the electron flow onto the PG, resulting in a higher electron density close to the PG in the xz plane, compared to those in the xy plane.

The changes in the electron distribution caused by the filter field and the deflection field influence the distribution of the other charged species, as they re-arrange to keep the plasma quasi-neutrality. Figures 6.6 and 6.7 show the densities and potential

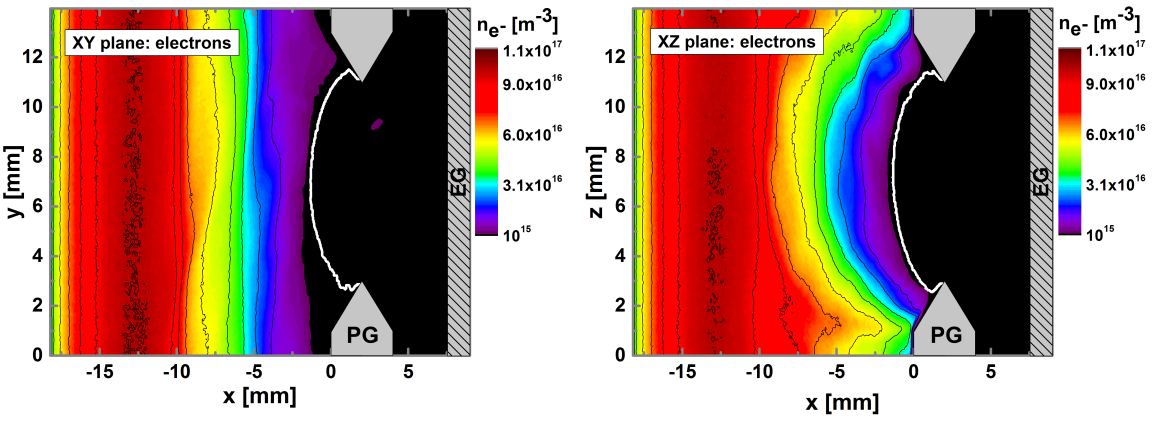

Figure 6.5: Standard case: Left) Electron density map in the xy plane (Filter field); Right) Electron density map in the xz plane (Deflection field). The meniscus is marked by the white curve.

profiles over the beamlet axis and border lines as marked in figure 6.2. The beamlet axis profile shows the effect of the magnetic field on the electron density: it decreases from $\sim 10^{17}$ m^{-3} at the exit of the source region to $<10^{15}$ m^{-3} close to the meniscus. However, a low electron density close to the meniscus boundary does not imply a low electron flux through the meniscus: the higher thermal velocity of electrons (due to its lower mass) leads to a flow of electrons through the meniscus which is still comparable to that of the negative ions. The density profile of the negative ions presents a smaller gradient compared to the electrons, due to the negative ions not being magnetized. In this way the negative ion density close to the meniscus is higher than that of electrons. The positive ions present a high density gradient between the source region and the PG; the positive ion density distribution rearranges to keep the plasma quasi-neutrality.

The border profile lines of the densities, shown in figure 6.7 for the xy and xz plane, show different electron distributions. The electron distribution in xy plane is reduced to values under 10^{14} m^{-3}, while the electron density distribution in the xz plane is not strongly reduced, presenting values higher than 10^{16} m^{-3}. The reduced electron density in front of the PG in the xy plane produces an ion-ion plasma, while in the xz plane similar densities of electrons and negative ions are found. An ion-ion plasma produces a different structure in the potential as now mass of the positive and negative charge carriers are similar. The plasma potential in front of the PG is different for both cases and in a lower degree so does the potential well. The potential well Φ_{well} is formed by the accumulation of surface emitted negative ions, and it limits the amount of negative ions going into the plasma. The average energy

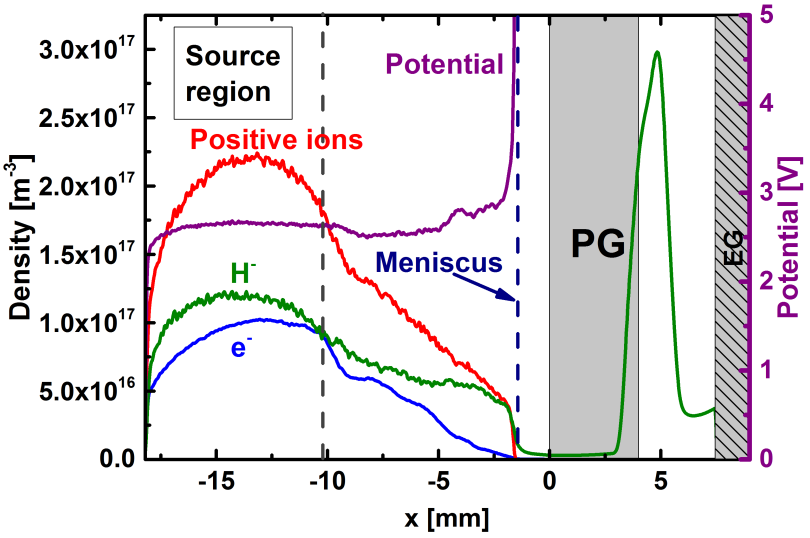

Figure 6.6: Standard case: Density and potential profiles along the beamlet axis line in the xy plane. The meniscus position is marked by the first null positive ion density isoline.

of the surface produced negative ions is 0.6 eV, meaning that more than the half of them are reflected back onto the PG. The deepness of the potential well is then a limiting factor in the increase of the maximum extracted current.

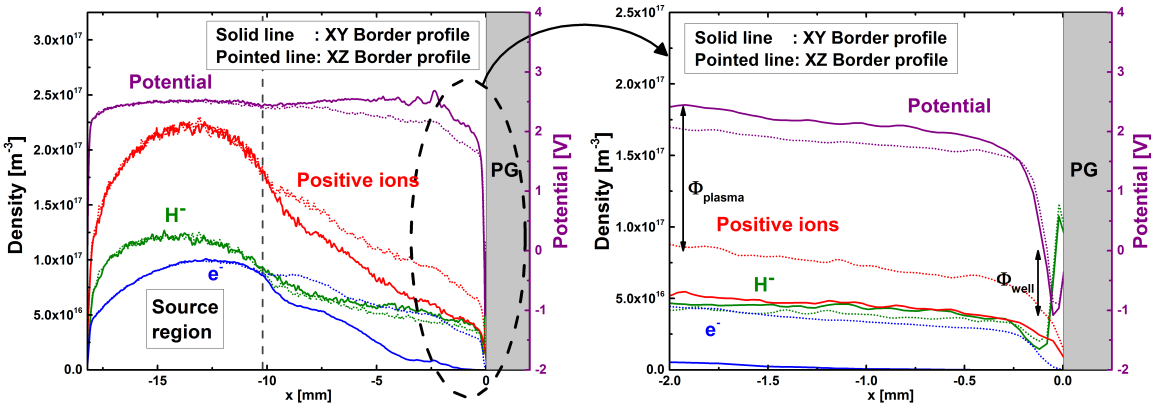

Figure 6.7: Density and potential profiles along the border line, as indicated in figure 6.2. The meniscus is marked by point of null positive ions density.

6.1.2 Extraction potential variation

In our initial standard simulation and over-focused beam was obtained. This resembles an under-perveance scenario. Thus, increasing the extracted current density or decreasing the extraction potential should lead the system closer to the perveance op-

timum. A higher extracted current density can be achieved by increasing the plasma density, however, this extends significantly the calculation time. Thus, the extraction potential was reduced from 10 kV to 5 kV.

In order to reduce the calculation time related to the expansion of the plasma from the source region until the PG, the simulation was started from the last equilibrium point of the standard case (at V_{ex} = 10 kV). The simulation was stopped once the extracted current at the EG reached the new steady state.

The extracted current density is reduced to j_{ex} = 140 Am^{-2} at V_{ex} = 5 kV compared to j_{ex} = 251 Am^{-2} at V_{ex} = 10 kV. The co-extracted electron current density is also reduced to j_e = 20 Am^{-2} from j_e = 115 Am^{-2}, and the electron-ion current density ratio to $\frac{j_{ex}}{j_e}$ = 0.14. The calculated perveance are $\Pi_{10kV} = 2.5{\cdot}10^{-4}$ $\frac{Am^{-2}}{V^{\frac{3}{2}}}$ and $\Pi_{5kV} = 3.9{\cdot}10^{-4}$ $\frac{Am^{-2}}{V^{\frac{3}{2}}}$, meaning that the system has been pushed to a higher perveance and a decrease in the beam divergence should be seen.

Figure 6.8 shows the negative ion density distributions for both cases with the meniscus shape over imposed in the xy middle plane. The flatter and less penetrating meniscus produces a more focused beam at the EG and reduces the amount of directly extracted negative ions. The changes in the meniscus shape and position and its relation with the extracted current density are described in the following:

- The 5 kV extraction voltage produced a flatter meniscus shape; its penetration into the plasma is reduced to 2.36 mm from 3.4 mm at 10 kV of extraction voltage.

- The reduction of the co-extracted electron current by a factor ∼5 can be attributed to the flatter meniscus, allowing a further reduction of the electron density by the filter field before reaching the meniscus.

- The reduction by a factor ∼2 of the extracted current is due to the reduced meniscus surface and the reduced intensity of the electric field produced by the voltage difference between the PG and the EG.

- The majority of the extracted current is still generated in the conical part of the PG, representing 54 % of the total extracted current.

The extracted current composition by its origin along with a comparison to the BATMAN standard case is detailed in the table 6.2; the negative ion current is divided according to their origin: from the PG (Conical and Flat part); originated by electron collisions with the neutral atoms (Coll); and initially inserted in the source region (Volume).

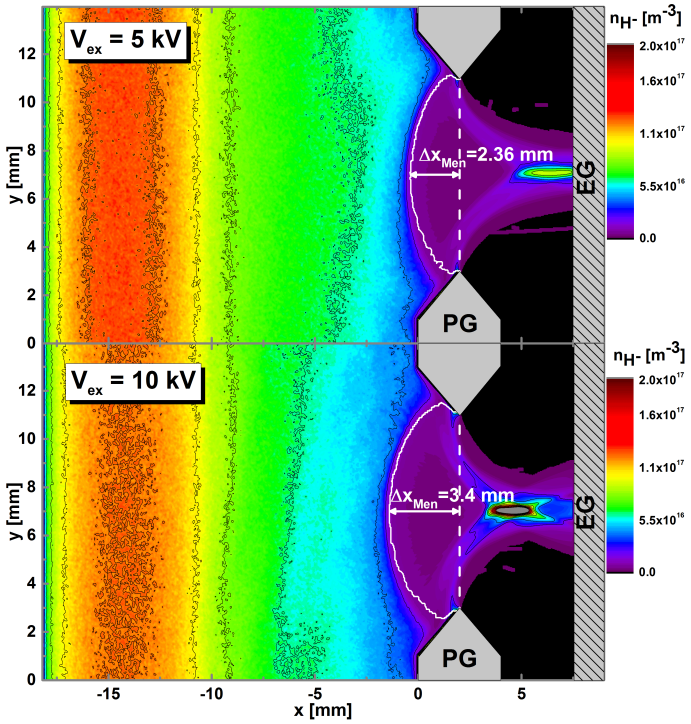

Figure 6.8: Negative ions density maps in the xy plane: Top) 5 kV extraction voltage; Bottom) 10 kV extraction voltage. The meniscus is marked by the white curve

	$\mathbf{V_{ex} = 5kV}$	$\mathbf{V_{ex} = 10kV}$
Total $[\mathbf{Am^{-2}}]$	140	251
Conical	54%	66 %
Volume	38%	32%
Coll	5%	1.7%
Flat	3%	0.3 %
$\mathbf{j_e}$ $[\mathbf{Am^{-2}}]$	20	115
$\frac{j_e}{j_{ex}}$	0.14	0.46

Table 6.2: Extracted current details for the BATMAN extraction aperture geometry with $V_{ex} = 5$ kV and $V_{ex} = 10$ kV.

Figure 6.9 shows the density profile along the beamlet axis for both cases. The density profile for electrons outside the source region does not suffer any relevant change, as the magnetic field has not been modified. However, the smaller penetration of the meniscus in the plasma for $V_{ex} = 5$ kV results in a smaller electron density at the meniscus, explaining the reduction in the co-extracted electron current. The plasma potential is reduced by 0.6 V for V_{ex} =5 kV due to the higher amount of negative ions present in the plasma.

The peak in the negative ion density profile after the PG shows the focus point

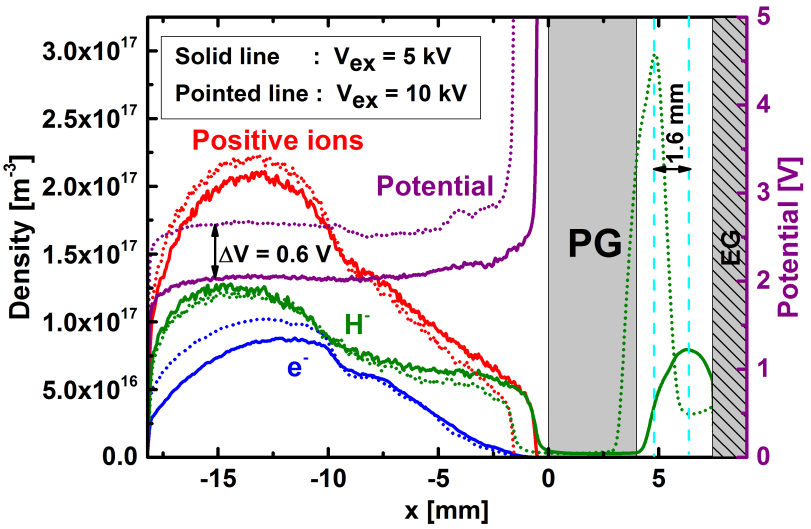

Figure 6.9: Densities and potential profiles in the beamlet axis line of sight, for aextraction ponteitla of 5 kV (solid line) and 10 kV (dotted line.)

of the beamlet, in both cases. The focus point is shifted closer to the EG by 1.6 mm for $V_{ex} = 5$ kV, while the meniscus shifted by 1 mm in the same direction. It means that the relation between the meniscus position and the beamlet focus point is not strictly linear. This non-linearity can be associated with the meniscus curvature and the perveance.

The perveance has a dependence of the form $\Pi \propto \frac{1}{d^2}$ with respect to the distance d between the emitting surface and the extraction grid. Thus, using the distance from the EG to the middle point of the meniscus, it is obtained that $\Pi_{10kV} \propto \frac{1}{8.9^2 mm^2} = 0.012$ mm^{-2} and $\Pi_{5kV} \propto \frac{1}{7.86^2 mm^2} = 0.016$ mm^{-2}. Thus , the lower penetration of the meniscus, associated with a lower curvature, represents a smaller perveance which is then related to the transition from an over-focused beam to a beam with a focus point in the EG position. Figure 6.10 shows the negative ion density profile at the EG for a extraction potential of 5 kV and 10 kV. The halo of the beam associated with an over-focused beam in the case for $V_{ex} = 10$ kV is reduced for $V_{ex} = 5$ kV.

6.1.3 Aperture geometry influence

The extraction aperture geometry is a design parameter of NBI ion sources that influences the extracted beam optics, as it changes the boundary conditions for the electrostatic potential in the extraction region. Thus, the geometry of the extraction aperture influences the penetration of the extraction potential into the plasma side.

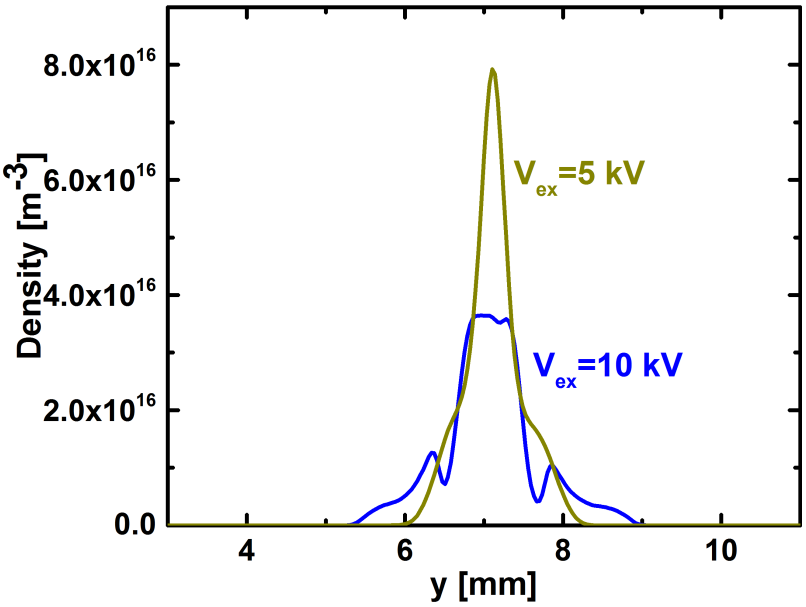

Figure 6.10: Negative ion density profile at the EG for a extraction potential of 5 kV and 10 kV .

Consequently, the meniscus shape depends on the extraction aperture geometry and so does the beam optics.

A variation of the aperture geometry respect to the conical geometry was analyzed to evaluate its influence on the meniscus shape and position. The aperture geometry was changed to a cylindrical one, deleting the conical region of the BATMAN geometry. The diameter of the extraction aperture was kept at 8 mm. The production of negative ions in the cylindrical aperture was restricted to the flat region facing the plasma side. No negative ions were emitted from the inner part of the cylindrical aperture; the assumption is that the flux of neutral atoms do not effectively flow onto the inner sides of the aperture.

Figure 6.11 shows the negative ion density for the cylindrical and standard conical BATMAN aperture geometry in the xy middle plane, with the meniscus shape highlighted by the white curve. The cylindrical aperture produced a flatter meniscus shape along with a beamlet that is focused at the EG. The meniscus penetration on the plasma side is reduced to 3 mm in the cylindrical aperture with respect to the 3.4 mm in the conical BATMAN aperture. The slightly reduced penetration of the meniscus can be attributed to the different boundaries conditions for the electrostatic potential at the PG aperture. The flat aperture geometry enforces a 0 V condition through an overall narrow aperture.

The directly extracted particles which produced the beam halo are reduced as

the conical part is taken out and the meniscus becomes less penetrating. The extracted current density is reduced to $j_{ex} = 59$ Am^{-2} in the cylindrical geometry, i.e. by a factor of 4. The co-extracted electron current density sets to $j_e = 69$ Am^{-2}, implying a reduction of almost a factor 2. The reduction in the extracted current can be attributed to the reduced PG surface, where negative ions are produced, and the reduction of the extraction probability by the change of the aperture geometry [34]. The negative ion production surface is reduced from ∼172 mm^2 in the conical BATMAN geometry to ∼146 mm^2 in the cylindrical geometry; this represents a reduction of 15% of surface emitted negative ions. Furthermore, the geometry changed the preferential velocity direction of the surface emitted negative ions, reducing their extraction probability [34].

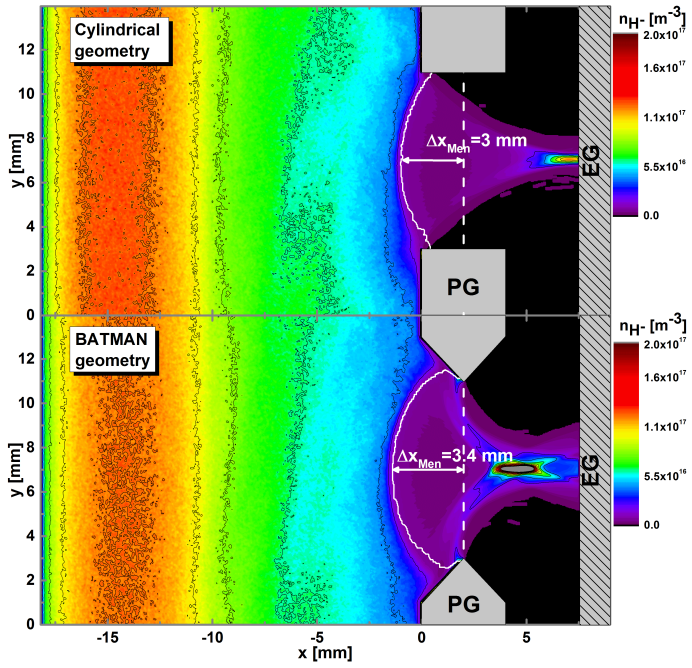

Figure 6.11: Negative ions density maps in the xy plane: Top) Cylindrical aperture; Bottom) BATMAN aperture. The meniscus is marked by the white curve.

Figure 6.12 shows the density and potential profiles along the beamlet axis for the cylindrical and conical BATMAN geometries. The flatter meniscus is associated in this profile by the reduction of the positive ion density to zero taking place 0.5 mm closer to the PG. Because the magnetic field is identical in both cases, the electron density profile is almost unchanged outside the source region. The lower electron density at the meniscus position and the smaller meniscus surface area explain the observed reduction of the co-extracted electron current.

The flat extraction aperture results in an extracted ion beam that is not longer over-focused and a lower co-extracted electron current density. However, the higher reduction in the extracted current density results in a higher electron-ion current density ratio of $\frac{j_e}{j_{ex}} = 1.17$ compared to the standard case.

Table 6.3 summarize the details of the extracted and co-extracted electron current density. In the cylindrical geometry most of the beam is formed by the negative ions (Volume) initially set in the source region. However, the net extracted current density produced by these negative ions is reduced to $\sim$51 Am^{-2}, compared to the $\sim$80 Am^{-2} obtained in the conical geometry. The decrease is due to the reduction of the meniscus surface, which limits the total amount of negative ions crossing the meniscus and forming the beam.

	Cylindrical	**Conical**
Total [Am^{-2}]	59	251
Conical	0%	66 %
Volume	86%	32%
Coll	9%	1.7%
Flat	5%	0.3 %
$\mathbf{j_e}$ **[Am^{-2}]**	69	115
$\frac{\mathbf{j_e}}{\mathbf{j_{ex}}}$	1.17	0.46

Table 6.3: Extracted current details for the cylindrical and standard conical BATMAN aperture geometries.

In the flat aperture geometry more negative ions are now directed to the plasma, and therefore the higher amount of negative ions in the plasma reduces the plasma potential drop by 0.4 V compared to the conical geometry.

The negative ion focal point, marked in figure 6.12 by the density peak after the PG, was shifted by 2.2 mm to the EG. This shift was higher than that of the meniscus penetration in the same direction, demonstrating that the geometry of the plasma grid aperture is highly influential on the position of the beam focus point.

The plasma facing inner half of the conical aperture was chosen to increase the extraction probability of the surface produced negative ions [34]. However, up to now there is no argument for the use of the conical downstream half. The results obtained from the simulation of a flat geometry suggests that this configuration can improve the beam optics, by shifting the focal point closer to the EG. Thus, a combination of both geometries (inner conical and downstream flat) could produce the high extracted current densities achieved in the conical geometry and reduce the deep penetration of the meniscus, avoiding the production of an over-focused beam.

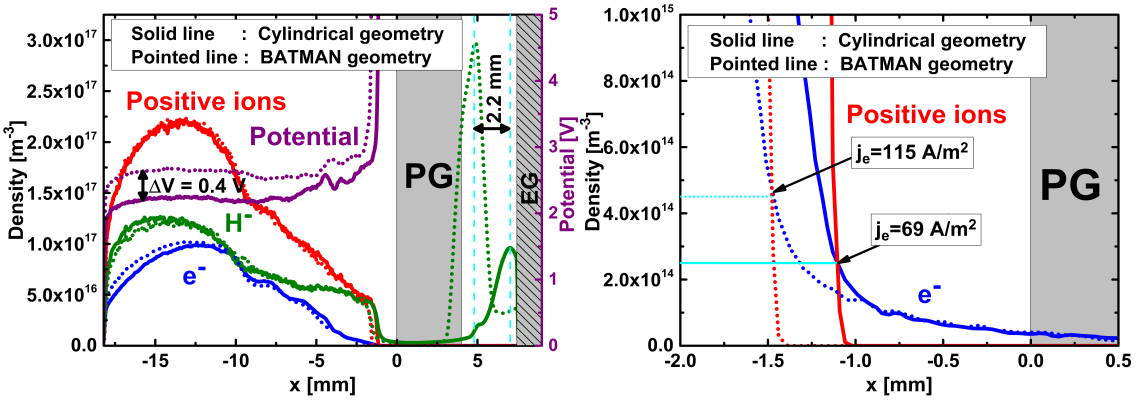

Figure 6.12: Densities and potential profiles in the beamlet axis line of sight, as marked in figure 6.2, for a cylindrical aperture(solid line) and the BATMAN aperture geometry (dotted line).

6.1.4 Negative ion emission homogeneity

Due to the depletion of Cs and the creation of Cs compounds over the PG, it is probable to find a non-homogeneous work function over the PG. This leads to an inhomogeneous emission of negative ions from the PG surface. This is probable to be found in negative NBI ion sources, specially in long pulses. The effects of the inhomogeneous negative ion emission from the PG, on the extracted ion current density and the co-extracted electron current density, cannot be studied in the experiments; mainly, due to the impossibility to determine the work function over the PG during the extraction pulses.

The former simulations done by ONIX have shown that the plasma does not reach the PG homogeneously, in the extension of one extraction aperture. For example, in the standard case, the tips of the conical part of the aperture are not reached by the plasma. Thus, in the this region the rates of removal of Cs compounds and the deposition of Cs by the plasma is lower, compared to the regions where the plasma reaches the surface. This scenario produces an inhomogeneous work function, and therefore an non-homogeneous emission of negative ions in the local extension of one extraction aperture.

To analyze the effect of a local non-homogeneous surface emission of negative ions, the emission surface of the PG was modified in ONIX. The emission from the flat part of the PG was unchanged, but the conical part was set such that negative ions were emitted only from the most inner half section of the conical part, as marked in figure 6.13. This represents the uneven distribution of Cs and/or the different work functions in the region barely reached by the plasma, as it is downstream the

meniscus. In this way the conical emitting surface $S_{conical}$ is reduced from 89 mm^2 to 49 mm^2, representing a reduction by a factor of 1.8. The emission rate of negative ions from the surface is set to the same value (550 A m^{-2}) for both cases.

Figure 6.13 shows the negative ion density distribution map in the xy plane along with the meniscus shape, for the half emitting surface and the entire emitting surface case. The extracted beam is focused at the EG for the half-emitting surface, in contrast with the entire emitting surface. This is due to the reduction of the directly extracted negative ions from the tip of the conical part, eliminating an important contributor of the over-focused beam. The extracted current density is reduced to $j_{ex} = 112$ Am^{-2}, a decrease by a factor of 2.2 with respect to the standard case. Thus, there is a discrepancy between the reduction factors of emission surface and extracted current density. This points that the directly extracted ions represent a higher fraction of the extracted current density than the negative ions emitted from the most inner half section of the conical part of the PG.

Two changes are noticed in the meniscus. The meniscus penetration increases by 0.35 mm respect to the entire emitting surface case. The meniscus shape is modified in the region where negative ions are not longer emitted. The meniscus marking the extension of the plasma is not longer present in the tip part of the conical section of the aperture. It means that positive ions do not longer reach this region. The reason for this is that with an entire emitting surface the emitted negative ions screen the extraction potential close to the PG, then the positive ions are able to reach this region. The screening of the extraction potential by the emitted current from a surface is proofed in the derivation of the Child-Langmuir law [46]. The suppression of the emission of negative ions in this region removes also the screening of the extraction potential, limiting the reach of the positive ions, and therefore modifying the shape of the meniscus. This results show that the emission rate influences the meniscus shape, and therefore it will also influence the optics of the beam.

Figure 6.14 shows the beamlet axis profiles for the potential and densities for the half and entire emitting surface cases. The plasma potential increases by 0.3 V for the half-emitting surface with respect to the standard case; this is due to the lower production of negative ions in the half emitting surface case. The positive ion density and negative ion density profiles do not present relevant changes, with the exception of the profiles being pushed 0.35 mm into the plasma side for the half-emitting case. The electron density profile, however, it's significantly modified as is the co-extracted electron current. The co-extracted electron current density increases to $j_e = 217$ Am^{-2} with respect to the standard case, giving a worst electron-ion ratio of $\frac{j_e}{j_{ex}} = 1.93$.

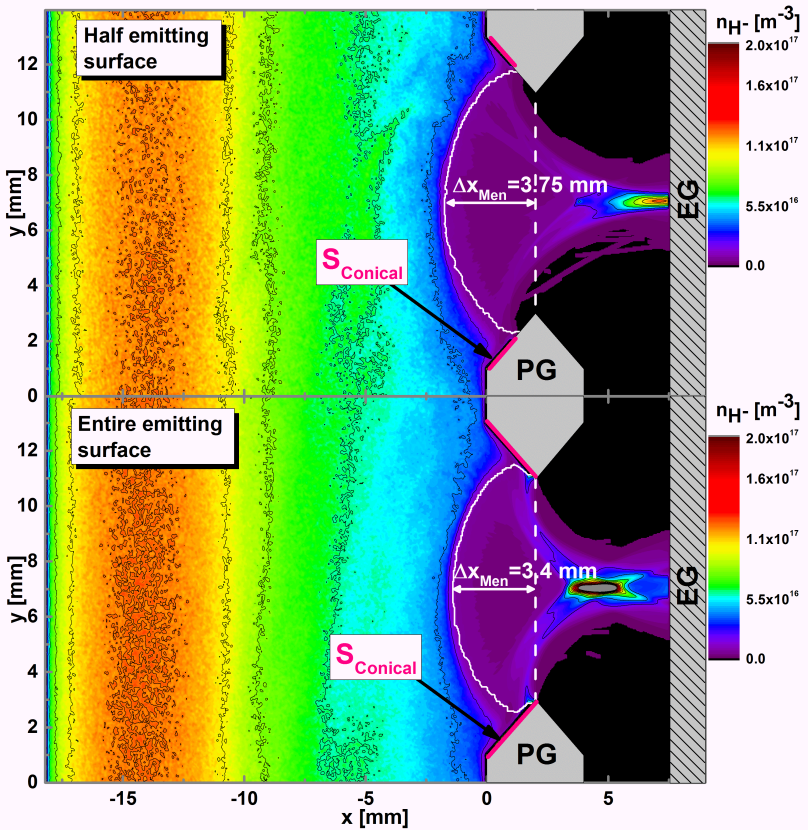

Figure 6.13: Negative ion density maps in the xy plane: Top) Half emitting surface in the conical part; Bottom) Entire emitting surface. The meniscus is marked by the white curve.

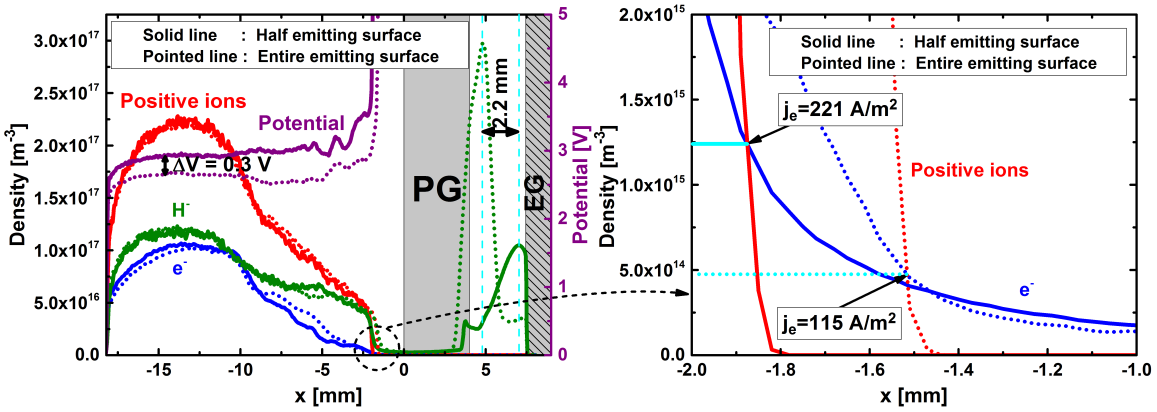

Figure 6.14: Densities and potential profiles along the beamlet axis, as marked in figure 6.2, for a half emitting conical surface (solid line) and entire emitting surface (dotted line).

The high increase in the co-extracted electron current density can be, partially, explained by the deeper meniscus penetration into the plasma in the half emitting surface case. Figure 6.14 shows the electron density and the positive ion density for both cases in the region at very close vicinity to the meniscus. The increase of the meniscus penetration by 0.35 mm results in a electron density ∼2.5 times higher at the meniscus position for the half emitting surface. Thus, a higher flow rate through the meniscus surface is obtained in the half emitting surface case, and therefore a higher co-extracted electron current is obtained.

Table 6.4 summarize the details of the extracted and co-extracted electron current. In this case the negative ions emitted from the conical part of the PG do not longer represent the majority of the extracted beam. Instead, the beam consist mainly of negative ions deposited initially in the source region.

	Half − surface	**Entire − surface**
Total [Am^{-2}]	112	251
Conical	13%	66 %
Volume	82%	32%
Coll	4%	1.7%
Flat	1%	0.3 %
j$_e$ [Am^{-2}]	217	115
$\frac{j_e}{j_{ex}}$	1.93	0.46

Table 6.4: Extracted current details for a half and entire emitting conical surface.

This simulation have shown the influence of a non-homegenous negative ion emission from the PG on the co-extracted electron current density. A degradation of the

Cs coverage (represented by the lower emission surface in the computational model) has the double effect of not only decreasing the extracted current density, but also increasing the co-extracted electron current. Besides, the emission of negative ions have been found to influence the meniscus penetration and shape, and therefore it also influences the beam optics.

6.1.5 Isotope effect

At the test facilities the co-extracted electron current, in a deuterium plasma, increases over time to the point where the electron-ion ratio goes above one [93]. The higher co-extracted electron current density and its increase over time is stronger in deuterium compared to hydrogen, as shown in figure 2.9. Thus, to keep the ratio $\frac{j_e}{j_{ex}} < 1$ in deuterium, a more intense filter field is required and/or a reduction in the RF power or the extraction potential. As a consequence the extracted current is reduced as well. Up to now, the reason for the different behavior of the co-extracted electron current for the different isotopes has not been explained.

The first and obvious difference between hydrogen and deuterium is the atomic mass. In order to investigate the atomic mass effect on the co-extracted electron current and the plasma, an ONIX simulation varying solely the mass of the ions from hydrogen to deuterium was done.

In the steady state the simulation gave an extracted negative ion current density of $j_{ex} = 182\ Am^{-2}$ and a co-extracted electron current density of $j_e = 147\ Am^{-2}$, giving a ratio $\frac{j_e}{j_{ex}} = 0.8$ which is higher than the 0.46 for hydrogen. The decrease in the extracted current density by a factor 0.72, in deuterium compared to hydrogen, is related to the reduction of the thermal velocity by the mass, factor i.e. $\frac{1}{\sqrt{2}} \sim 0.71$. A reduction in the thermal velocity decrease the flux through the meniscus by the same factor and therefore the extracted current density.

The increase of the co-extracted electron current by a factor 1.28 cannot be directly explained by the change of the ion mass, but rather by effects in the plasma, as explained in the following:

- An electron from the source region can reach the PG only if it has an energy higher than the potential barrier $\Delta\Phi = \Phi_{plasma} + \Phi_{well}$.
- An electron with an energy lower than $\Delta\Phi$ is reflected back to the plasma.
- A heavier positive ion mass in the plasma results in an increased plasma potential drop Φ_{plasma}, see equation 3.16.

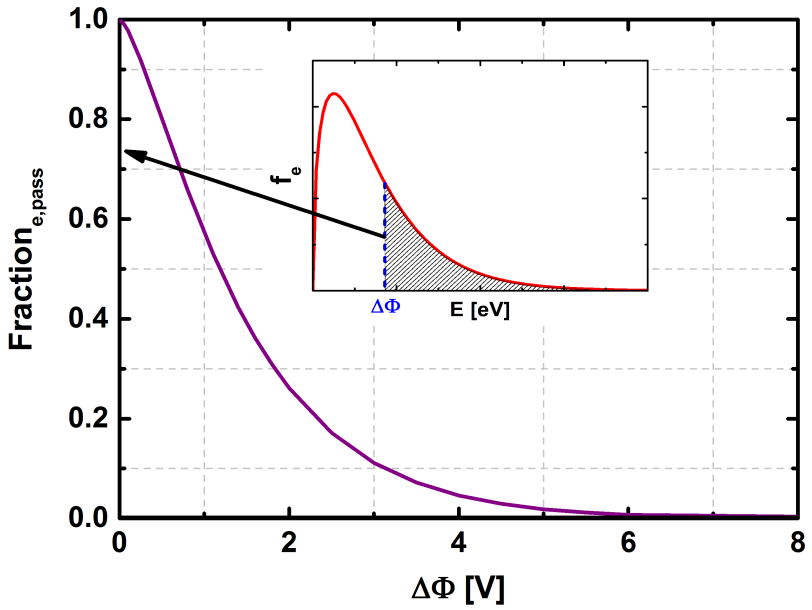

Figure 6.15: Fraction of electrons from a Maxwellian energy (T_e = 1 eV) distribution than can overcome a potential barrier $\Delta\Phi$.

- In deuterium $\Delta\Phi$ is increased with respect to hydrogen and the probability of an electron being destroyed at the PG is decreased.
- The fraction of electrons not reaching the PG and reflected back to the plasma can then be extracted.
- The probability to extract electrons is increased.

Figure 6.15 shows the fraction of electrons, from a Maxwellian energy distribution (with T_e = 1 eV), able to reach the PG in function of the potential barrier $\Delta\Phi$. The fraction of electrons able to overcome the potential barrier is given by integrating the energy distribution function of electrons from $\Delta\Phi$ to the infinity. Thus, for higher $\Delta\Phi$ the integration boundaries are reduced, resulting in a lower fraction of electrons able to reach the PG.

Figure 6.16 shows the border profile line through the PG for the densities and the plasma potential in deuterium and hydrogen. The plasma potential is 3.3 V for deuterium and 2.5 V for hydrogen. At the border profile line, in the xy plane, the potential well in deuterium is 1.4 V giving a total barrier of 4.7 V. The potential well in hydrogen at the same position is 1.1 V, giving a lower potential barrier of 3.6 V. Thus, the initial hypothesis of the increased potential barrier in deuterium is confirmed, not only because of the plasma potential, but also by the increase in the potential well.

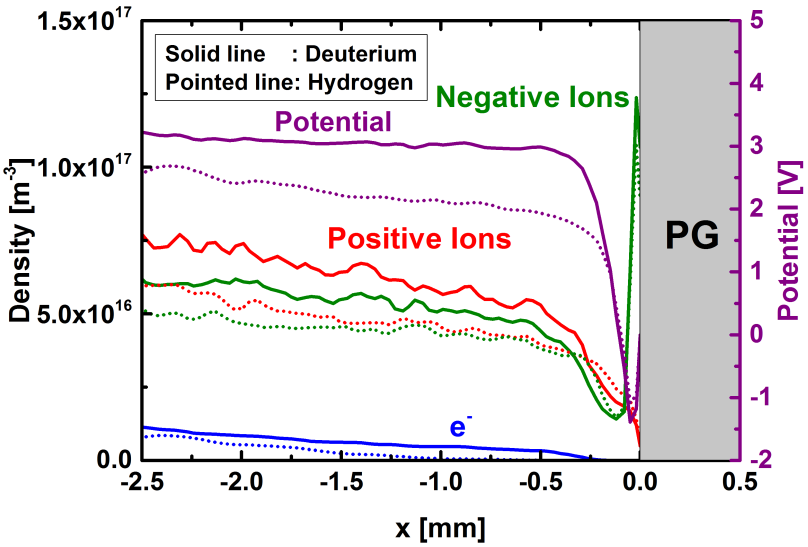

Figure 6.16: Densities and potential profiles in the border line of sight, as indicated in figure 6.2, for deuterium (solid line) and hydrogen (dotted line).

Figure 6.17 shows the negative ion density in the xy plane for deuterium and hydrogen along with the meniscus. The meniscus shape is similar in both cases. The meniscus surface is given by the equilibrium between the forces generated by the pressure and the extraction voltage, and neither of them depend on the isotope mass, thus, the meniscus shape is not influenced by the isotope mass. The negative ion density maps show that the extracted beam for hydrogen and deuterium are also similar. Higher negative ion density values are seen close to the meniscus in the deuterium case, compared to that in hydrogen. The higher amount of electrons reflected from the PG, in deuterium, can also create negative ions by dissociative attachment. Thus, increasing the negative ion density. Besides, the deuterium case required more calculation time until the equilibrium, and therefore slower species such as Cs expand from the source region, allowing a higher negative ion density outside the source region.

Besides the mass effect, a deuterium operation scenario presents a higher dissociation of the gas molecules [94]. A higher dissociation degree means that the flux of neutral atoms from the driver onto the PG is also increased. To analyze the effect of the higher atom flux onto the PG that increases the surface production of negative ions, the emission rate in the model was increased to 770 Am^{-2}.

Increasing the emission rate does not increase significantly the amount of negative ions going into the plasma. The reason is that the potential well depth increases to keep the negative ion flux into the plasma constant [44][45]. Only a slight increase of

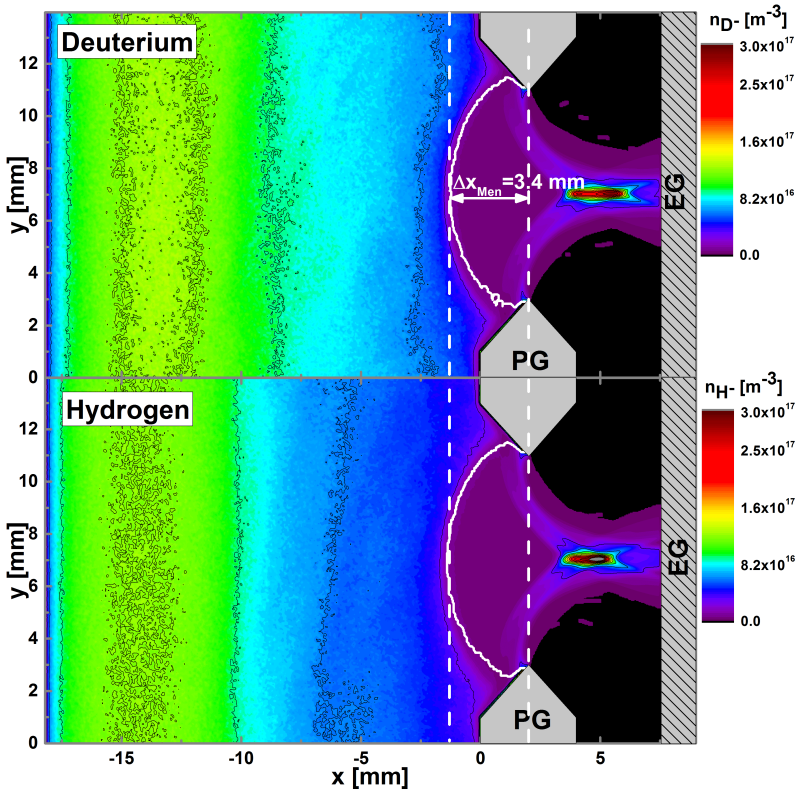

Figure 6.17: Negative ions density maps in the xy plane: Top) Deuterium plasma; Bottom) Hydrogen plasma. The meniscus is marked by the white curve.

the negative ions in the plasma is to be expected, as the potential well is not formed in the region where there are directly extracted negative ions. Therefore, the extracted negative ion current density increases by a factor 1.1, as shown in figure 6.18, being this lower than the factor 1.4 by which the emission rate was increased.

	Hydrogen (550Am^{-2})	Deuterium (550Am^{-2})	Deuterium (770Am^{-2})
$\Phi_{plasma,xy}$ [V]	2.5	3.3	3.2
$\Phi_{well,xy}$ [V]	1.1	1.4	1.7
$\Delta\Phi_{xy}$ [V]	3.6	4.7	4.9
$\Phi_{plasma,xz}$ [V]	2.5	3.3	3.2
$\Phi_{well,xz}$ [V]	0.9	1.2	1.1
$\Delta\Phi_{xz}$ [V]	3.4	4.5	4.3

Table 6.5: Plasma potential drop and potential well through the border profile line in the xy and xz planes.

Table 6.5 summarize the values for the potential drop and potential well at the border profile lines in the xy and xz planes for the three cases. The current density of electrons onto the PG was calculated in order to quantitatively show its dependence

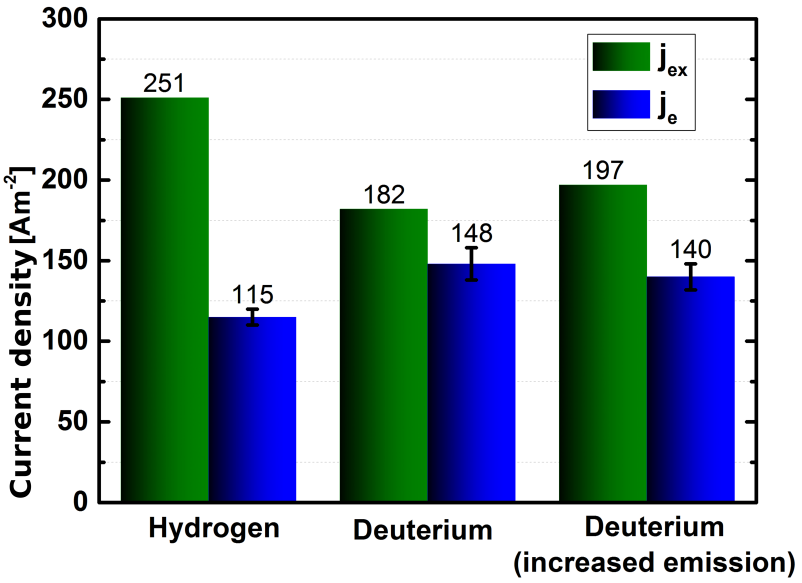

Figure 6.18: Extracted current density and co-extracted electron current density for an hydrogen plasma, a deuterium plasma with a surface emission rate of 550 Am^{-2} and a deuterium plasma with an increased surface emission rate of 770 Am^{-2}.

on the potential barrier. For an hydrogen plasma an electron current density impinging onto the PG $j_{e,PG} = 15.5 \pm 0.3$ Am^{-2} was calculated in the simulation. For deuterium plasma with a negative ion surface emission rate of 550 Am^{-2} a current density of $j_{e,PG} = 5.0 \pm 0.2$ Am^{-2} was calculated, being as expected lower than that of hydrogen. For the deuterium plasma with a surface emission rate of 770 Am^{-2} a electron current density $j_{e,PG} = 4.4 \pm 0.3$ Am^{-2} was measured, it is again much lower than that of hydrogen, and below the value for the standard surface emission rate.

This simulation has given an explanation for the higher co-extracted electron current density and the lower extracted ion current density in deuterium with respect to hydrogen. However, the electron-ion current density ratio does not reach values above 1, as shown in the experimental results in figure 2.9. Nonetheless, as the sputtering yield [95] by deuterium is higher than for hydrogen, the isotope mass effect should be combined with the inhomogeneous (reduced) negative ion emission rate shown in the previous section. As proposal for continuation of the simulations in deuterium, a constant reduction of the surface emission of negative ions over time should be implemented. It could produce an increase of the co-extracted electron current over time. Thus, the electron ion-ratio could reach values above 1.

6.1.6 Plasma phase simulation

Measurements using different plasma diagnostics at ∼2 cm from the PG of the BATMAN and ELISE test facilities show that plasma densities and potential vary between plasma phase (PP) and beam extraction (HV). For example, Langmuir probe measurements [96] taken in the plasma give the values for the electron density, the positive ions density and the plasma potential [97]. The measurements at the extraction region show that the electron temperature is constant in both phases; the electron density decreases by 75% and the positive ion density decreases by 20%, in the PP phase compared to the HV phase within a relative error of 10% for the densities. The potential difference between the plasma and the PG decreases by 0.8 V in the PP respect to the HV phase, within an error of 0.7 V.

This motivated a simulation of the PP, i.e. $V_{ex} = 0$ V. The BATMAN aperture geometry was used and the simulation started from the steady state of the standard case, i.e. $V_{ex} = 10$ kV (HV). The extraction potential was set to zero and the calculation was continued until the plasma expanded and a new steady state was reached.

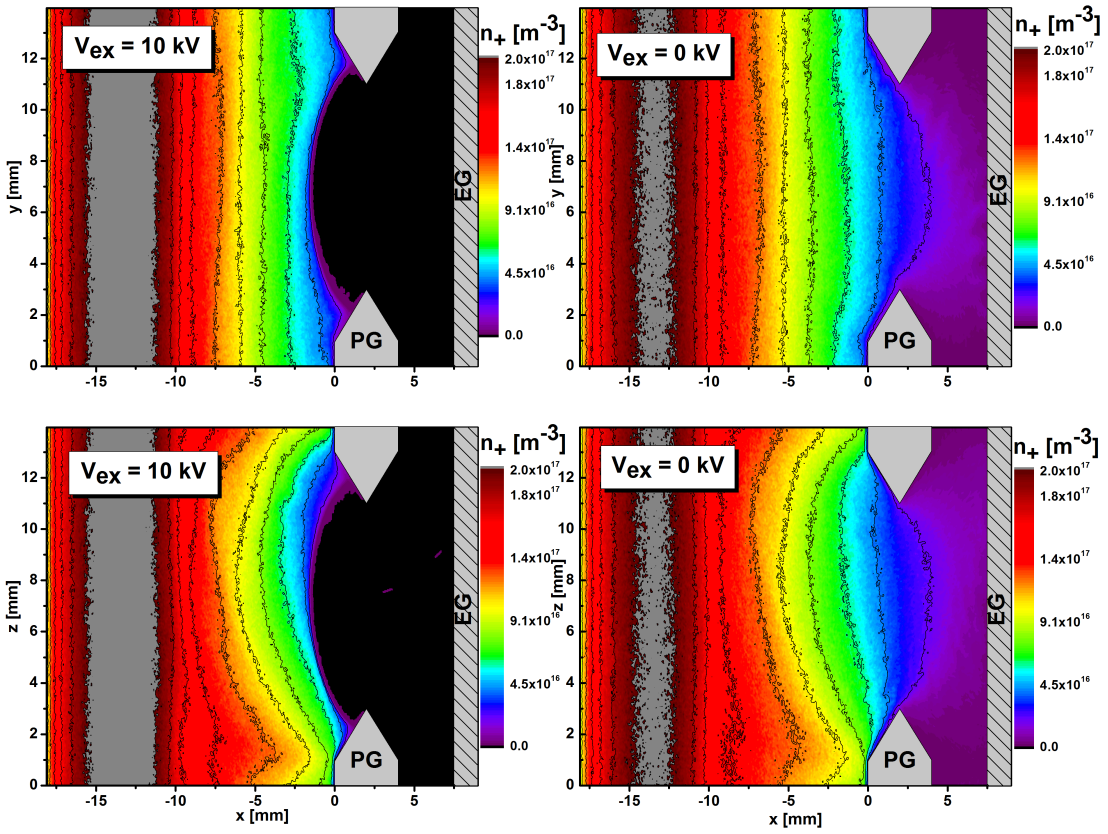

Figure 6.19: Positive ions density in the xy and xz planes for the PP ($V_{ex} = 0$ kV) and the HV phase ($V_{ex} = 10$ kV).

Figure 6.19 shows the positive ion density in the planes xy and xz for both cases. The gray area in the density maps marks densities over $2{\cdot}10^{17}$ m^{-3}. It is clearly seen that the extension of the gray region is diminished for $V_{ex} = 0$ V (PP). The decrease in the positive ion density in the source region is due to the positive ions expanding over the whole domain, as the extraction potential does not longer limit their pass through the aperture. Even though positive ions are present in the region between the PG and EG, they present a strong gradient compared to that seen from the source region to the PG. The higher intensity of the deflection field in this region magnetize the positive ions, and therefore decreases their diffusion rate.

Figure 6.20 shows the electron density maps in the xy and xz planes for PP and HV phase. The electron density is also reduced in the source region in the PP with respect to the HV phase. The electrons flows through the extraction aperture; however, the strong magnetic deflection field between the PG and EG modifies its distribution as they are magnetized; besides, it limits their diffusion in this region. The lower electron density in the source region is explained then by the expansion of the plasma in the region between the PG and EG, and the additional losses of electrons in the EG and the down stream PG surface, as now they act as containing surfaces for the plasma.

Figure 6.21 shows the beamlet axis profile of densities and potential for the PP and the HV given by the simulation. The flow of the magnetized electrons and the less magnetized ion flow is partially equated by the magnetic field; thus, the plasma potential drop is reduced by 0.83 V in the source region for the plasma phase with respect to the high voltage phase.

6.2 ELISE extraction aperture geometry

The magnetic field in the extraction region is a key parameter in the transport of electrons. As explained in chapter 3, the electrons in this region are magnetized and therefore their diffusion depends on the magnetic field topology. In addition, the presence of particle drift velocities due to the electric and magnetic fields modifies the effective diffusion through the magnetic field lines.

A candidate to achieve a reduction of the co-extracted electrons is therefore the magnetic field and its topology. Consequently, the variation of the magnetic field topology should be done initially in the computational model to understand their effect on the electrons transport in detail, and the results used to develop new conceptual modifications in the ion source.

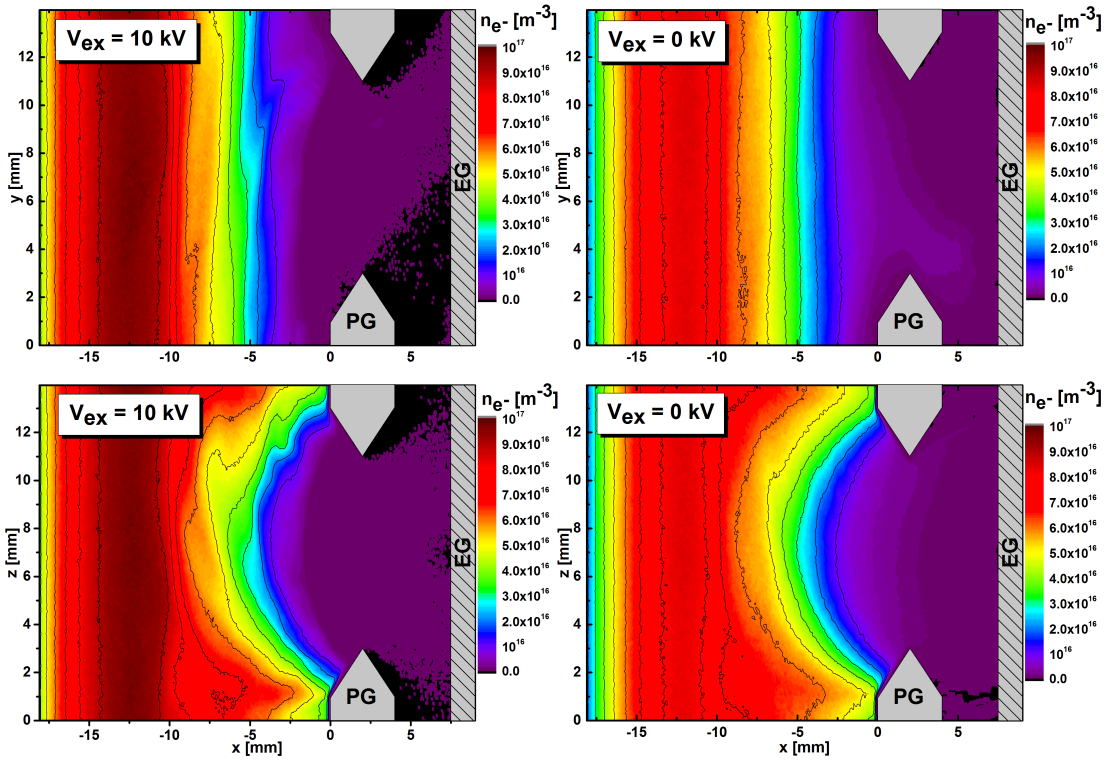

Figure 6.20: Electron density in the xy and xz planes for the plasma phase (V_{ex} = 0 kV) and the high voltage phase (V_{ex} = 10 kV).

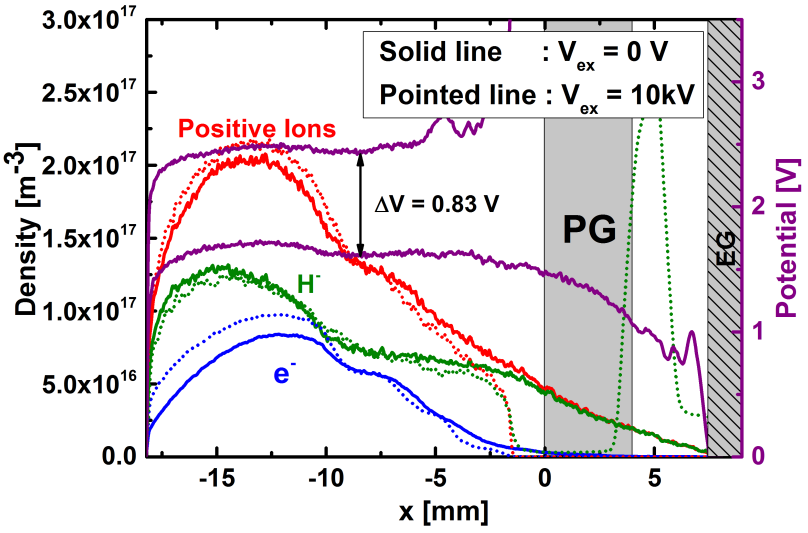

Figure 6.21: Densities and potential profiles along the beamlet axis line of sight, as marked in figure 6.2, plasma phase (solid line) and high voltage phase (dotted line).

6.2.1 ELISE standard case

A simulation using the ELISE extraction aperture geometry was done to understand the changes in the extracted beam compared to the BATMAN geometry and the

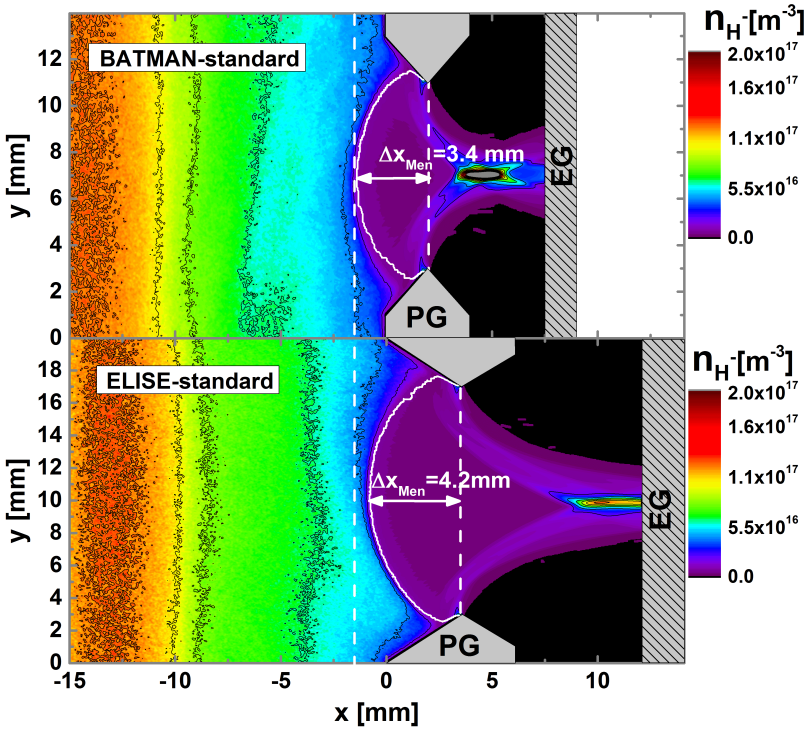

Figure 6.22: Negative ions density maps in the xy plane: Top) Standard BATMAN case; Bottom) Standard ELISE case. The meniscus is marked by the white curve.

influence of the magnetic field topology on the plasma transport. The simulation used the standard physical and numerical parameters, and the extraction potential is set to 10 kV. For the ELISE simulations the potential over the EG was optimized to include the effect of the extraction aperture, the method is described in Appendix A.

As mentioned before, the magnetic filter field in ELISE is generated by a current I_{PG} through the PG. An $I_{PG} = 2.5$ kA is typically used in the experimental hydrogen plasma campaigns [16], and therefore was used for the standard ELISE case. An $I_{PG} = 2.5$ kA corresponds to a field strength of ∼2.0 mT at 5 mm from the PG. Figures of all the components of the total magnetic field in the xy and xz middle planes can be found in the Appendix B.

Figure 6.22 shows the negative ion density in the xy middle plane along with the meniscus curve, for the ELISE and BATMAN standard case. The extracted beam focus point is positioned at the EG for the ELISE standard case, differently to that of the over-focused beam for the BATMAN standard case, implying that the ELISE standard case is closer to the perveance optimum.

At steady state the extracted current density for the ELISE standard case is j_{ex}= 154 Am^{-2}, which is lower than that of the BATMAN case at 251 Am^{-2}. The

distance between the PG and EG is 6 cm in the ELISE geometry, being larger than the 3.5 cm in the BATMAN geometry. A larger distance between grids decreases the electric field if the extraction potential is kept constant. Thus, the extracted ion current density is reduced in the ELISE case, with respect to BATMAN case, due to the larger distances between the grids.

Different extracted ion current densities for the same extraction potential implies that the perveance is different for both cases. However, in order to compared both systems, the perveance has to be normalized by the distance between the meniscus and the EG as the geometry has been changed, i.e. $\Pi_{norm} \propto j_{\mathrm{ex}} \cdot d^2/V_{\mathrm{ex}}^{\frac{3}{2}}$. The meniscus penetration in the ELISE standard case is 4.3 mm, and therefore $\Pi_{norm,ELISE} \propto 2.5{\cdot}10^{-8}$ $\mathrm{Am^{-2}V^{-\frac{3}{2}}}$; comparatively, for the BATMAN standard case $\Pi_{norm,BATMAN} \propto 2.0{\cdot}10^{-8}$ $\mathrm{Am^{-2}V^{-\frac{3}{2}}}$. As it was proved before, the BATMAN case was in the under-perveance regime, and therefore a higher perveance implies that the ELISE standard case is in a regime closer to the perveance optimum. Thus, in the ELISE case the beam is not over-focused and the focus point is closer to the EG position.

The co-extracted electron current for the ELISE standard case is reduced to $\mathrm{j_e}$= 21.2 $\mathrm{Am^{-2}}$, with respect to the $\mathrm{j_{ex}}$= 115 $\mathrm{Am^{-2}}$ for the BATMAN case. However, this reduction cannot be attributed to only one parameter, as not only the aperture diameter has been changed, but also the distance between the PG and EG, geometry of the PG aperture and magnetic field topology. Nonetheless, all the geometrical factors that have influence in the reduction of the electric field, by increasing the distance between the meniscus and the EG, result in a reduction of the extracted ion current density and the co-extracted electron current. To understand the effects of the variation of the magnetic field the geometry should be kept the same and only the magnetic field should be varied. This study will be done in the following, but before it is needed to analyze in detail the effect of the magnetic field in the in the plasma and in transport of electrons.

Figure 6.23 shows the electron density map in the xy plane, and the intensity of the main component of the total magnetic field which for the xy plane is the $\mathrm{B_y}$ component of the magnetic filter field. With a field strength of ∼2.0 mT and an electron temperature $\mathrm{T_e}$ = 1 eV, the electron gyro-radius is ∼0.3 mm, and therefore electrons are magnetized. In this plane the electron distribution follows the structure of the magnetic field with the exception of a pronounced asymmetry close to the PG (x > -4 mm). The electron density presents higher values close to the PG for y < 10 mm.

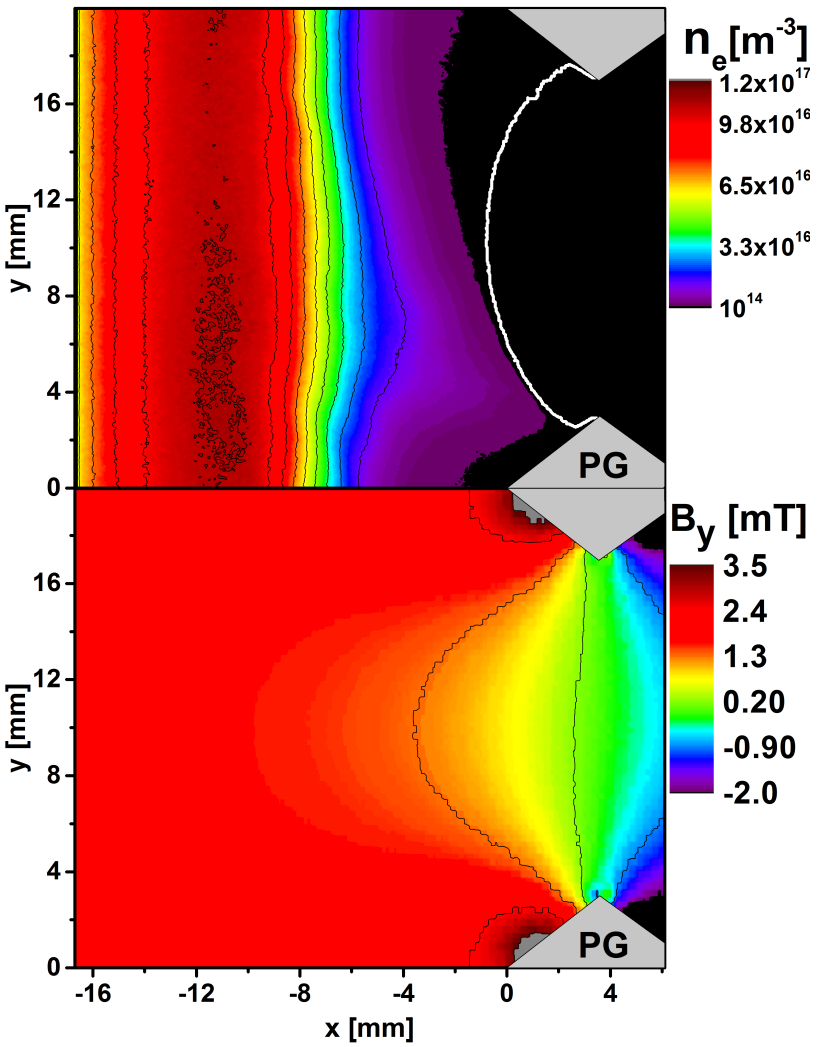

Figure 6.23: Top) Electron density distribution in the xy plane; Bottom) B_y component of the total magnetic field.

Figure 6.24 shows the electron density map in the xz plane along with the intensity map of the B_z component of the magnetic field which is produced mainly by the magnetic deflection field and is predominant in this plane. Due to their magnetization, the electron density presents a structure similar to that of the magnetic deflection field. It can be seen that the influence of the deflection field also reduces the electron diffusion towards the aperture. However, due to the magnetic deflection field curvature, its fields lines go trough the PG, and in the region close to the PG the electron diffusion is not reduced as effectively as through the aperture. The electron distribution in the xz plane also shows a slight asymmetry over the z = 10 mm line. The asymmetries found in both the xy and xz plane are due to a drift velocity that

gives the electrons a preferential velocity direction.

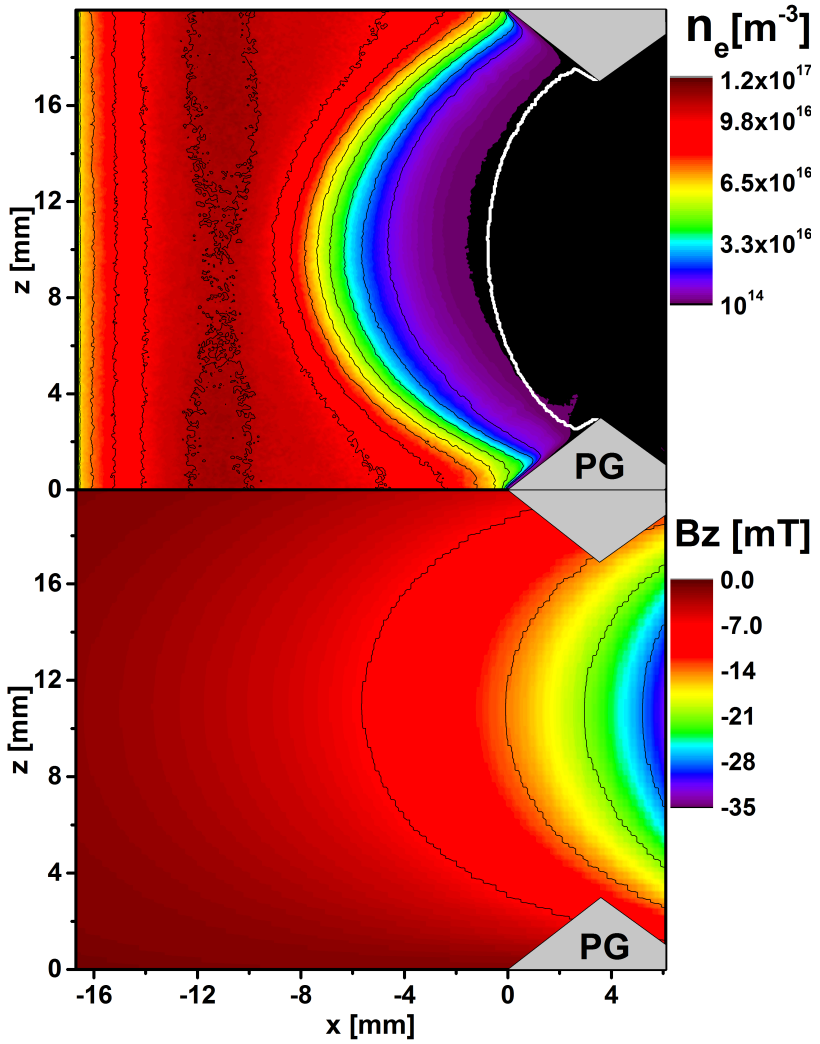

Figure 6.24: Top) Electron edensity distribution in the xz plane; Bottom) B_z component of the total magnetic field.

A drift velocity $v_{\text{drift}} = \frac{m_s v_{||}^2 + m_s v_{\perp}^2/2}{q_s B} \frac{\mathbf{B}\times\nabla B}{B^2}$ produced by the magnetic field gradient and curvature, generates a charge dependent velocity drift. The drift velocity in the xy plane has to be originated by the gradient of the deflection field, while the drift velocity in the xz plane has to be produced by the gradient of the filter field. The gradient of the deflection field is higher than that of the filter field, thus the drift velocity in the xy plane is higher than that in the xz plane.

Figure 6.25 shows the average electron flow Γ_e and positive hydrogen ion flow Γ_{H^+} in the xy and xz planes. Due to the thermalization process electrons are not magnetized inside the source region, and therefore they do not show any preferential

velocity direction. However, in the xy plane outside of the source region they move along the B_y fields lines with a preferential $-y$ velocity direction. The magnetized electrons moving along the filter field lines with the drift velocity in the $-y$ direction eventually diffuse in the direction perpendicular to the magnetic field, and are extracted when they reach the meniscus. This preferential velocity in the $-y$ direction produces the asymmetry found in the electron density over this plane. In the same plane the positive hydrogen ions flow onto the PG due to the plasma sheath formation. Nonetheless, a preferential $+y$ velocity direction is seen due to the charge dependent drift velocity.

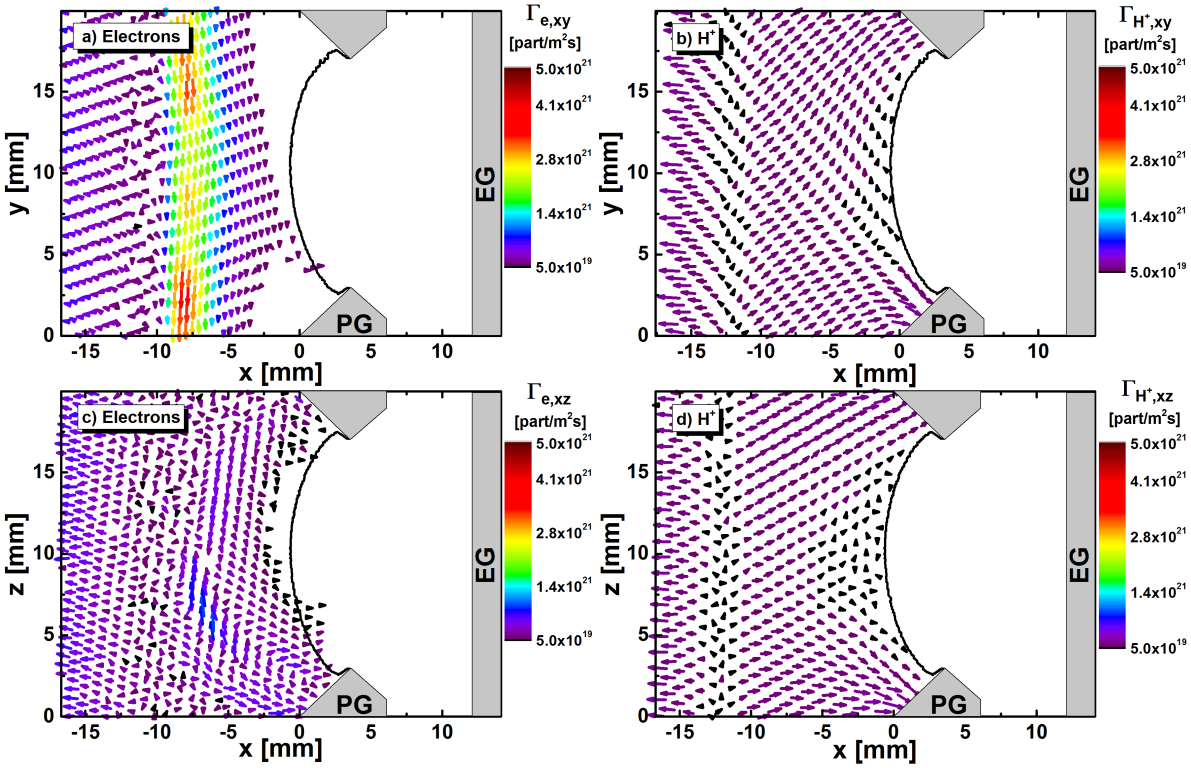

Figure 6.25: a) Vector map of the flow for electrons $\Gamma_{e,xy}$ in the xy; b)Vector map of the flow $\Gamma_{H^+,xy}$ for H^+ in the xy; c)Vector map of the flow $\Gamma_{e,xz}$ for electrons in the xz; d) Vector map of the momentum $\Gamma_{H^+,xz}$ for H^+ in the xz.

In the xz plane the electron flow through the PG aperture is reduced, but still higher than that in the xy plane. The flow of electrons onto the PG is not reduced in the xz plane compared to that in the xy plane due to the structure of the magnetic deflection field. A preferential electron flow in the $-z$ direction is observed. This drift velocity is the cause of the asymmetry over the beamlet axis found in the electron density distribution. In this plane the flow of the positive hydrogen ions is more symmetric through the beamlet axis; however, a preferential $+z$ flow also takes place,

but in a smaller scale compared to the one found in the xy plane due to the drift velocity being smaller in this plane.

It is noticeable that the flow of electrons onto the PG is drastically reduced in the xy plane compared to that in the xz plane. Besides, in the flow map of electrons in the xz plane, some regions present a flow in the $+z$ direction despite of the drift being in the $-z$ direction. This regions denote that, despite of the (dominant) drift velocity, in average a non-negligible fraction of the electrons still flow in the $+z$ direction. To understand the origin of these regions, an analysis of the individual electron trajectories is necessary.

Figure 6.26a shows electrons trajectories projected in the xz plane. As mentioned before, electrons in the source region are not magnetized, and therefore they show random walk like trajectories. Electrons under the influence of the deflection field follow the magnetic field lines. However, some of them are reflected by the potential barrier $\Delta\Phi$, shown in figure 6.26b, when approaching the PG. The reflected electrons continue their trajectories afterwards over the field lines, but in the opposite direction. The process of being reflected at the other extreme of the PG is repeated until they reach the meniscus and are extracted.

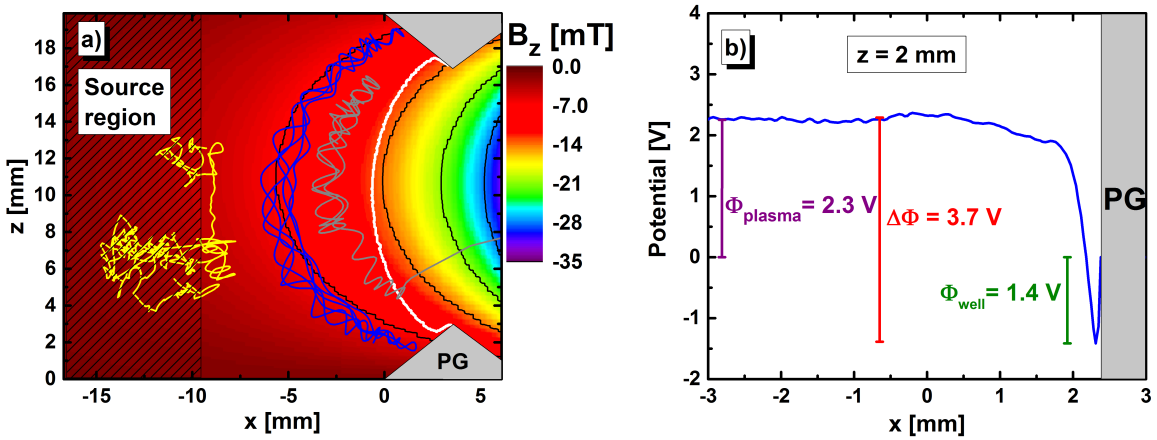

Figure 6.26: Left) Electron trajectories in the xz plane, marked in white is the meniscus; Right) Potential profile over a line crossing the PG at z = 2mm.

The electron flux onto the PG is not the same in the xy and xz plane due to the 3D topology of the magnetic field, as shown in figure 6.25. This inhomogeneous electron flow onto the PG modifies the potential well over the PG plane. This can be seen in figure 6.27 , showing the potential well over the yz plane of the PG. The potential well is not homogeneous, and a structure for its gradient can be distinguished. The potential well is reduced in the segments where the deflection field is predominant and

is higher where the filter field is predominant (electron flow reduced). The potential barrier reflecting the electrons is then not constant over the surface of the PG.

The structure of the potential is modified to keep a quasi-neutral plasma and different electron fluxes onto the PG are compensated by different negative ion flux from the surface into the plasma. Different negative fluxes from the surface into the plasma are possible by a variation of the potential well.

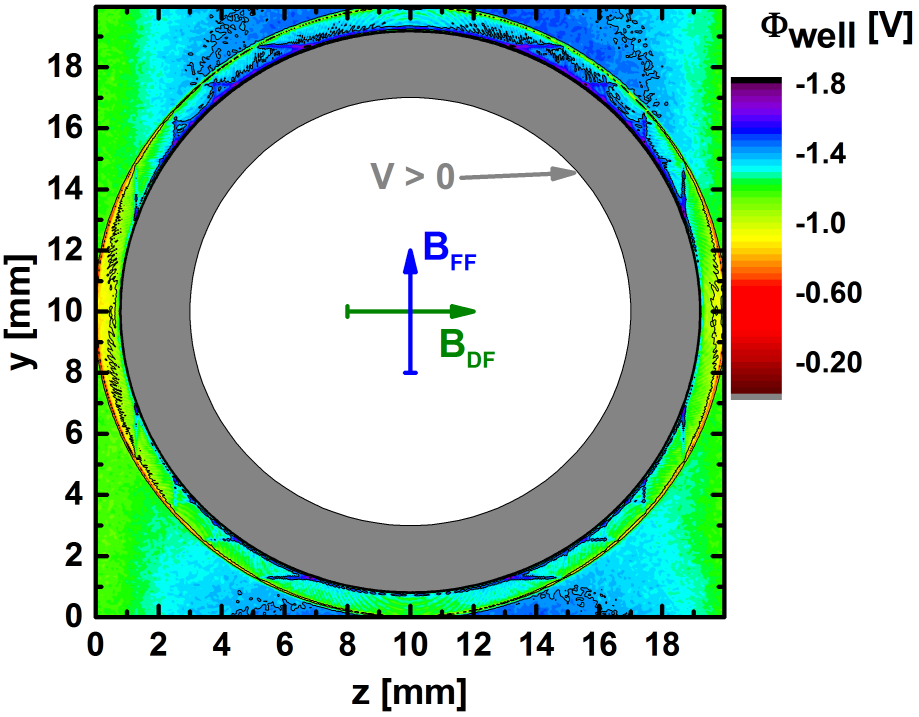

Figure 6.27: Potential well variation over the plane parallel to the PG. Marked in gray is the region of the PG where no potential well has formed. Marked in white is the aperture.

Figure 6.28 shows the negative ion density profile of the beamlet at the position of the EG, in the y and z direction. The profiles are not identical, demonstrating that the beam is not homogeneous. The peak of the distribution is more deflected from the aperture center for the y direction respect to the z direction. The higher deflection in the y direction is due to the intensity increase of the deflection field as the particles get closer to the EG.

To quantitative evaluate the asymmetry of the extracted beam, the emittance in the y and z direction were calculated. The emittance at x = 7.5 mm in the y and z direction are 0.22 mm·rad and 0.20 mm·rad respectively. However, the beam divergence in both directions was found to be the same at 0.46 rad. Therefore, the

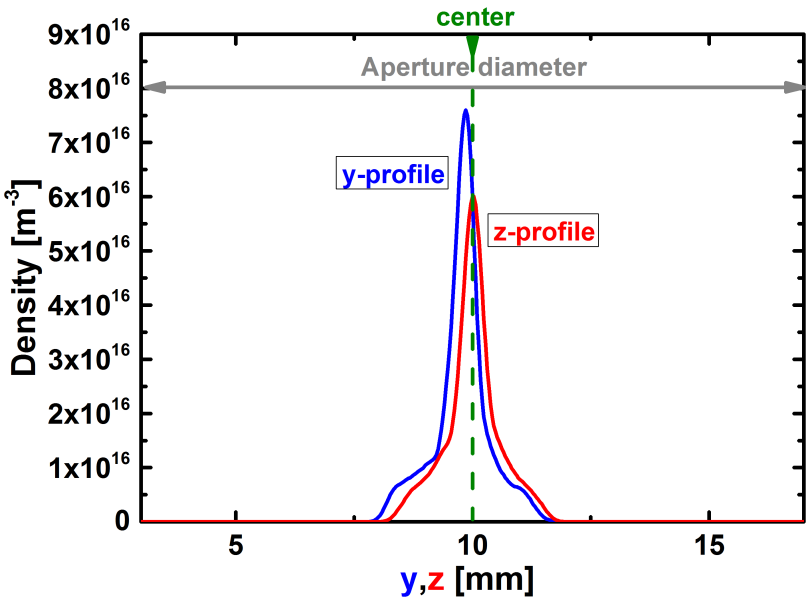

Figure 6.28: Negative ion density profiles in the y (blue line) and z (red line) direction at the EG position.

asymmetry of the beam at the EG is not due to non equal divergences of the extracted beam, but rather to spatial inhomogeneity. It should also be noted that the divergence of the beam is calculated just at the exit of the EG, and therefore the beam has not been fully accelerated. The acceleration of the beam decreases the beam divergence, thus, the given divergence should not be compared to that of the ITER requirements.

6.2.2 Evaluation of different magnetic field configurations

Since both the filter and deflection magnetic field have shown to have a strong influence on the electron dynamics close to the extraction aperture, simulations varying the deflection and magnetic field intensity have been performed. The purpose was to identify if a higher intensity of one of these fields can lead to a reduction in the co-extracted electron current. Three different cases are compared: 1) standard configuration, 2) an intensified filter field by a factor 2, and 3) an intensified deflection field by a factor 2. It has to be kept in mind, however, that an intensified FF will affect all plasma parameters at the source region position and this is not done in ONIX.

Figure 6.29 shows the electron density maps in the plane xz for the three cases. The intensified FF case does not present any significant change in the electron density

distribution compared to the standard case. The meniscus shape is the same and presents the same penetration of $\Delta x_{Men} = 4.2$ mm into the plasma.

The intensified DF case presents an electron density distribution more restrained into the plasma source compared to the standard case. The reason is that the more intense deflection field diminishes the diffusion of the electrons from the source region to the PG; a higher electron density is then seen in the source region.

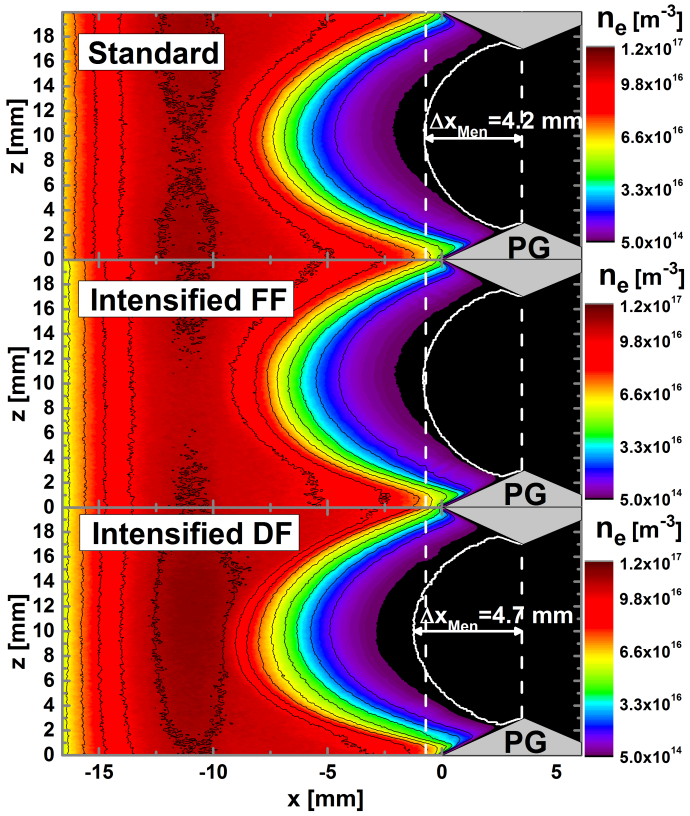

Figure 6.29: Electron density map in the xz plane. Three cases are compared: standard magnetic field configuration, intensified magnetic filter field and intensified deflection field. The meniscus shape is marked by the white curve.

Figure 6.30 shows the electron density map in the xy plane for the three cases. The intensified FF does not change the electron density distribution compared to that of the standard case. The intensified DF reduce the electron diffusion from the source region, and therefore a higher electron density is found in the source region.

The co-extracted electron current density in the intensified FF case is $j_e = 19.5$ Am^{-2} and thus similar to that in the standard case $j_e = 21.2$ Am^{-2}. The effect of the filter field extends further beyond the 2 cm from the PG, and its main effect is in reducing the electron density and temperature from the driver to the PG. Thus, its intensity

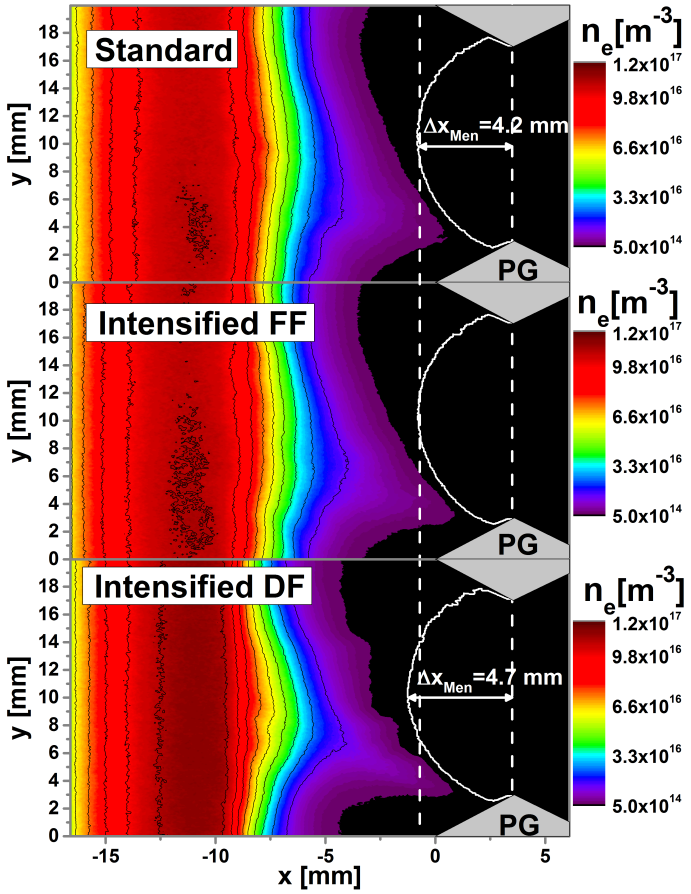

Figure 6.30: Electron density map in the xy plane. Three cases are compared: standard magnetic field configuration, intensified magnetic filter field and intensified deflection field. The meniscus shape is marked by the white curve.

seems not to be relevant once the electron temperature and density have been reduced in the vicinity of the PG.

For the intensified deflection field the co-extracted electron current is reduced to $j_e = 5.2$ Am^{-2}, i.e. by a factor 4. The reduction of the co-extracted electron current for an intensified DF is the result of the combination of two effects:

- The deflection field restrain the electrons into the source region.
- The stronger magnetization of the electrons by the DF increases the probability of electrons reaching the PG.

An intensified deflection field decreases the diffusion rate of electrons through the magnetic field lines, increasing the time needed to cross over the magnetic field lines before being extracted. During this time the electrons are reflected more often at the

potential barrier close to the PG surface. Thus, increasing the probability to reach a point along the PG surface where the potential barrier is smaller, as shown in figure 6.27.

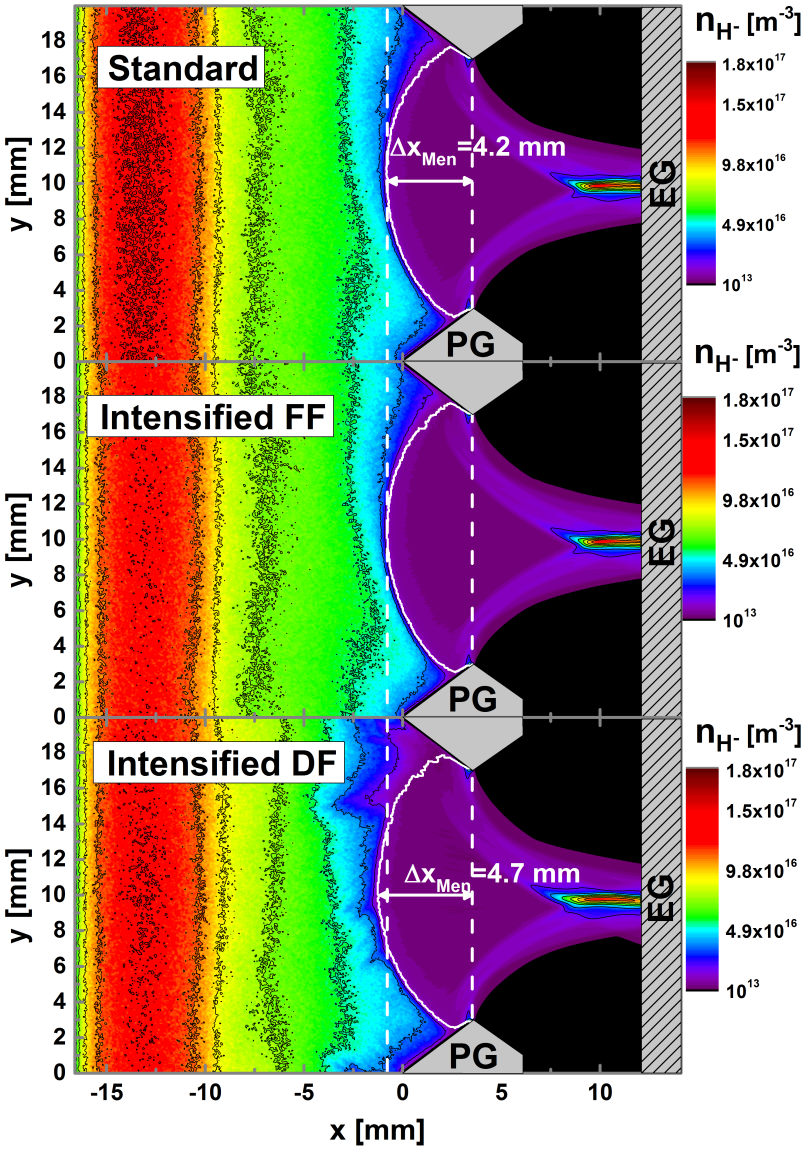

Figure 6.31: Negative ion density map in the xy plane. Three cases are presented: standard magnetic field configuration, intensified magnetic filter field and intensified magnetic deflection field. The meniscus shape is marked by the white curve.

Figure 6.31 shows the negative ion density map in the xy plane for the three cases under investigation. The increased filter field intensity does not change the negative ion density distribution with respect to the standard case. Negative ions are not strongly magnetized, thus an effect of the magnetic field on their distribution is

mainly due to the magnetization of the electrons and the plasma re-arrangement to keep its quasi-neutrality. This is in agreement with the unvaried electron distribution. As the meniscus shape and position are also unchanged, the beam focus point is the same in the two cases.

The intensified deflection field increases the meniscus penetration to $\Delta x_{\mathrm{Men}} = 4.7$ mm, shifting the beam focus ~1 mm further from the EG, i.e. over-focusing the beam. The intensified deflection field has shown to restrict the flow of electron from the source region to the PG. This restriction on the electron flows modifies the whole plasma distribution, modifying the meniscus shape. Thus, the intensified magnetic field shift the focus point of the extracted beam closer to the PG.

Figure 6.32 shows the beamlet axis profile line for the potential and positive ion density for the three cases. The comparison between the intensified filter field and the standard case shows no difference in neither the potential nor the positive ion distribution. In this way a variation in the magnetic field produces changes in the plasma distribution mainly for the negatively charged particles. For an intensified deflection field, the positive ion distribution does not present any significant variation from the standard case, apart from the meniscus being shifted closer to the source region. In the source region the positive ion distribution and the potential are the same as in the standard case.

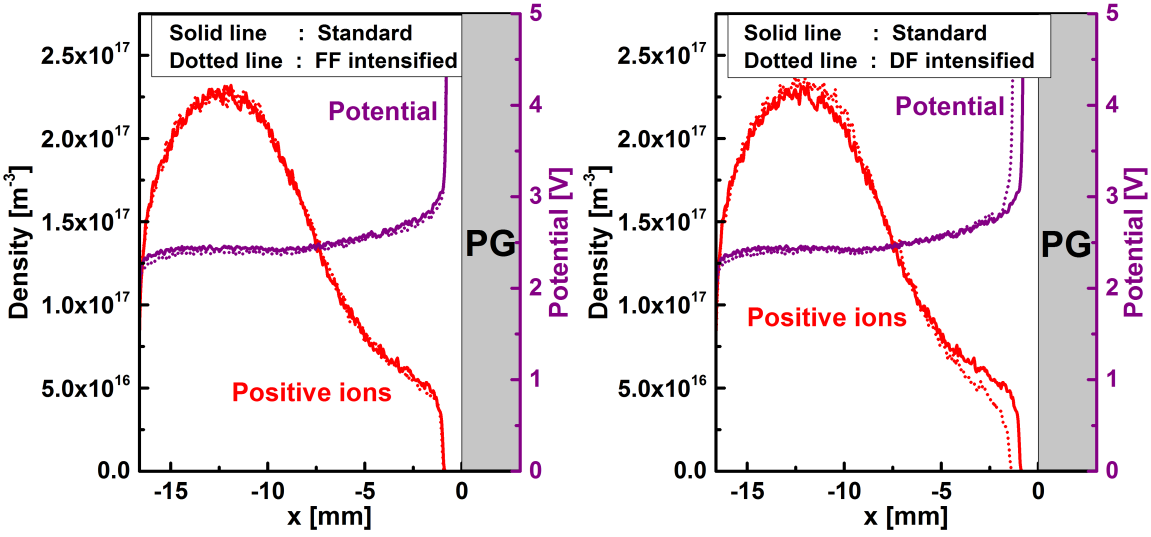

Figure 6.32: Left) Comparison of the positive ions and potential beamlet axis profiles between the standard magnetic field configuration and intensified filter field cases; Right) Comparison of the positive ions and potential beamlet axis profiles between the standard magnetic field configuration and intensified deflection field cases;

The values of the extracted ion current density and co-extracted electron current density, for the three magnetic field configurations, are detailed in the table 6.6. The extracted current density for an intensified FF and the standard case are the same at $j_{\mathrm{ex}} = 154\ \mathrm{Am}^{-2}$, having an electron ion ratio of $\frac{j_{\mathrm{e}}}{j_{\mathrm{ex}}} = 0.14$. The intensified DF decreases the extracted current density to $j_{\mathrm{ex}} = 145\ \mathrm{Am}^{-2}$. However, the electron-ion ratio is improved to $\frac{j_{\mathrm{e}}}{j_{\mathrm{ex}}} = 0.04$ for the intensified DF because of the strong reduction in the co-extracted electron current. The results from this simulations suggest that an increase in the deflection field should decrease the co-extracted electron current density at the test facilities. If the intensity of the magnets embedded in the EG cannot be increased due to technological limits, then the distance between the EG and the PG could be reduced. As the EG is moved closer to the PG the effect of the deflection field on the plasma becomes stronger. However, reducing the distance between grids requires a modification of the extraction potential in order to avoid an over-focused beam.

	Standard	**Intensified – FF**	**Intensified – DF**
$\mathbf{j}_{\mathrm{ex}}$ $[\mathbf{Am}^{-2}]$	154	154	145
$\mathbf{j}_{\mathrm{e}}$ $[\mathbf{Am}^{-2}]$	21.2	19.5	5.2
$\frac{\mathbf{j_e}}{\mathbf{j_{ex}}}$	0.14	0.14	0.04

Table 6.6: Extracted current details for the standard magnetic field configuration, the intensified magnetic filter field and the intensified magnetic deflection field.

Chapter 7

Summary

A neutral beam injection system will be used for heating and current drive in the ITER fusion experiment. Due to the energy requirement of 1 MeV (0.87 MeV) for the neutral deuterium (hydrogen) beam, the ITER neutral beam injection system will be based on the production, extraction and acceleration of negative ions. The development of the ITER neutral beam injection ion source brings new challenges as the inevitable co-extraction of electrons and the production of negative ions. The ITER source is required to full-fill an accelerated current of 40 A (46 A) in deuterium (hydrogen) for up to 3600 s.

The ITER neutral beam ion source is based on the design of the prototype RF-driven ion source at the BATMAN test facility. In this source a plasma is generated by inductive coupling. This source has 1 driver and is roughly 1/8 the size of the future ITER ion source. As part of the development road for the ITER ion source the ELISE test facility host an ion source with 4 drivers and half the size of the ITER ion source. To enhance the surface production of negative ions, Cs is evaporated into the ion sources in order to lower the surface work function.

The extraction of negative ions is done by a multi-aperture multi-grid system. A positive voltage difference between the plasma facing grid and the second grid is applied in order to extract negative ions. The extraction of negative ions is pulsed, consisting of 4 s of beam extraction in a 6-10 s plasma pulse at the BATMAN test facility, and 10 s of beam extraction every 150 s in a plasma pulse up to 3600 s at the ELISE test facility

A magnetic filter field is applied in order to reduce the electron density and temperature close to the plasma facing grid (PG) containing the extraction apertures. A low electron density and temperature reduces the negative ion losses by collisions with energetic electrons and the co-extracted electron current. The co-extracted electrons are deflected onto the second grid (EG) after extraction by a magnetic deflection

field, in order to avoid them being fully accelerated. A too high co-extracted electron current results in a heat load onto the EG above the technological capabilities of the cooling system. Thus, it is required for the ITER ion source that the ratio between the co-extracted electron current and the extracted ion current is below 1.

The different diagnostics installed in the test facilities have identified relations between the extracted current and the plasma parameters in the region downstream the magnetic filter field. The electron current density in front of the extraction apertures is found to be related to the co-extracted electron current density. It has also been measured that the co-extracted electron current is higher in deuterium, compared to hydrogen. Furthermore, a pronounced temporal increase of the co-extracted electron current takes places during the extraction of negative ions. In a similar way, the negative ion density in front of the extraction apertures is related to the extracted ion current density. The region in front of the extraction apertures where these relations have been found is denominated extraction region.

An understanding of the physics found in the extraction region is decisive to understand the ion beam extraction and formation process, as well as, the transport of the electrons before their extraction. In the extraction region a plasma sheath determines the transport of the surface produced negative ions into the plasma, and therefore enforce a limit in the extracted ion current density. The meniscus surface defining the interface between the plasma and the beam is formed through the extraction apertures. The meniscus shape influences the beam optics, as the initial velocity direction of the extracted particles is perpendicular to the meniscus surface. The shape of the meniscus is defined by the plasma conditions such as density and temperature in the extraction region. The electrons near the extraction apertures are magnetized, and therefore their transport is determined by the total magnetic field, composed by the filter and deflection field.

Measurements at the test facilities are limited to distances $\gtrsim$2 cm from the extraction apertures. However, the length scale of the plasma sheath and meniscus is that of the Debye length λ_D, which is typically around $\sim 2 \cdot 10^{-3}$ cm in the extraction region. Therefore, the diagnostics are unable to give a detailed insight over the extraction region physics. However, the experimental measurements taken $\sim$2 cm from the extraction aperture can be given as input to computational models, in order to complement the experimental data.

The ONIX code implements a 3D Particle In Cell method, allowing to model self-consistently the plasma in the extraction region. Its domain extends over the volume around one extraction aperture from $\sim$2 cm in the plasma to the start of the EG. It

has already been used for the simulation of the extraction of negative ions and study of the beam formation at the BATMAN test facility. The results showed to have predictive capabilities regarding the dependence of the maximum extracted current densities with the surface emission rate of negative ions. However, it was not used to make a deep study of the plasma dynamics in front of the extraction apertures, as the plasma physical model was not validated.

As first part of the present work a process of validation of ONIX for the plasma sheath physics and the surface emission was carried out. The validation was realized by comparison with analytical and validated computational models. The simulations were done in a reduced test domain in order to fulfill the same physical conditions of the reference models. The validation was done for an electron temperature range from 0.5 eV to 5 eV and a plasma density from 10^{14} m^{-3} to 10^{17} m^{-3}. These ranges are representative of the plasma parameters measured at the extraction region in the test facilitates.

An optimization of the numerical parameters set formed by the mesh size, time step and number of particles per cell was performed to reduce the calculation time. The optimal parameter set with $\Delta x = 1.5\ \lambda_D$, $\Delta t = 0.1\ \omega_{pe}^{-1}$ and an average of 30 particles per cell was identified to reproduce the plasma sheath physics, without adding relevant numerical perturbations and reducing the calculation time by 20% with respect to the numerical parameters usually suggested in the literature. A typical amount of 180 hours in 4096 cores is needed to make a simulation for one extraction aperture in the extraction region.

A series of parametric studies were done by applying the validated ONIX code to the BATMAN extraction aperture geometry. The aperture has a 8 mm diameter and a 45° chamfered geometry. An initial BATMAN standard simulation was done for comparison purposes. The initial conditions for the simulations used physical parameters measured for an hydrogen plasma at the test facility, corresponding to an electron temperature of 1 eV, a positive ion density $\sim 10^{17}$ m^{-3} and a proportion of electrons to negative ions 1:1. A surface negative ion emission rate of 550 Am^{-2} was implemented, as suggested by previous studies on the surface emission of negative ions in an ion source.

The standard case used an extraction voltage of 10 kV between the PG and EG, which is a typical value used during high performance operation at the test facility. At steady state the calculated extracted ion current density was 251 Am^{-2} and the co-extracted electron current density was 115 Am^{-2}, giving an electron-ion ratio of 0.46. The extracted ion current density is lower than the 329 Am^{-2}

extracted current density required for the ITER ion source. It was identified that the development of a potential well in front of the PG limited the amount of the negative ions going into the plasma, and therefore the extracted current density. Most of the negative ions forming the beam are directly extracted from the conical part of the extraction aperture. These ions generated an over-focused beam due to its initial preferential velocity direction perpendicular to the surface. The directly extracted negative ions are related to a deep penetration of the extraction potential into the plasma, increasing the penetration and curvature of the meniscus. The over-focused beam produced a divergent beam with a halo at the EG position. Ideally, the focus point of the beam should be at the entrance of the EG.

At the test facilities, a relation between the perveance and the beam divergence has been empirically seen. The perveance being defined by the ratio between the extracted current density and the extraction potential to the power of 1.5. The empirically seen relation between divergence and perveance was studied with ONIX, by analyzing an additional case with an extraction potential of 5 kV.

Reducing the extraction potential to 5 kV resulted in a less penetrating meniscus, producing a beam focused at the entrance of the EG. The extracted current density was reduced to 140 Am^{-2}, due to the lower extraction potential. The higher perveance and lower divergence, for the 5 kV extraction potential case with respect to the standard case, correspond to the behavior of the empirically seen under-perveance curve. ONIX allows then to explain the empirically seen relation. A high extraction potential penetrates deep into the plasma, increasing the curvature of the meniscus and the amount of directly extracted negative ions. A too high curvature of the meniscus acts then as a lens with a focal point in between the PG and EG, increasing the beam divergence at the EG. On the opposite, reducing the extraction potential decreases the penetration and curvature of the meniscus, shifting the beam focal point closer to the EG.

The co-extracted electron current density was reduced to 20 Am^{-2}, giving an electron-ion ratio of 0.14. The reduction of the co-extracted electron current was due the lower extraction potential and less penetrating meniscus. The less penetrating meniscus increased the distance in which the magnetic filter field reduces the electron density before they are extracted, and therefore the flux of electrons through the meniscus is reduced and so does the co-extracted electron current.

The penetration of the extraction potential does not only depend on the intensity of it, but also on the boundary conditions for the electrostatic potential, i.e. the geometry of the surfaces. To evaluate the influence of the aperture geometry on the

meniscus and extracted current, the extraction aperture geometry was changed from the conical to a flat extraction aperture.

In the flat geometry the extracted ion current density was reduced to 59 Am^{-2}. The reduction in the extracted current density was due to the decrease of the surface area for negative ion emission, and the reduction of the extraction probability. The chamfered geometry of the inner part of the extraction aperture was chosen to increase the extraction probability, as proven by previous Monte-Carlo simulations. Nonetheless, a less penetrating meniscus with respect to the standard case was achieved along with a beam with focal point at the EG.

In order to achieve a high extracted ion current density as in the standard case and to reduce the beam divergence, the extraction aperture geometry could be modified. The inner 45° chamfered part of the aperture can be kept to have the highest extraction probability and surface production area, while the downstream half could use a flat geometry to decrease the meniscus penetration.

Another parameter studied was the variation of the negative ion surface emission rate from the PG. The Cs deposited on the surface, to enhance the negative ion surface production, can be depleted over long pulses. The Cs depletion decreases the negative ion surface production due to the increase of the surface work function. It has been shown that the transport of Cs to the surface is done by the plasma. In the standard case it was noticed that the deep penetration of the meniscus reduces the reach of the plasma to the tips of the conical part of the extraction aperture.

In order to study the local variation of the negative ion production due to the local depletion of Cs, the negative ion emission from the conical surface was reduced to only the inner half of it. A decrease in the extracted current density to 112 Am^{-2} was obtained due to the reduction of emitting surface. The meniscus shape was modified in the region where the emission of negative ions was omitted. The meniscus penetration in the plasma was increased; as a result, the co-extracted electron current density increased to 217 Am^{-2}.

The experimentally seen higher co-extracted electron current and lower extracted current in a deuterium plasma was studied. As initial step the mass of the ions was modified (i.e. isotope effect). The results showed that the extracted current density is reduced by a factor 0.72 to 182 Am^{-2} in deuterium with respect to hydrogen. The reduction was found out to be due to a smaller ion flux through the meniscus, caused by a reduction in the thermal velocity by a factor $\frac{1}{\sqrt{2}} \sim 0.71$ due to the higher mass of deuterium. The co-extracted electron current increased to 147 Am^{-2}. The simulation showed that in a deuterium plasma electrons approaching the PG

confront a higher potential barrier compared to the hydrogen case. The potential barrier forbids electrons with a lower energy than it to reach the surface and be destroyed. Thus, a higher potential barrier increases the amount of electrons near the meniscus that can eventually be extracted. The results suggest that in order to reduce the co-extracted electron current the potential barrier should be reduced.

A simulation setting the extraction potential to 0 V was realized to analyze the difference between the plasma phase and extraction phase. The results showed that in the plasma phase, the plasma expands through the apertures as the extraction potential does not longer limit the global transport of the plasma. A high decrease in the ion and electron density was seen in the region between the PG and EG. The gradient being caused by the higher intensity of the deflection field in this region, which magnetize the plasma and reduced their diffusion. The expansion of the plasma showed a reduction of the electron and ion density in the region ∼2 cm from the PG, where usually measurements are realized. Besides, the potential in the plasma was reduced by 0.8 V due to the magnetic deflection field already reducing the electron flow onto the PG, and therefore requiring a lower plasma potential in order to equate the flow of electron and ions onto this surface.

A series of simulations were done for the extraction aperture geometry of the ELISE test facility. It has chamfered apertures with a diameter of 14 mm. The simulations focused in the effect of the magnetic field on the transport of electrons and the co-extracted electron current. An initial standard case was studied using the magnetic filter field generated by a current trough the PG of 2.5 kA, corresponding to a magnetic field of ∼2.0 mT. The deflection magnetic field generated by permanent magnets was also included.

The results of the simulation showed that the magnetized electrons follow the structure of the magnetic field. The magnetic filter field and magnetic deflection field have different structures and are dominant on different directions. Thus, the electron density distribution presented a 3D distribution. A drift velocity generated by the magnetic field curvature and gradient was identified. The 3D topology of the magnetic field showed to cause a non-homogeneous electron flow onto the PG. The magnetic deflection field lines directed the flow of electrons onto the PG surface, while the magnetic filter field limited the flow of electrons onto the PG. As a product of the variation of the electron flow onto the PG, the potential well was shown to vary along the PG plane, being deeper in the regions where the filter field is dominant (electron flow reduced).

The intensity of each source component of the magnetic field was increased to study their effect on the co-extracted electron current density. Three cases were compared: standard ELISE case, magnetic filter field intensity increased by a factor 2 and magnetic deflection field intensity increased by a factor 2. A total co-extracted electron current density of 21.2 Am^{-2} was registered for the standard case, 21.2 Am^{-2} for the intensified filter field and 5.2 Am^{-2} for the intensified deflection field. The extracted ion current density was 154 Am^{-2} for the standard and intensified case, while a reduced 145 Am^{-2} extracted ion current density was obtained in the intensified deflection field case.

The magnetic filter field produces changes in the plasma composition at a much larger scale, and the used domain only accounted that of one aperture fixing the plasma composition, and therefore reducing the more global effect of the filter field. An intensified deflection field showed a slight decrease of the extracted current density and a high reduction of the co-extracted electron current density, reducing the electron-ion ratio respect to the other two cases by a factor 3. The results from these simulations suggest that a more intense deflection field is an option to decrease the co-extracted electron current. However, the intensity of the permanent magnets producing the deflection field is technologically limited. An option to increase the intensity of the deflection field in the plasma is to move the EG closer to the PG. Nonetheless, if the EG is shifted the extraction potential has to be reduced as to avoid a deep penetration of the meniscus.

The simulations results done by the validated ONIX code identified key parameter that can lead to develop new concepts and techniques to decrease the beam divergence and reduce the co-extracted electron current. As continuation from the presented research, a series of simulations varying the extraction aperture geometry and extraction potential can help to identify an optimum geometry and extraction potential, for which the extracted ion current density is maximized and the beam divergence minimized. A series of simulations with different topologies of the magnetic field can be explored in order to reduce the co-extracted electron current, and afterwards implement the modifications at the test facilities. In order to improve the analysis of the effect of the magnetic field a domain including two extraction apertures should be explored. The increasing availability of computational resources at high performance computing systems suggests that the extension of the domain to two extraction apertures would be possible in the near future.

Appendix A

ONIX-IBSimu connection

At the test facilities, the divergence of the whole beam is measured at ∼2 m after the grounded grid. Thus, the divergence calculated by ONIX for a single beamlet between the PG and EG cannot be compared to that measured experimentally, as the acceleration stage between the EG and the GG produces electrostatic lenses that influence the beam optics. An increase in the simulation domain in ONIX is not feasible due to the increase in calculation time that it implies. Therefore, a plausible option is to connect ONIX with a particle tracking code. A particle tracking code models a beamlet considering all the grids in the acceleration phase and has the capability to reproduce the whole beam by the superposition of several beamlets.

A well developed particle tracking code including all the necessary features to model a beam in the acceleration phase is IBSimu [98]. IBSimu uses as input the initial particle distribution of the extracted particles and the magnetic field; the electrostatic field is then obtained from the distribution of the extracted particles and an analytical model for the space charge compensation.

In order to connect ONIX with IBSimu, information such as position, velocity and species of the particles composing the beam has to be given to IBSimu as input. The information is given at a certain plane perpendicular to the beam direction. The codes are connected in the plane located at the beginning of the EG, end of the ONIX domain. In this way the plasma and extracted beam formation are modeled by ONIX and IBSimu models the beam transport. However, the electrostatic potential should be the same in both codes at the plane of connection.

The boundary condition in ONIX at the EG plane was modified in order to have the same electrostatic potential as IBSimu. The potential at the EG of the vacuum solution given by IBSimu, including the EG aperture and the GG, was given to ONIX as boundary condition at the EG.

Figure A.1 shows the vacuum potential in the ONIX domain using the planar EG and the IBSimu generated boundary condition. The effect of the aperture is noticeable close the EG. The potential isolines are almost parallel using the planar EG, while the optical lenses generated by the aperture in the EG are noticeable with the IBSimu conditions. However, the potential difference between the two cases shows that the effect is negligible in the plasma side (left to the PG). In this way we ensure that simulations done with the planar EG properly represent the plasma.

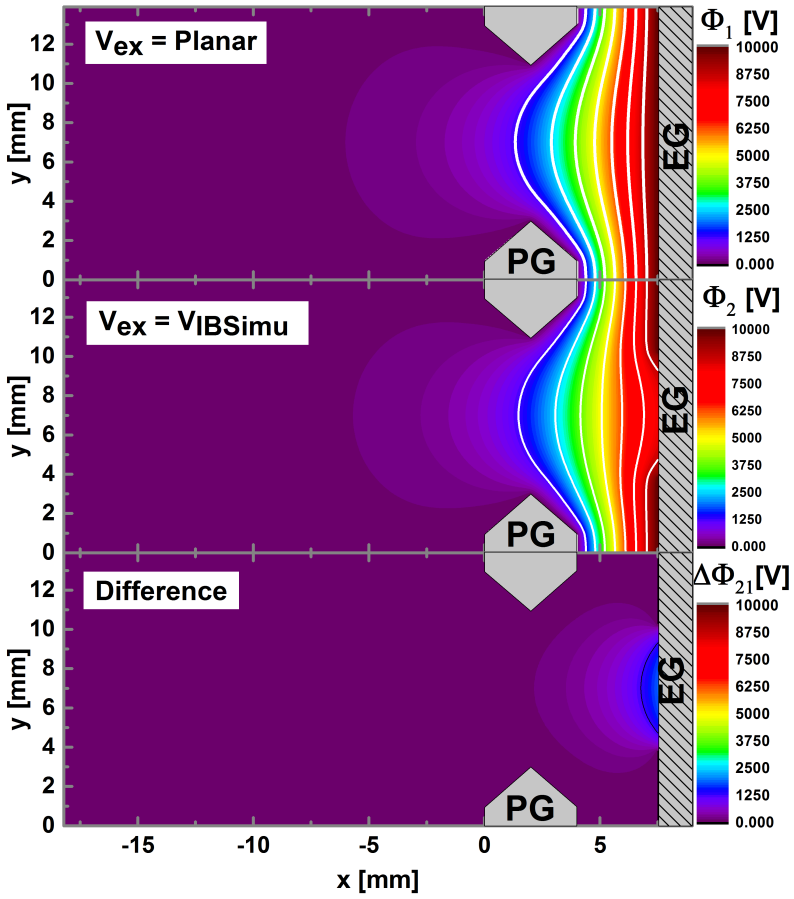

Figure A.1: Vacuum electrostatic potential in the BATMAN extraction aperture geometry using the planar EG boundary condition, the IBSimu boundary conditions and the difference between the two cases.

An evaluation of the effect of the new boundary conditions was done for the standard BATMAN case. Figure A.2 shows the negative ion density map for the two cases. The meniscus positions is unchanged meaning that the plasma interaction with the extraction voltage is similar if not the same. A comparison of the potential lines, marked by the white curves in the figure A.2, shows that a change in the beam is going to be produced by the curvature of the potential lines. The electrostatic lenses

close to the EG are defocussing, meaning they accelerate the beam in the direction perpendicular to the beam (y and z). This defocussing is usually intended to avoid the beam expansion due to a high charge accumulation over one point. The electrostatic lenses then change the beam divergence close to the EG, and therefore it is essential to include the aperture effect in ONIX for its connection to IBSimu.

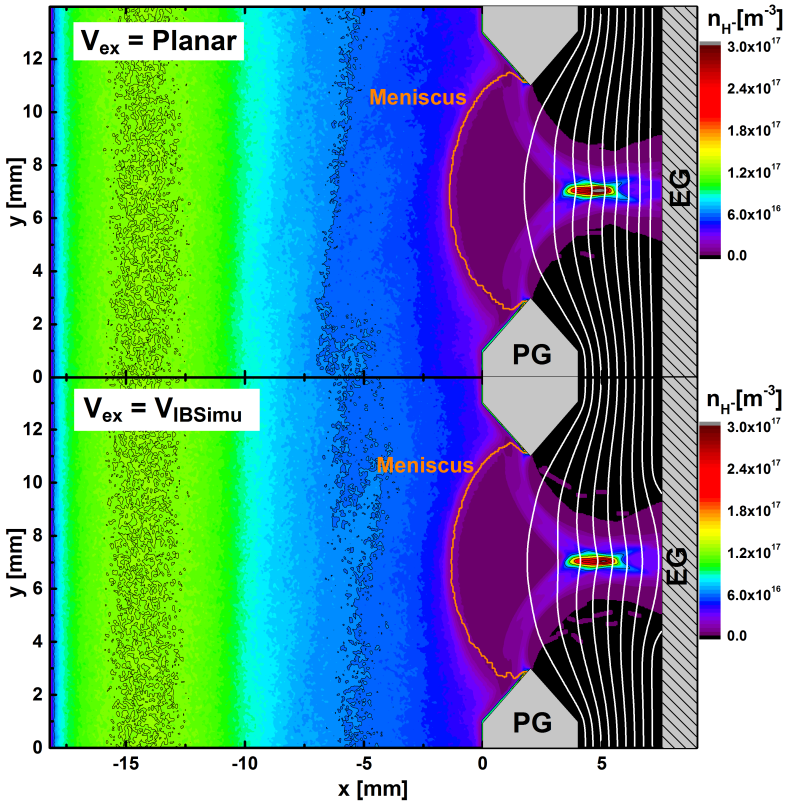

Figure A.2: Negative ion density for planar EG and IBSimu boundary conditions. The meniscus shape is marked by the orange curve, and the electrostatic field lines are marked in white.

Appendix B

Magnetic field input

B.1 BATMAN

At the BATMAN test facility the magnetic filter field is generated by permanent magnets around the expansion chamber and the magnetic deflection field is generated by permanent magnets embedded in the EG. The total magnetic field for one extraction aperture was calculated by [99] using the PerMag [74] code. Figures B.1 and B.2 show the total magnetic field components in the xy and xz middle planes.

B.2 ELISE

At the ELISE test facility the magnetic filter field is generated by a current flowing through the PG. The deflection field is generated by permanent magnets embedded in the EG. The deflection field was calculated by [99] using the PerMag code [74] and the magnetic filter field was taken from [75], calculated using the commercial software ANSYS. Figures B.3 and B.4 show the components of the total magnetic field in the xy and xz middle planes.

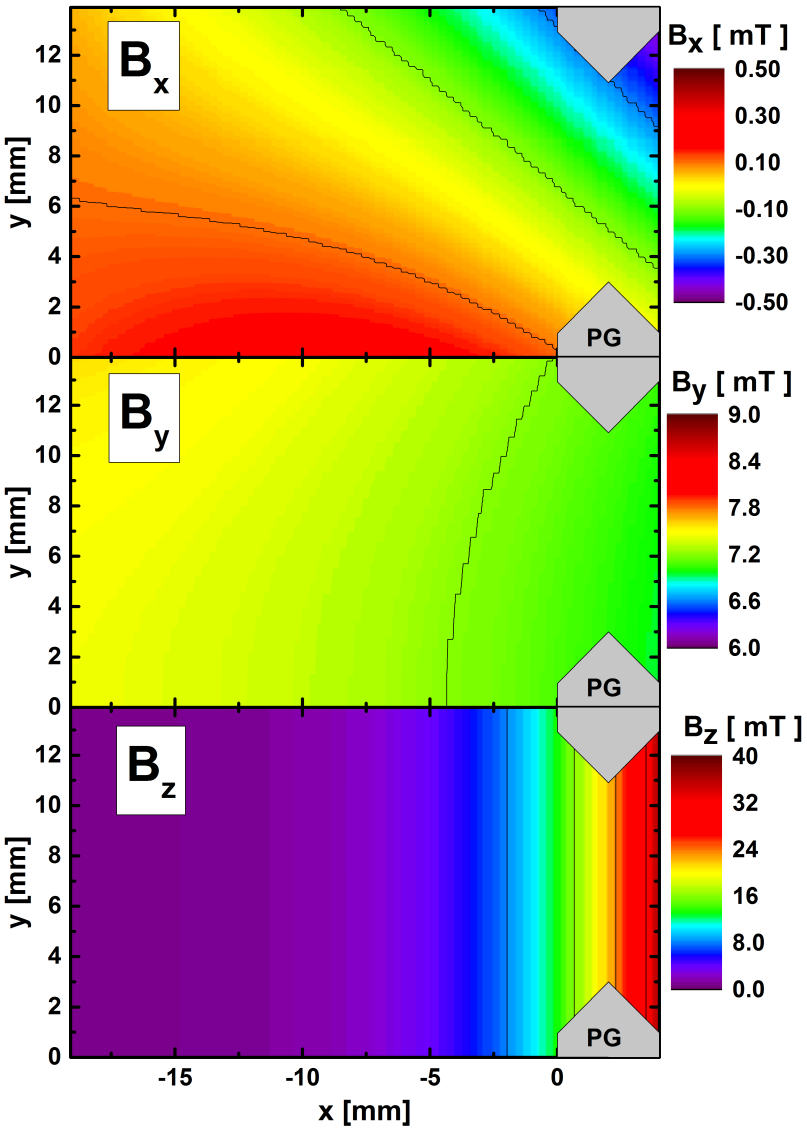

Figure B.1: BATMAN magnetic field components for the one aperture domain in the xy middle plane.

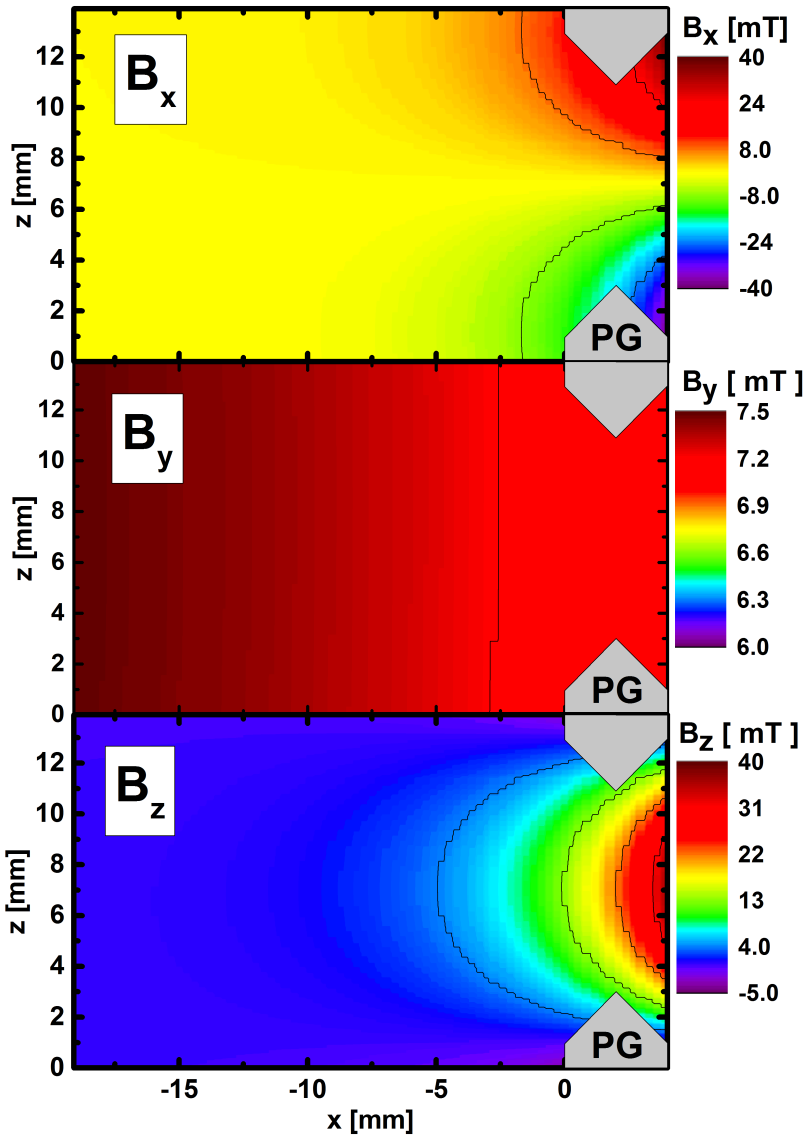

Figure B.2: BATMAN magnetic field components for the one aperture domain in the xz middle plane.

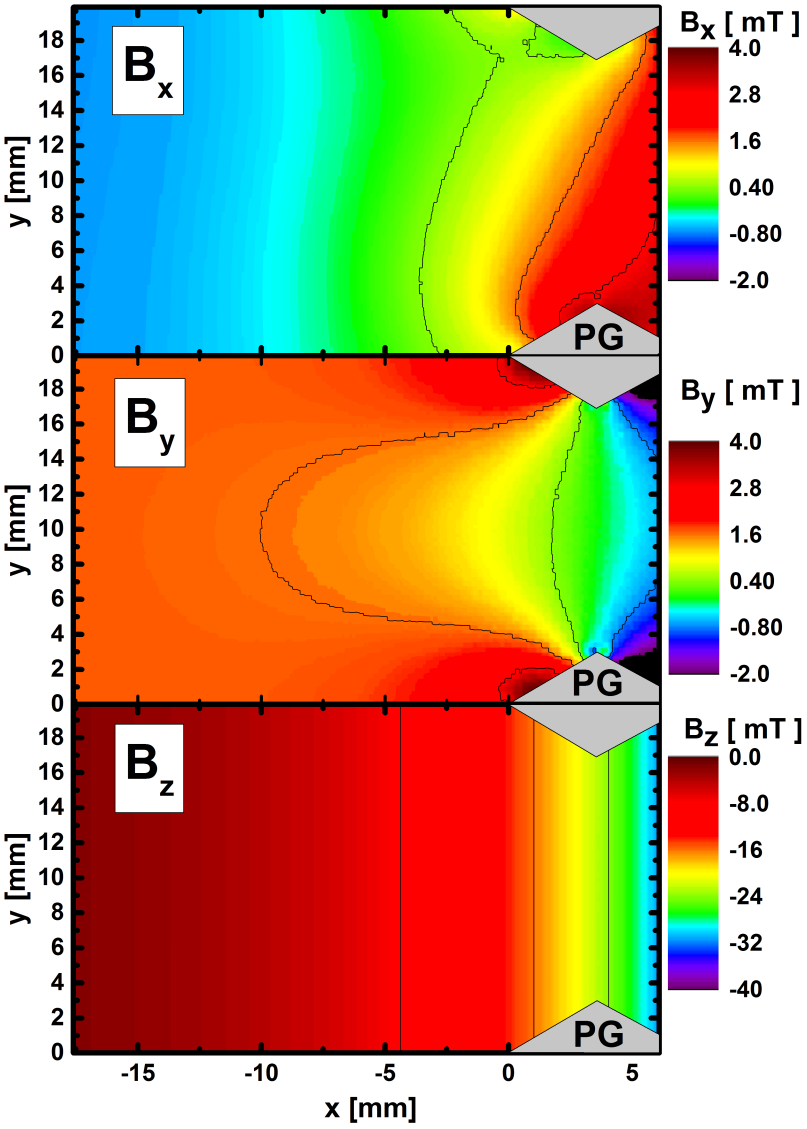

Figure B.3: ELISE magnetic field components for the one aperture domain in the xy middle plane.

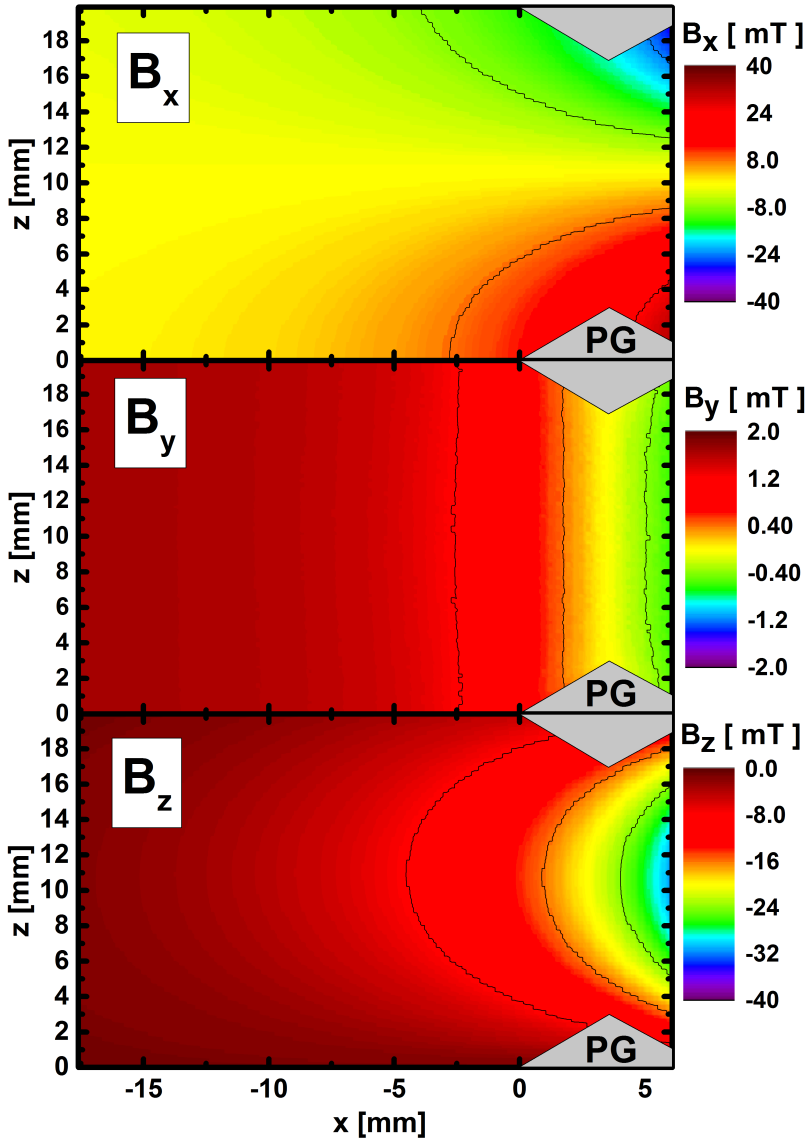

Figure B.4: ELISE magnetic field components for the one aperture domain in the xz middle plane.

Bibliography

[1] J. P. Freidberg, *Plasma Physics and Fusion Energy.* Cambridge: Cambridge University Press, 2007.

[2] P. Kaw and I. Bandyopadhyay, *The case for fusion.* Vienna, Austria: IAEA, 2012.

[3] R. Aymar, P. Barabaschi, and Y. Shimomura, "The ITER design," *Plasma Physics and Controlled Fusion*, vol. 44, no. 5, p. 519, 2002.

[4] ITER Organization, "ITER research plan within the staged approach," Tech. Rep. ITR-18-003, 2018.

[5] J. Jacquinot, F. Albajar, B. Beaumont, A. Becoulet, T. Bonicelli, D. Bora, D. Campbell, A. Chakraborty, C. Darbos, H. Decamps, G. Denisov, R. Goulding, J. Graceffa, T. Gassmann, R. Hemsworth, M. Henderson, G. Hoang, T. Inoue, N. Kobayashi, P. Lamalle, A. Mukherjee, M. Nightingale, D. Rasmussen, S. Rao, G. Saibene, K. Sakamoto, R. Sartori, B. Schunke, P. Sonato, D. Swain, K. Takahashi, M. Tanaka, A. Tanga, and K. Watanabe, "Progress on the heating and current drive systems for ITER," *Fusion Engineering and Design*, vol. 84, no. 2, p. 125, 2009.

[6] B. Geiger, M. Weiland, A. Jacobsen, D. Rittich, R. Dux, R. Fischer, C. Hopf, M. Maraschek, R. McDermott, S. Nielsen, T. Odstrcil, M. Reich, F. Ryter, M. Salewski, P. Schneider, and G. Tardini, "Fast-ion transport and neutral beam current drive in ASDEX Upgrade," *Nuclear Fusion*, vol. 55, no. 8, p. 083001, 2015.

[7] R. S. Hemsworth, D. Boilson, P. Blatchford, M. Dalla Palma, G. Chitarin, H. P. L. de Esch, F. Geli, M. Dremel, J. Graceffa, D. Marcuzzi, G. Serianni, D. Shah, M. Singh, M. Urbani, and P. Zaccaria, "Overview of the design of the ITER heating neutral beam injectors," *New Journal of Physics*, vol. 19, no. 2, p. 025005, 2017.

[8] A. Kojima, M. Hanada, Y. Tanaka, M. Kawai, N. Akino, M. Kazawa, M. Komata, K. Mogaki, K. Usui, S. Sasaki, K. Kikuchi, N. Seki, S. Nemoto, K. Oshima, T. Simizu, N. Kubo, K. Oasa, T. Inoue, K. Watanabe, M. Taniguchi, M. Kashiwagi, H. Tobari, N. Umeda, S. Kobayashi, Y. Yamano, and L. Grisham, "Achievement of 500 keV negative ion beam acceleration on JT-60U negative-ion-based neutral beam injector," *Nuclear Fusion*, vol. 51, no. 8, p. 083049, 2011.

[9] N. Umeda, J. Hiratsuka, A. Kojima, M. Ichikawa, M. Yoshida, H. Yamanaka, H. Tobari, K. Watanabe, and M. Kashiwagi, "Long pulse and high power density H^- ion beam acceleration for ITER," *AIP Conference Proceedings*, vol. 1869, no. 1, p. 030008, 2017.

[10] W. Cooper and R. Pyle, "The National Negative-Ion-Based Neutral-Beam Development Plan," tech. rep., The Lawrence Berkeley Laboratory and The Office of Fusion Energy of The U.S. Department of Energy, 1983.

[11] A. Krylov and R. Hemsworth, "Gas flow and related beam losses in the ITER neutral beam injector," *Fusion Engineering and Design*, vol. 81, no. 19, p. 2239, 2006.

[12] K. Berkner, R. Pyle, and J. Stearns, "Intense, mixed-energy hydrogen beams for CTR injection," *Nuclear Fusion*, vol. 15, no. 2, p. 249, 1975.

[13] L. R. Grisham, "The operational phase of negative ion beam systems on JT-60U and LHD," *IEEE Transactions on Plasma Science*, vol. 33, no. 6, p. 1814, 2005.

[14] A. Masiello, G. Agarici, T. Bonicelli, M. Simon, J. Alonso, M. Bigi, D. Boilson, G. Chitarin, C. Day, P. Franzen, S. Hanke, B. Heinemann, R. Hemsworth, A. Luchetta, D. Marcuzzi, J. Milnes, T. Minea, R. Pasqualotto, N. Pomaro, G. Serianni, W. Rigato, P. Sonato, V. Toigo, F.Villecroze, C. Waldon, and P. Zaccaria, "The European contribution to the development of the ITER NB injector," *Fusion Engineering and Design*, vol. 86, no. 6, p. 860, 2011. Proceedings of the 26th Symposium of Fusion Technology (SOFT-26).

[15] R. Hemsworth, H. Decamps, J. Graceffa, B. Schunke, M. Tanaka, M. Dremel, A. Tanga, H. D. Esch, F. Geli, J. Milnes, T. Inoue, D. Marcuzzi, P. Sonato, and P. Zaccaria, "Status of the ITER heating neutral beam system," *Nuclear Fusion*, vol. 49, no. 4, p. 045006, 2009.

[16] B. Heinemann, U. Fantz, W. Kraus, L. Schiesko, C. Wimmer, D. Wünderlich, F. Bonomo, M. Fröschle, R. Nocentini, and R. Riedl, "Towards large and powerful radio frequency driven negative ion sources for fusion," *New Journal of Physics*, vol. 19, no. 1, p. 015001, 2017.

[17] P. McNeely, M. Barlak, J. Baldzuhn, S. Bozhenkov, M. Drevlak, G. Gawlik, B. Heinemann, D. Holtum, J. Jagielski, R. Kairys, R. Nocentini, R. Riedl, P. Rong, N. Rust, R. Schroeder, E. Speth, A. Stbler, A. Turos, and R. Wolf, "Current status of the neutral beam heating system of W7-X," *Fusion Engineering and Design*, vol. 88, no. 6, p. 1034, 2013.

[18] N. Angert, "Ion sources," in *CAS CERN accelerator school: 5 general accelerator physics course* (S. Turner, ed.), vol. 2, p. 619, European Organization for Nuclear Research (CERN), 1994.

[19] M. Bacal and M. Wada, "Negative hydrogen ion production mechanisms," *Applied Physics Reviews*, vol. 2, no. 2, p. 021305, 2015.

[20] J. N. Bardsley and J. M. Wadehra, "Dissociative attachment and vibrational excitation in low-energy collisions of electrons with H_2 and D_2," *Phys. Rev. A*, vol. 20, p. 1398, 1979.

[21] A. J. T. Holmes, "Electron flow through transverse magnetic fields in magnetic multipole arc discharges," *Review of Scientific Instruments*, vol. 53, no. 10, p. 1517, 1982.

[22] A. R. P. Rau, "The negative ion of hydrogen," *Journal of Astrophysics and Astronomy*, vol. 17, no. 3, p. 113, 1996.

[23] H. B. Michaelson, "The work function of the elements and its periodicity," *Journal of Applied Physics*, vol. 48, no. 11, p. 4729, 1977.

[24] W. Haynes, *CRC Handbook of Chemistry and Physics, 93rd Edition*. Taylor & Francis, 2012.

[25] G. Alton, "Semi-empimcal mathematical relationships for electropositive adsorbate induced work function changes," *Surface Science*, vol. 175, no. 1, p. 226, 1986.

[26] C. Wimmer, L. Schiesko, and U. Fantz, "Investigation of the boundary layer during the transition from volume to surface dominated H^- production at the BATMAN test facility," *Review of Scientific Instruments*, vol. 87, no. 2, p. 02B310, 2016.

[27] J. Horáček, M. Čížek, K. Houfek, P. Kolorenč, and W. Domcke, "Dissociative electron attachment and vibrational excitation of h_2 by low-energy electrons: Calculations based on an improved nonlocal resonance model," *Phys. Rev. A*, vol. 70, p. 052712, 2004.

[28] R. K. Janev, W. D. Langer, D. E. Post, and K. Evans, *Elementary processes in hydrogen-helium plasmas*. Springer Berlin Heidelberg, 1987.

[29] E. Speth, H. D. Falter, P. Franzen, U. Fantz, M. Bandyopadhyay, S. Christ, A. Encheva, M. Fröschle, D. Holtum, B. Heinemann, W. Kraus, A. Lorenz, C. Martens, P. McNeely, S. Obermayer, R. Riedl, R. Süss, A. Tanga, R. Wilhelm, and D. Wünderlich, "Overview of the RF source development programme at IPP Garching," *Nuclear Fusion*, vol. 46, p. S220, 2006.

[30] P. Franzen, H. D. Falter, U. Fantz, W. Kraus, M. Berger, S. Christ-Koch, M. Fröschle, R. Gutser, B. Heinemann, S. Hilbert, S. Leyer, C. Martens, P. McNeely, R. Riedl, E. Speth, and D. Wünderlich, "Progress of the development of the IPP RF negative ion source for the ITER neutral beam system," *Nuclear Fusion*, vol. 47, no. 4, p. 264, 2007.

[31] U. Fantz, C. Hopf, D. Wnderlich, R. Friedl, M. Frschle, B. Heinemann, W. Kraus, U. Kurutz, R. Riedl, R. Nocentini, and L. Schiesko, "Towards powerful negative ion beams at the test facility ELISE for the ITER and DEMO NBI systems," *Nuclear Fusion*, vol. 57, no. 11, p. 116007, 2017.

[32] U. Fantz, P. Franzen, W. Kraus, L. Schiesko, C. Wimmer, and D. Wnderlich, "Size scaling of negative hydrogen ion sources for fusion," *AIP Conference Proceedings*, vol. 1655, no. 1, p. 040001, 2015.

[33] P. McNeely, S. V. Dudin, S. Christ-Koch, and U. Fantz, "A Langmuir probe system for high power RF-driven negative ion sources on high potential," *Plasma Sources Science and Technology*, vol. 18, no. 1, p. 014011, 2008.

[34] R. Gutser, D. Wünderlich, and U. F. and, "Negative hydrogen ion transport in RF-driven ion sources for ITER NBI," *Plasma Physics and Controlled Fusion*, vol. 51, no. 4, p. 045005, 2009.

[35] R. Nocentini, R. Gutser, B. Heinemann, M. Frschle, and R. Riedl, "Optimization of the cooling circuit and thermo-mechanical analysis for the extraction grid of ELISE," *Fusion Engineering and Design*, vol. 86, no. 6, p. 916, 2011. Proceedings of the 26th Symposium of Fusion Technology (SOFT-26).

[36] B. Heinemann, H. Falter, U. Fantz, P. Franzen, M. Fröschle, R. Gutser, W. Kraus, R. Nocentini, R. Riedl, E. Speth, A. Stäbler, D. Wünderlich, P. Agostinetti, and T. Jiang, "Design of the half-size ITER neutral beam source for the test facility ELISE," *Fusion Engineering and Design*, vol. 84, no. 2, p. 915, 2009. Proceeding of the 25th Symposium on Fusion Technology.

[37] J. D. Isenberg, H. J. Kwon, and M. Seidl, "Surface production of H^- ions by backscattering of H^+ and H_2^+ ions in the 3-50 eV ion energy range," *AIP Conference Proceedings*, vol. 287, no. 1, p. 38, 1992.

[38] R. J. Goldston and P. H. Rutherford, *Introduction to plasma physics*. London: IOP Publishing Ltd, 1995.

[39] F. F. Chen, *Introduction to Plasma Physics and Controlled Fusion*. US: Springer, 3 ed., 1984.

[40] I. Adamovich, S. D. Baalrud, A. Bogaerts, P. J. Bruggeman, M. Cappelli, V. Colombo, U. Czarnetzki, U. Ebert, J. G. Eden, P. Favia, D. B. Graves, S. Hamaguchi, G. Hieftje, M. Hori, I. D. Kaganovich, U. Kortshagen, M. J. Kushner, N. J. Mason, S. Mazouffre, S. M. Thagard, H. R. Metelmann, A. Mizuno, E. Moreau, A. B. Murphy, B. A. Niemira, G. S. Oehrlein, Z. L. Petrovic, L. C. Pitchford, Y. K. Pu, S. Rauf, O. Sakai, S. Samukawa, S. Starikovskaia, J. Tennyson, K. Terashima, M. M. Turner, M. C. M. van de Sanden, and A. Vardelle, "The 2017 plasma roadmap: Low temperature plasma science and technology," *Journal of Physics D: Applied Physics*, vol. 50, no. 32, p. 323001, 2017.

[41] D. Wünderlich, S. Mochalskyy, I. M. Montellano, and A. Revel, "Review of particle-in-cell modeling for the extraction region of large negative hydrogen ion sources for fusion," *Review of Scientific Instruments*, vol. 89, no. 5, p. 052001, 2018.

[42] D. Bohm, "Minimum ionic kinetic energy for a stable sheath," *The Characteristics of Electrical Discharges in Magnetic Fields*, p. 77, 1949.

[43] P. C. Stangeby, "Plasma sheath transmission factors for tokamak edge plasmas," *The Physics of Fluids*, vol. 27, no. 3, p. 682, 1984.

[44] D. Wünderlich, R. Gutser, and U. Fantz, "PIC code for the plasma sheath in large caesiated RF sources for negative hydrogen ions," *Plasma Sources Science and Technology*, vol. 18, no. 4, p. 045031, 2009.

[45] R. McAdams, A. J. T. Holmes, D. B. King, and E. Surrey, "Transport of negative ions across a double sheath with a virtual cathode," *Plasma Sources Science and Technology*, vol. 20, no. 3, p. 035023, 2011.

[46] C. D. Child, "Discharge from hot CaO," *Phys. Rev. (Series I)*, vol. 32, p. 492, 1911.

[47] R. Maurizio, U. Fantz, F. Bonomo, and G. Serianni, "Characterisation of the properties of a negative hydrogen ion beam by several beam diagnostic techniques," *Nuclear Fusion*, vol. 56, no. 6, p. 066012, 2016.

[48] C. K. Birdsall and A. B. Langdon, *Plasma Physics via Computer Simulation*. Bristol, England: IOP Publishing Ltd, 1 ed., 1991.

[49] C. K. Birdsall, "Particle-in-cell charged-particle simulations, plus Monte Carlo collisions with neutral atoms, PIC-MCC," *IEEE Transactions on Plasma Science*, vol. 19, no. 2, p. 65, 1991.

[50] T. Takizuka and H. Abe, "A binary collision model for plasma simulation with a particle code," *Journal of Computational Physics*, vol. 25, no. 3, p. 205, 1977.

[51] L. Spitzer, *Physics of Fully Ionized Gases*. New York: Dover Publications Inc, 2 ed., 1962.

[52] H. Okuda, "Nonphysical noises and instabilities in plasma simulation due to a spatial grid," *Journal of Computational Physics*, vol. 10, no. 3, p. 475, 1972.

[53] R. Courant, K. Friedrichs, and H. Lewy, "Über die partiellen Differenzengleichungen der mathematischen Physik," *Mathematische Annalen*, vol. 100, no. 1, p. 32, 1928.

[54] F. Taccogna, S. Longo, M. Capitelli, and R. Schneider, "Negative-Ion-Source Modeling: From Expansion to Extraction Region," *IEEE Transactions on Plasma Science*, vol. 36, no. 4, p. 1589, 2008.

[55] T. Sakurabayashi, A. Hatayama, and M. Bacal, "Effects of a weak transverse magnetic field on negative ion transport in negative ion sources," *Journal of Applied Physics*, vol. 95, no. 8, p. 3937, 2004.

[56] M. Turek, J. Sielanko, P. Franzen, and E. Speth, "Influence of transversal magnetic field on negative ion extraction process in 3D computer simulation of the multiaperture ion source," *AIP Conference Proceedings*, vol. 812, no. 1, p. 153, 2006.

[57] M. Turek and J. Sielanko, "Simulations of negative ion extraction from a multiaperture ion source in the presence of the magnetic filter," *Vacuum*, vol. 83, p. S256, 2009.

[58] K. Miyamoto, S. Okuda, and A. Hatayama, "Meniscus and beam halo formation in a tandem-type negative ion source with surface production," *Applied Physics Letters*, vol. 100, no. 23, p. 233507, 2012.

[59] K. Miyamoto, S. Okuda, A. Hatayama, M. Hanada, and A. Kojima, "Study of beam optics and beam halo by integrated modeling of negative ion beams from plasma meniscus formation to beam acceleration," *Applied Physics Letters*, vol. 102, no. 2, p. 023512, 2013.

[60] F. Taccogna and P. Minelli, "PIC modeling of negative ion sources for fusion," *New Journal of Physics*, vol. 19, no. 1, p. 015012, 2017.

[61] J. P. Boeuf, G. Fubiani, and L. Garrigues, "Issues in the understanding of negative ion extraction for fusion," *Plasma Sources Science and Technology*, vol. 25, no. 4, p. 045010, 2016.

[62] S. Nishioka, I. Goto, K. Miyamoto, A. Hatayama, and A. Fukano, "Study of ion-ion plasma formation in negative ion sources by a three-dimensional in real space and three-dimensional in velocity space particle in cell model," *Journal of Applied Physics*, vol. 119, no. 2, p. 023302, 2016.

[63] S. Nishioka, K. Miyamoto, S. Okuda, I. Goto, A. Hatayama, and A. Fukano, "Study of plasma meniscus and beam halo in negative ion sources using three

dimension in real space and three dimension in velocity space particle in cell model," *Review of Scientific Instruments*, vol. 85, no. 2, p. 02A737, 2014.

[64] K. Miyamoto, S. Nishioka, I. Goto, A. Hatayama, M. Hanada, A. Kojima, and J. Hiratsuka, "Analysis of the beam halo in negative ion sources by using 3D3V PIC code," *Review of Scientific Instruments*, vol. 87, no. 2, p. 02B124, 2016.

[65] F. Taccogna, P. Minelli, M. Cavenago, P. Veltri, and N. Ippolito, "The characterization and optimization of NIO1 ion source extraction aperture using a 3D particle-in-cell code," *Review of Scientific Instruments*, vol. 87, no. 2, p. 02B145, 2016.

[66] M. Cavenago, G. Serianni, M. De Muri, P. Agostinetti, V. Antoni, C. Baltador, M. Barbisan, L. Baseggio, M. Bigi, V. Cervaro, F. Degli Agostini, E. Fagotti, T. Kulevoy, N. Ippolito, B. Laterza, A. Minarello, M. Maniero, R. Pasqualotto, S. Petrenko, M. Poggi, D. Ravarotto, M. Recchia, E. Sartori, M. Sattin, P. Sonato, F. Taccogna, V. Variale, P. Veltri, B. Zaniol, L. Zanotto, and S. Zucchetti, "First experiments with the negative ion source NIO1," *Review of Scientific Instruments*, vol. 87, no. 2, p. 02B320, 2016.

[67] M. Cavenago, T. Kulevoy, S. Petrenko, G. Serianni, V. Antoni, M. Bigi, F. Fellin, M. Recchia, and P. Veltri, "Development of a versatile multiaperture negative ion source," *Review of Scientific Instruments*, vol. 83, no. 2, p. 02A707, 2012.

[68] G. Fubiani, L. Garrigues, G. Hagelaar, N. Kohen, and J. P. Boeuf, "Modeling of plasma transport and negative ion extraction in a magnetized radio-frequency plasma source," *New Journal of Physics*, vol. 19, no. 1, p. 015002, 2017.

[69] S. Mochalskyy, *Modeling of the negative ion extraction from a hydrogen plasma source : application to ITER neutral beam injector*. Doctoral thesis, Université Paris Sud - Paris XI, 2011.

[70] A. Revel, S. Mochalskyy, I. M. Montellano, D. Wünderlich, U. Fantz, and T. Minea, "Massive parallel 3D PIC simulation of negative ion extraction," *Journal of Applied Physics*, vol. 122, no. 10, p. 103302, 2017.

[71] S. Mochalskyy, U. Fantz, D. Wünderlich, and T. Minea, "Comparison of ONIX simulation results with experimental data from the BATMAN testbed for the study of negative ion extraction," *Nuclear Fusion*, vol. 56, no. 10, p. 106025, 2016.

[72] S. Mochalskyy, J. Lettry, and T. Minea, "Beam formation in CERNs cesiated surfaces and volume H^- ion sources," *New Journal of Physics*, vol. 18, no. 8, p. 085011, 2016.

[73] A. Revel, S. Mochalskyy, D. Wünderlich, U. Fantz, and T. Minea, "ONIX results: Comparison of grid geometry (BATMAN - ELISE - flat grid)," *AIP Conference Proceedings*, vol. 1869, no. 1, p. 020004, 2017.

[74] D. Ciric, "PerMag Manual (Abington:UKAEA Fusion/Euratom Association, Culham Science Centre)," *private communication*, 2007.

[75] R. Nocentini, R. Gutser, B. Heinemann, M. Froeschle, and R. Riedl, "Plasma grid design for optimized filter field configuration for the NBI test facility ELISE," *Fusion Engineering and Design*, vol. 84, no. 12, p. 2131, 2009.

[76] R. K. Janev, W. D. Langer, E. Douglass Jr, *et al.*, *Elementary processes in hydrogen-helium plasmas: cross sections and reaction rate coefficients*, vol. 4. Springer Science & Business Media, 2012.

[77] R. Celiberto, R. Janev, A. Laricchiuta, M. Capitelli, J. Wadehra, and D. Atems, "Cross section data for electron-impact inelastic processes of vibrationally excited molecules of hydrogen and its isotopes," *Atomic Data and Nuclear Data Tables*, vol. 77, no. 2, p. 161, 2001.

[78] P. McNeely, D. Wünderlich, and the NNBI Team, "Neutral depletion in an H-source operated at high RF power and low input gas flow," *Plasma Sources Science and Technology*, vol. 20, no. 4, p. 045005, 2011.

[79] IAEA Nuclear Data Section A+M Data Unit, "Atomic and molecular data."

[80] G. Fubiani and J. P. Boeuf, "Role of positive ions on the surface production of negative ions in a fusion plasma reactor type negative ion source-Insights from a three dimensional particle-in-cell monte carlo collisions model," *Physics of Plasmas*, vol. 20, no. 11, p. 113511, 2013.

[81] D. Wünderlich, L. Schiesko, P. McNeely, U. Fantz, and P. Franzen, "On the proton flux toward the plasma grid in a RF-driven negative hydrogen ion source for ITER NBI," *Plasma Physics and Controlled Fusion*, vol. 54, no. 12, p. 125002, 2012.

[82] W. Eckstein and J. P. Biersack, "Reflection of low-energy hydrogen from solids," *Applied Physics A*, vol. 38, no. 2, p. 123, 1985.

[83] S. Nishioka, I. Goto, K. Miyamoto, A. Hatayama, and A. Fukano, "Study of ion-ion plasma formation in negative ion sources by a three-dimensional in real space and three-dimensional in velocity space particle in cell model," *Journal of Applied Physics*, vol. 119, no. 2, 2016.

[84] R. J. Procassini, C. K. Birdsall, and E. C. Morse, "A fully kinetic, selfconsistent particle simulation model of the collisionless plasma-sheath region," *Physics of Fluids B: Plasma Physics*, vol. 2, no. 12, p. 3191, 1990.

[85] S. Schlesinger, R. E. Crosbie, R. E. Gagne, G. S. Innis, C. Lalwani, J. Loch, R. J. Sylvester, R. D. Wright, N. Kheir, and D. Bartos, "Terminology for model credibility," *SIMULATION*, vol. 32, no. 3, p. 103, 1979.

[86] R. G. Sargent, "Verification and validation of simulation models," in *Proceedings of the 37th Conference on Winter Simulation*, WSC '05, p. 130, Winter Simulation Conference, 2005.

[87] L. A. Schwager and C. K. Birdsall, "Collector and source sheaths of a finite ion temperature plasma," *Physics of Fluids B: Plasma Physics*, vol. 2, no. 5, p. 1057, 1990.

[88] L. R. G. Treloar and D. H. Landon, "Secondary-electron emission from nickel, cobalt and iron as a function of temperature," *Proceedings of the Physical Society*, vol. 50, no. 5, p. 625, 1938.

[89] J. R. Calvey, G. Dugan, W. Hartung, J. A. Livezey, J. Makita, and M. A. Palmer, "Measurement and modeling of electron cloud in a field free environment using retarding field analyzers," *Phys. Rev. ST Accel. Beams*, vol. 17, p. 061001, 2014.

[90] U. Fantz and D. Wünderlich, "A novel diagnostic technique for H^-(D^-) densities in negative hydrogen ion sources," *New Journal of Physics*, vol. 8, no. 12, p. 301, 2006.

[91] A. Manhard, U. Fantz, A. Stäbler, H. Greuner, and B. Crowley, "Spectroscopic Studies on Positive Ion Based Neutral Beam Injection Systems ," Tech. Rep. IPP 4/289, Max-Planck-Institut für Plasmaphysik, 2008.

[92] S. Nishioka, S. Abe, K. Miyamoto, A. Fukano, and A. Hatayama, "Effect of Coulomb collision between surface produced H^- ions and H^+ ions on H^- extraction mechanism and beam optics in a Cs-seeded H^- ion source by 3D particle in cell model," *Journal of Applied Physics*, vol. 123, no. 6, p. 063302, 2018.

[93] W. Kraus, D. Wünderlich, U. Fantz, B. Heinemann, F. Bonomo, and R. Riedl, "Deuterium results at the negative ion source test facility ELISE," *Review of Scientific Instruments*, vol. 89, no. 5, p. 052102, 2018.

[94] U. Fantz, L. Schiesko, D. Wünderlich, and N. Team, "A comparison of hydrogen and deuterium plasmas in the IPP prototype ion source for fusion," *AIP Conference Proceedings*, vol. 1515, no. 1, p. 187, 2013.

[95] C. Steinbrüchel, "A simple formula for low-energy sputtering yields," *Applied Physics A*, vol. 36, no. 1, p. 37, 1985.

[96] M. Lieberman and A. J. Lichtenberg, *Plasma discharges and Materials processing*. New Jersey: John Wiley & Sons, Inc., 2 ed., 2005.

[97] I. Mario, "Langmuir probe measurements at the ELISE test facility." Private communication, 2018.

[98] T. Kalvas, O. Tarvainen, T. Ropponen, O. Steczkiewicz, J. Ärje, and H. Clark, "IBSimu: A three-dimensional simulation software for charged particle optics," *Review of Scientific Instruments*, vol. 81, no. 2, p. 02B703, 2010.

[99] D. Wünderlich. Private communication, 2016.

Acknowledgements

I acknowledge EUROfusion and the EUROfusion High Performance Computer (Marconi-Fusion) for providing the computational resources needed to produce the results in this thesis.

I would also like to express my gratitude to the people who gave me the chance of carrying on this work and was by my side during my years as a PhD student.

This work was possible thanks to the access to the ONIX source code provided by the Laboratory of Physics of Gases and Plasma (LPGP) at University Paris-Sud. The excellent counseling of Dr. Tiberiu Minea was essential in order to understand the technical and physical aspects of the code. The advices given by Dr. Adrien Revel helped me to understand how to use and modify the ONIX code, the further improvements he implemented to the code helped to reduce the calculation time and obtain results that before could have not been possible.

I would like to thank **Prof. Dr.-Ing. Ursel Fantz**, for her supervision during the entire period of my PhD at the Max-Plank-Institut für Plasmaphysik and betting for me as someone suitable to get the work done.

I would like to thank **Prof. Dr. Liviu Chioncel** for having accepted to be the second reviewer of my PhD thesis.

I want to thank **Dr. Dirk Wünderlich** for all his time, interest and dedication during the project. Also, for solving problems such as obtaining enough computational resources which were essential to obtain all the results of this thesis.

I want to thank **Serhiy Mochalskyy** for acting as guide in all the computational aspects of my project and dedicating more time than he should had.

My gratitude is to **Isabella Mario** for being the best office mate I could ask for. If I were Dante, then she would be Virgil and the PhD I guess it can be deduced.

Thank you very much **Federico D'isa** and **Dr. Alessandro Mimo**, for always worrying for my well-being and always proposing things to enjoy our time outside of work.

During my work a lot of my concerns were solved by people from the group with whom I could also share some time during a coffee break, discuss about almost any subject and get some laughs: **Dr. Federica Bonomo, Dr. Sofia Cristofaro, Dr. Niek Den Harder, Dr. Christian Hopf, Dr. Andrew Hurlbatt, Dr.**

Loïc Schiesko, Giuseppe Starnella, Dr. Christian Wimmer and **Dominikus Zielke** along with all the people of the ITED division.

I must not forget the people that was before, as all my friends of my time living in Argentina. In particular, I would like to mention **Rodrigo Bonazzola**, **Ignacio Fabre** and **Franco Mangussi**, their support and friendship is something I will never forget. Thanks to all my friends wherever in the universe they are as to be rich in friends is to be poor in nothing.

My eternal love and gratitude is always with **my parents** and **my sister**, talking with them by phone was enough to make me feel closer to home. Thanks for being there with me, no matter what was the problem, the time or the place.